IIEEJ Transactions on

Image Electronics and Visual Computing

Special Issue on Extended Papers Presented in IEVC2019

Vol. 8, No. 1 2020

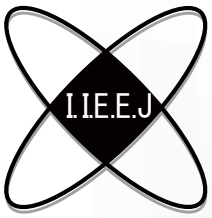

The Institute of Image Electronics Engineers of Japan

Editorial Committee of IIEEJ

Contact Information

The Institute of Image Electronics Engineers of Japan (IIEEJ)
3-35-4-101, Arakawa, Arakawa-ku, Tokyo 116-0002, Japan
Tel : +81-3-5615-2893 Fax : +81-3-5615-2894
E-mail : hensyu@iieej.org
http://www.iieej.org/ (in Japanese)
http://www.iieej.org/en/ (in English)
http://www.facebook.com/IIEEJ (in Japanese)
http://www.facebook.com/IIEEJ.E (in English)

IIEEJ Transactions on
Image Electronics and Visual Computing
Vol.8 No.1 June 2020

CONTENTS

Published two times a year by the Institute of Image Electronics Engineers of Japan（IIEEJ）
3-35-4-101, Arakawa, Arakawa-ku, Tokyo 116-0002, Japan
Tel:+81-5615-2893 Fax:+81-5615-2894 E-mail:hensyu@iieej.org http://www.iieej.org/

Upon the Special Issue on Extended Papers Presented in IEVC2019

Editor: Prof. Naoki KOBAYASHI
Saitama Medical University

The Institute of Image Electronics Engineering of Japan (IIEEJ) regularly holds International academic events named “Image Electronics and Visual Computing (IEVC)” since 2007, on every two or two and half years. The 6th International Conference on Image Electronics and Visual Computing (IEVC2019) was held in Bali, Indonesia on August 21-24, 2019. From this time, the name of this event was changed from International Workshop to International Conference to promote the event more worldwide and more attractive for speakers and attendees. The conference was successfully held with 109 presentations and 165 participants (including 39 foreigners from more than 10 countries).

There were two paper categories in IEVC2019: general paper and late breaking paper (LBP), and in general paper, there were two tracks: Journal track (JT) and Conference track (CT). In IEVC2019, 33 JT papers, 52 CT papers and 24 LBP were submitted.

Journal track is a newly introduced one and has the advantage to be able to publish the paper on the journal (IIEEJ Trans. on IEVC) in the “Special Issue on Journal Track in IEVC2019” on December 2019 issue, by submitting full paper version (8 pages) together with conference paper version to be peer-reviewed in advance. Actually seven papers were adopted in the “Special Issue on Journal Track in IEVC2019” published on December 2019.

The special issue on “Extended Papers Presented in IEVC2019” to be published on June 2020 was openly called for all paper categories in IEVC2019, and five papers have passed the review process to be in time for its publishing schedule. In them, the JT papers not to be in time for the publication of December 2019 Special issue are also included. The papers currently under review will be published in the next issue, if accepted.

Finally, I would like to give great thanks to all the reviewers and editors for their time and efforts towards improving the quality of papers. I would also like to express my deepest appreciation to the editorial committee members of IIEEJ and the staff at IIEEJ office for various kinds of support.

IIEEJ Paper -- Special Issue on Extended Papers Presented in IEVC2019 --

Technique to Embed Information in 3D Printed Objects Using Near Infrared Fluorescent Dye

Hideo KASUGA† (*Member*), Piyarat SILAPASUPHAKORNWONG†, Hideyuki TORII†, Masahiro SUZUKI††, Kazutake UEHIRA† (*Member*)

†Kanagawa Institute of Technology, ††Tokiwa University

<Summary> This paper presents a new technique to embed information in 3D printed objects using a near infrared fluorescent dye. Regions containing a small amount of fluorescent dye are formed inside an object during fabrication to embed information inside it, and these regions form a pattern that expresses certain information. When this object is irradiated with near-infrared rays, they pass through the object made of resin but are partly absorbed by the fluorescent dye in the pattern regions, and it emits near-infrared fluorescence. Therefore, the internal pattern can be captured as a high-contrast image using a near-infrared camera, and the embedded information can be nondestructively read out. This paper presents a technique of forming internal patterns at two different depths to double the amount of embedded information. We can determine the depth of the pattern from the image because the distribution of the brightness of the captured image of the pattern depends on its depth. We can also know from the brightness distribution whether or not a pattern exists at two depths. Because this can express four states, the amount of embedded information can be doubled using this method. We conducted experiments using deep learning to distinguish four states from the captured image. The experiments demonstrated the feasibility of this technique by showing that accurate embedded information can be read out.

Keywords: 3D printer, digital fabrication, information embedding, deep learning

1. Introduction

Digital fabrication has been attracting attention as a new method of manufacturing. This is because a user can obtain a product that he or she wants just by inputting the model data into fabrication equipment. If a user has equipment at home or in the office, he or she can easily obtain a product by obtaining the model data through the Internet and print it. 3D printers are typical digital fabrication equipment that has been reduced in price and miniaturized. As a result, they are beginning to become popular with consumers. Thus, 3D printers are expected to revolutionize distribution and manufacturing in the future[1-3].

3D printers use a unique process called additive manufacturing in which thin layers are formed one by one to form an object[4]. This enables forming any structure inside the object during fabrication. We have studied techniques that form fine patterns inside the object to express information[5-9]. These patterns are made invisible from the outside. Therefore, information can be embedded in the object so that it cannot be seen.

The embedding of information inside 3D printed objects will enable extra value to be added to these objects, expanding their applications. For example, we can embed information that usually comes with newly purchased products (e.g., user manuals) into them. Moreover, it will be possible to use them as "things" of the Internet of Things (IoT) in connecting to the Internet.

In addition to embedding information, we have also studied techniques that can read out embedded information nondestructively from the outside. In that study, we used a fused deposition modeling (FDM) 3D printer with resin as a material. We have studied some techniques to read out embedded information, and one of them uses a near infrared camera. We formed fine patterns inside the fabricated objects using resin that has a high reflectivity or high absorption rate for near infrared light. Those resins were basically the same kind as that of the body of the object. We could capture the inside pattern using a near infrared camera because most resin materials transmit near infrared rays.

We have also studied a technique for forming patterns containing a small amount of fluorescent dye. Fluorescent dye emits near-infrared fluorescence; therefore, the internal pattern can be captured as a high-contrast image using a near-infrared camera. This enhances the readability of the embedded information.

This paper describes a technique that can double the amount of information embedded. It embeds patterns containing fluorescent dye at two different depths to achieve double the amount of embedded information. In order to read out information, we needed a technique to recognize whether or not a pattern exists at each depth. We used deep learning for this recognition. This paper also describes the results of experiments conducted to validate the feasibility of this method.

2. Information Embedding Inside 3D Printed Objects

2.1 Information embedding by forming fine patterns inside 3D printed objects

Figure 1 illustrates a simple example of embedding information inside an object by forming fine patterns. A 3D-printed object contains fine domains having physical characteristics such as optical, acoustic, or heat conduction differing from the other part of the object. Although various ways can be used to express information due to the disposition of the fine domain, one example involves binary data, "1" or "0," being expressed due to a fine domain existing or not existing in a designated position, as shown in Fig. 1.

We can expect to read out these embedded binary data by detecting the presence or absence of a domain at a designated position utilizing the difference in physical characteristics between the materials of the fine domain and another part of the object.

In our previous study, inside patterns were sensed nondestructively from outside the object using a near infrared camera and thermography to determine the difference in the thermal conductivity and optical characteristics in a near infrared region.

2.2 Related work on Information embedding inside 3D printed objects

Related work includes a technique of embedding information inside 3D printed objects using a thin plate with a cutout pattern. Willis and Wilson first created product parts, one of which had a visible pattern, and then assembled these parts into one product so that the patterned part was inside it[10]. They read out the patterned information inside using terahertz wavelength light. However, in practical terms, applying it to common 3D printing was too complicated.

Another related study involved embedding an RFID tag in 3D printed objects[11]. Object fabrication is suspended once in embedding an RFID tag, and it is put on the fabricated surface; then, fabrication is resumed to cover the RFID tag. After fabrication is completed, the RFID tag is embedded inside the objects.

In these related studies, users could not make an object by just inputting data. They needed additional parts and additional processes; therefore, the features of 3D printing were completely lost. In contrast, the patterns in our technique are integrally formed using the body-utilizing additive manufacturing process of 3D printers, which eliminates any additional processes. This means whoever obtains data can make the objects in which information is embedded inside.

2.3 Information embedding using fluorescent dye

Figure 2 shows the basic principle of the technique using fluorescent dye. It assumes that the resin is used as an object material. The dotted rectangles in Fig. 2 indicate the inside pattern region. The pattern regions are formed using the same resin as that of the other regions, but they contain a small amount of fluorescent dye. The rays reach the internal fluorescent dye when the object is irradiated with near-infrared rays from the outside because resin has high transmittance for near infrared. The light source irradiates

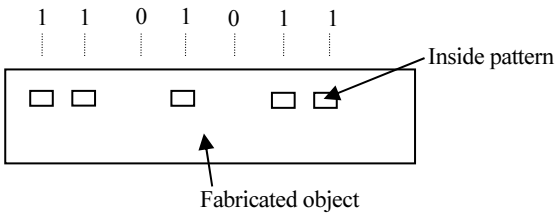

Fig. 1 Example of embedding information inside object

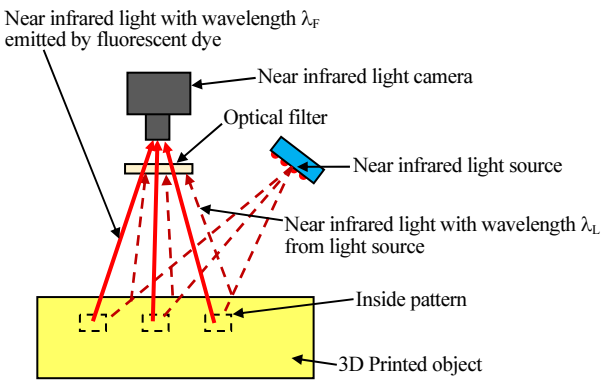

Fig. 2 Basic concept of technique

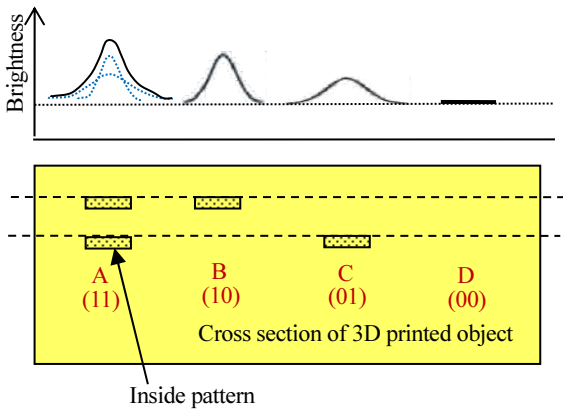

Fig. 3 Basic configuration of dual depth

light with wavelength λ_L in the near infrared region, which excites the fluorescent dye. The dye is excited and emits florescence with wavelength λ_F, which is also near the infrared region but differs from λ_L. Because the dye emits the light, a bright image of the patterns inside the resin object can be captured.

Because wavelength λ_F of the dye's fluorescence differs from wavelength λ_L of the irradiated light, only light the fluorescent dye emits enters the camera. An optical filter that blocks the source light reflected from the object surface is used; therefore, a low noise image of the inside patterns can be obtained.

2.4 Dual depth embedding

Figure 3 shows the basic configuration of dual depth embedding. The inside patterns are formed at two different depths. We can express 2-bit information at one position using this arrangement. For example, we can assign (11) when patterns exist at both depths (A in Fig. 3), (10) when a pattern exists at only low depth (B in Fig. 3), (01) when it is at only high depth (C in Fig. 3), and (00) when no pattern exists (D in Fig. 3). In the previous method, only one bit could be embedded at one position, but this method enables embedding two bits. Therefore, the amount of information that can be embedded is double.

Near-infrared rays transmit through the resin but are scattered to some extent during transmission. This scattering increases as the passing distance increases. Therefore, when the near infrared image of the internal pattern is captured from the outside, the image of the pattern blurs. In addition, the blurring becomes more pronounced for images of deep patterns. Therefore, the brightness distribution of the captured image changes depending on the depth, as shown

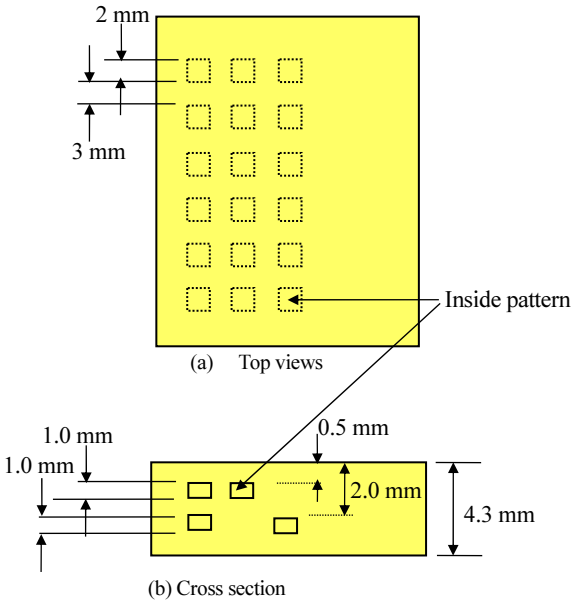

Fig. 4 Layout of sample

in Fig. 3. The difference in the brightness distribution at positions B and C in Fig. 3 shows this state clearly. When patterns are at two depths, the brightness distribution is the sum of them, as shown in Fig. 3, for position A. Therefore, we should be able to recognize which of the four cases the captured image is; that is, 2-bit binary information can be read out.

In our previous study[12], we could see clear differences in brightness distribution at four positions, as shown in Fig. 3, for the naked eye–except between images at Position A and Position B.

Recognizing these four states using pattern recognition techniques is possible because few differences are evident in the histogram of the captured image for (11) and (10) and because few differences are evident in the brightness distribution. In this study, we used deep learning to recognize the four states and read out the 2-bit binary information from each position.

3. Experiments

3.1 Sample preparation

Figure 4 shows the designed layout of the sample. Four types of arrangements of patterns at two depths were formed in equal numbers for each row. The pattern size was 1×1 mm, and the thickness was 1 mm. The reason for adopting 1×1 mm as the minimum size was that this pattern was the smallest that could be formed stably.

The depth of the upper pattern from the surface was 0.5

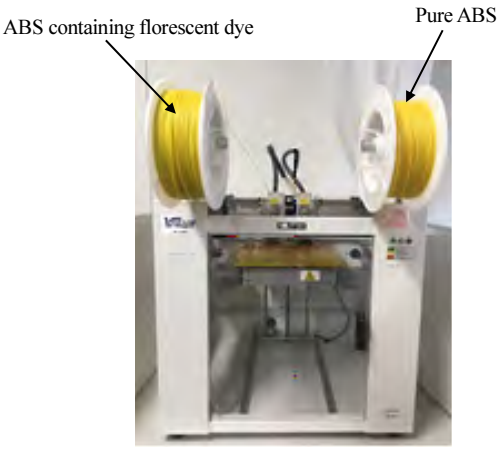

Fig. 5 3D printer used in experiment

mm, and that of the bottom pattern was 2 mm. The reason for setting the depth to 0.5 mm was that the pattern could not be seen from the outside at that depth. As the bottom pattern becomes deeper, the blurring of the pattern increases, and it becomes easier to distinguish from the shallow pattern. However, if it becomes too deep, the brightness decreases significantly, and the pattern cannot be recognized. Therefore, we chose 2 mm as the optimum depth for the bottom pattern.

We used a FDM 3D printer, Mutoh Value3D MagiX 2200D, shown in **Fig. 5**, to fabricate the samples. It has two nozzles so that two kinds of materials can be used for one object. The lamination pitch (resolution in the z-direction) of this 3D printer was 0.05 mm.

The body structure was fabricated using pure acrylonitrile butadiene styrene (ABS) resin, which is the one on the right in Fig. 5, and the inside patterns were formed using the same ABS resin as that for the body; however, it contained a small amount of florescent dye (less than 1%), which can be seen on the left. The color of the ABS containing florescent dye is almost the same as that of pure ABS. Therefore, even if the pattern is formed very shallow from the surface, it cannot be seen.

The melting temperature of the ABS containing fluorescent dye was the same as that of pure ABS; therefore, the sample was fabricated in a successive process using the same temperature for the nozzle and stage. **Figure 6** shows an example of the samples.

3.2 Capture of near infrared images

Figure 7 shows the layout and photograph of the near infrared image capture system used to take a near infrared Image. We used two sets of LED arrays as near infrared

Fig. 6 An example of samples.

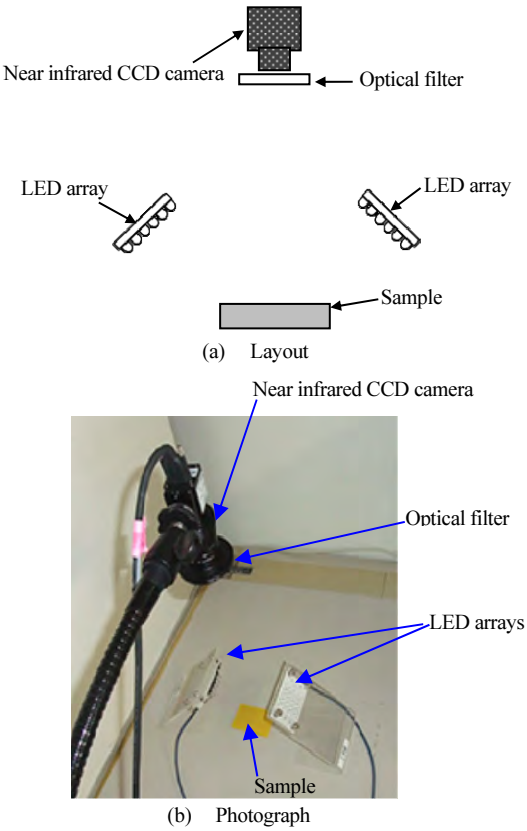

Fig. 7 Near infrared image capture

light sources. They were placed 10 cm away from the sample. Their wavelength was 760 nm, and the power was 12 W in a total of 2 sets. A 2048 × 1088 pixel CCD camera, a conventional silicon-based one, was used. Because we removed the cold filter placed in front of the CCD sensor, it was sensitive to light with wavelengths up to 1100 nm. It was set at the same side as the aforementioned sample between the LED arrays.

An optical filter was placed in front of the camera lens. We used a long-pass optical filter with a cutoff wavelength of 850 nm.

3.3 Reading out embedded information using deep learning

Four kinds of neural network, ResNet50[13], Network in

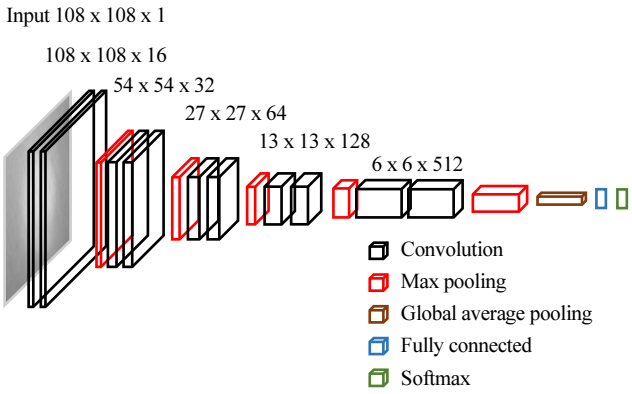

Fig. 8 Configuration of original neural network model

Table 1 Layers of original model

Input image 108 x 108 x 1
Convolution 108 x 108 x 16
Convolution 108 x 108 x 16
Max pooling
Convolution 54 x 54 x 32
Convolution 54 x 54 x 32
Max pooling
Convolution 27 x 27 x 64
Convolution 27 x 27 x 64
Max pooling
Convolution 13 x 13 x 128
Convolution 13 x 13 x 128
Max pooling
Convolution 6 x 6 x 512
Convolution 6 x 6 x 512
Max pooling
Global average pooling
Fully connected 4
Softmax

Network (NIN) [14], GoogLeNet[15], and an original model were used to distinguish four states of captured images for reading out embedded information. ResNet50, NIN, and GoogLeNet are neural networks commonly used in the field of image classification. In our study, these neural networks consisted of the same network used in ImageNet large scale visual recognition challenge (ILSVRC).

The original model is a simple but highly accurate neural network. It is based on VGG[16], and the number of layers and the number of channels were adjusted. The configuration is shown in **Fig. 8**. The layers are shown in **Table 1**. The input to our original network is a 108× 08 grayscale image. Therefore, the size of the first convolution layer is 108×108 × 16. We used a 3× convolution filter. The convolution stride is 1. ReLU was used for the activation function. The number of channels in the first layer is 16 because the accuracy did not improve and because the calculation cost increased even if the number of channels was very high. Max pooling was performed with a kernel size of 2× 2 and a stride of 2. As a result, the spatial resolution was down-sampled in half. The number of channels was doubled after each max pooling layer. However, the last two convolution layers had 512 channels. This is because increasing the number of channels in the last two layers improved accuracy. The global average pooling layer, the fully connected layer, and the soft-max layer come after the convolution layers.

Fig. 9 Example image of the sample captured with near infrared CCD camera

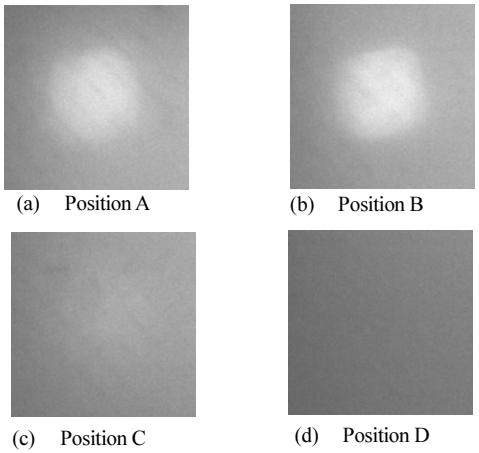

Fig. 10 Example images cut out at position shown in Fig. 3

Images at each position with 108×108 pixels were cut out. These images were input to neural networks. Because the sample had only six positions for each binary number, as shown in Fig. 3, 25 photos of the sample were taken under various conditions. Therefore, 150 photos were obtained for each binary number, that is, 600 photos were used in the evaluation. 500 photos were used for training, and 100 photos were used for the evaluation. We evaluated the accuracy in reading out embedded information using the aforementioned deep learning.

4. Results and Discussion

Figure 9 shows one example of images of the sample

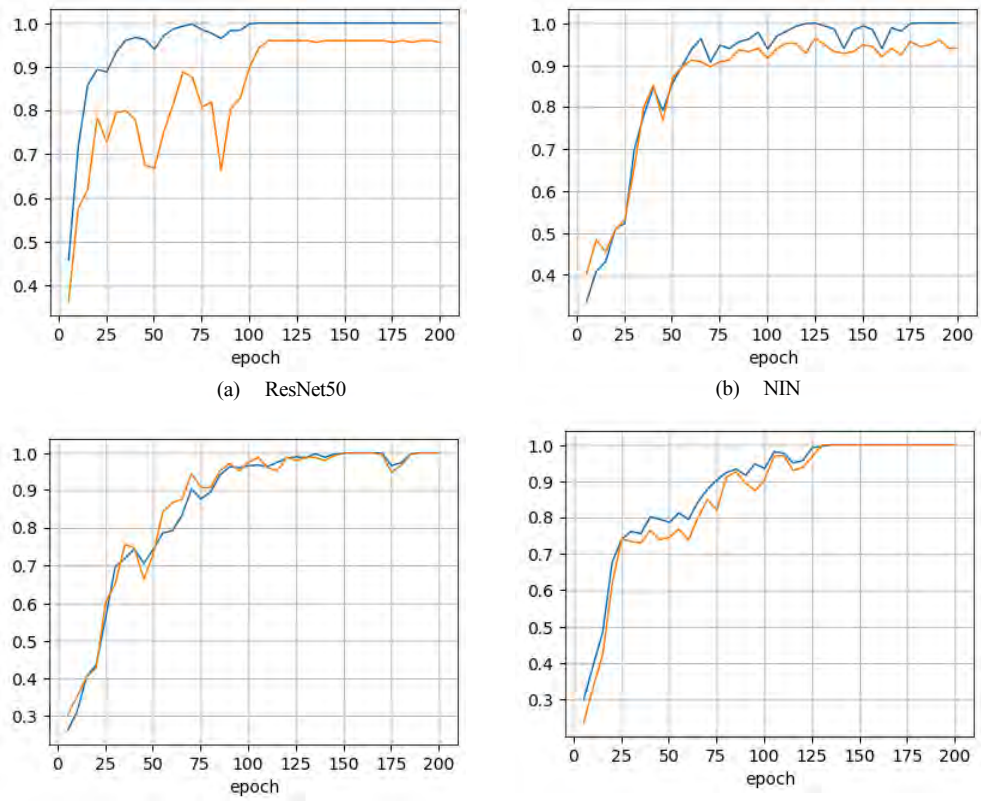

(a) ResNet50 (b) NIN

(c) GoogLeNet (d) Original model

Fig. 11 Training accuracy and validation accuracy — Training accuracy, Validation accuracy

captured with the CCD camera, and Fig. 10 shows the example images cut out at a position shown in Fig. 3 as A to D. **Figure 10** (b) and (c) show that the blur of the image differs depending on the depth of the pattern, as expected. Therefore, the three cases having only one pattern or no pattern at two depths can be distinguished from each other using the distribution. However, no clear difference in the image and the luminance distribution is evident when only one pattern is at a shallow position and when two patterns are at both depths. This is because the light intensity from the pattern at the shallow position is much higher than that at the deep position. If the depth of the latter pattern decreases or if the thickness of the pattern is increased, the difference between the two can be seen.

In order to distinguish four cases, we performed neural network training using 500 images captured with the CCD camera. We randomly selected 10% of the training data for use as validation data. **Figure 11** shows the training accuracy and validation accuracy of four kinds of neural networks. The training curve indicates that training was almost completed at 200 epochs in any neural network. The training accuracy after sufficient training was nearly 100% for all models. However, the validation accuracy of NIN and ResNet50 was lower than the training accuracy. In particular, the training curve of ResNet50 was mostly very high, but the validation curve was lower in the whole range. These results indicate that overfitting occurred. Because overfitting naturally occurs when the model is too complex, ResNet50 was too complex for our study. The original model, which has a simple structure, had almost no difference between the training curve and the validation curve. Therefore, overfitting hardly occurred with it. Because GoogLeNet also had almost no difference between the training curve and the validation curve, overfitting hardly occurred with it, as well. According to these training and validation curves, GoogLeNet and Original model showed high accuracy.

To evaluate the discrimination accuracy using the trained model, we conducted a test using 100 images captured with the CCD camera. These images, which were test data sets, were randomly selected from 600 images captured for the experiment. We repeated training and testing 12 times to find the average of the discrimination accuracy. **Table 2** shows the average accuracies of the test data set evaluated using the trained models. The accuracy was over 90% with any neural network. Although the

difference in accuracy was small, GoogLeNet was the most accurate. However, the original model was just as accurate. Because our model had fewer parameters than GoogLeNet, it could be calculated faster and required less machine power. Because the difference in accuracy between GoogLeNet and Original model was small, the original model was sufficiently effective. The accuracy of ResNet50 was lower than that of the original model. ResNet50 had the most parameters among the four neural networks and took time to process. NIN is a neural network that was calculated faster than GoogLeNet or ResNet50, but it had the lowest accuracy among the four kinds of neural network.

The accuracy rates of these four kinds of neural networks were all as high as about 95%, though a slight difference was evident between them. These high accuracies indicate the possibility of achieving 100% with some improvement in the future.

We did not reach 100% accuracy in this study for two reasons. The first was that the difference between the images of the pattern at positions A and B was too small. This is because the brightness of the images of deep patterns was small; therefore, increasing the brightness using the aforementioned methods will improve the accuracy. The second reason is that only 500 images were used for learning, and this was not enough for image recognition by deep learning. The accuracy will be further improved if the number of images for learning is increased.

5. Conclusion

We studied a technique to embed information in 3D printed objects by forming patterns at two depths inside the object using a near infrared fluorescent dye. The fluorescent dye was used because it can capture bright, high-contrast pattern images. This technique can double the amount of embedded information by expressing 2-bit information depending on whether or not patterns exist at two depths. In the experiments, whether or not a pattern existed at each of the two depths was identified using four kinds of neural networks from the images taken using a near infrared camera. Experiment results showed that the accuracy rates of these four neural networks were all as high as about 95%. These high accuracies indicate the possibility of achieving 100% with some improvement in the future and indicate the feasibility of this technique.

In future work, we will optimize the depth and thickness of the deep patterns to distinguish the four states clearly, in addition to increasing the number of images used for learning. This should enable achieving 100% accurate recognition.

Table 2 Average of discrimination accuracy of each model

Network model	Average accuracy
ResNet50	94.25%
NIN	93.67%
GoogLeNet	95.50%
Original model	95.42%

Acknowledgement

We would like to thank DIC Corporation for providing the fluorescent dye used in this study. This research was supported by a grant aid program from the Kanagawa Institute of Technology in 2018.

References

1) B. Berman: “3-D Printing: The New Industrial Revolution”, Business Horizons, Vol. 55, No. 2, pp. 155–162 (2012).

2) B. Garrett: “3D Printing: New Economic Paradigms and Strategic Shifts”, Global Policy, Vol. 5, No. 1, pp. 70–75 (2014).

3) C. Weller, R. Kleer, F. T. Piller: “Economic Implications of 3D Printing: Market Structure Models in Light of Additive Manufacturing Revisited”, Proc. of International Journal of Production Economics, Vol. 164, pp. 43–56 (2015).

4) S. Yang, Y. F. Zhao: “Additive Manufacturing-Enabled Design Theory and Methodology: A Critical Review”, International Journal of Advanced Manufacturing Technology, Vol. 80, No. 1-4, pp. 327–342 (2015).

5) M. Suzuki, P. Silapasuphakornwong, K. Uehira, H. Unno, Y. Takashima: “Copyright Protection for 3D Printing by Embedding Information inside Real Fabricated Objects”, International Conference on Computer Vision Theory and Applications, pp. 180–185 (2015).

6) M. Suzuki, P. Dechrueng, S. Techavichian, P. Silapasuphakornwong, H. Torii, K. Uehira: “Embedding Information into Objects Fabricated With 3-D Printers by Forming Fine Cavities inside Them”, Proc. of IS&T International symposium on Electronic Imaging, Vol. 2017, No. 41, pp. 6–9 (2017) .

7) P. Silapasuphakornwong, M. Suzuki, H. Unno, H. Torii, K. Uehira, Y. Takashima: “Nondestructive Readout of Copyright Information Embedded in Objects Fabricated with 3-D Printers”, Proc. of The 14th International Workshop on Digital-forensics and Watermarking, Revised Selected Papers, pp.232–238 (2016).

8) K. Uehira, P. Silapasuphakornwong, M. Suzuki, H. Unno, H. Torii, Y. Takashima: “Copyright Protection for 3D Printing by Embedding Information Inside 3D-Printed Object”, Proc. of The 15th International Workshop on Digital-forensics and Watermarking Revised Selected Papers, pp.370–378 (2017).

9) P. Silapasuphakornwong, M. Suzuki, H. Torii, K. Uehira, Y. Takashima: “New Technique of Embedding Information inside 3-D Printed Objects”, Journal of Imaging Science and Technology, Vol. 63, No. 1, pp. 010501-1- 010501-8 (2019).

10) K. D. D. Willis, A. D. Wilson: “InfraStructs: Fabricating Information inside Physical Objects for Imaging in the Terahertz Region”, ACM Trans. on Graphics, Vol. 32, No. 4, pp. 138-1–138-10 (2013.).

11) K. Fujiyoshi: “Personal Fabrication That Links Information with Things Using RFID Tags”, Keio University Graduation Thesis (2015) in Japanese.

12) P. Silapasuphakornwong, H. Trii, K. Uehira, A. Funsian, K. Asawapithulsert, T. Sermpong: “Embedding Information in 3D Printed Objects Using Double Layered Near Infrared Fluorescent Dye”, Proc. of 3rd International Conference on Imaging, Signal Processing and Communication (2019).

13) K. He, X. Zhang, S. Ren, J. Sun: “Deep Residual Learning for Image Recognition”, Proc. of The IEEE Conference on Computer Vision and Pattern Recognition (CVPR), pp. 770–778, (2016).

14) M. Lin, Q. Chen, S. Yan: “Network in Network”, arXiv: 1312.4400 (2013).

15) C. Szegedy, W. Liu, Y. Jia, P. Sermanet, S. Reed, D. Anguelov, D. Erhan, V. Vanhoucke, A. Rabinovich: “Going Deeper with Convolutions”, Proc. of The IEEE Conference on Computer Vision and Pattern Recognition, pp. 1–9 (2015).

16) K. Simonyan, A. Zisserman, “Very Deep Convolutional Networks for Large-Scale Image Recognition”, CoRR, abs/ 1409.1556 (2014).

(Received September 26, 2019)

Hideo KASUGA (*Member*)

He received his B. E. and M. E. degree in computer science, and his Ph. D. degree in engineering from Shinshu University in 1995, 1997 and 2000, respectively. He is currently an associate professor at the Department of Information Media, Kanagawa Institute of Technology. His research interests include image processing, image recognition and machine learning.

Piyarat SILAPASUPHAKORNWONG

She received her BS (2007) and Ph.D. (2013) in Imaging Science from Chulalongkorn University, Bangkok, Thailand. Since 2014, she has been a researcher at the Human Media Research Center, Kanagawa Institute of Technology, Atsugi, Kanagawa, Japan. Her research interests include image processing, computer vision, multimedia, human-computer interaction, geoscience, and 3D-printing. She is currently a member of IEEE and IEEE Young Professionals.

Hideyuki TORII

He received his B.Eng., M. Eng., and Ph.D. degrees from the University of Tsukuba, Tsukuba, Japan, in 1995, 1997, and 2000, respectively. He joined the Department of Network Engineering, Kanagawa Institute of Technology as a research associate in 2000 and is currently a professor in the Department of Information Network and Communication of the same University. His research interests include information hiding, spreading sequences, and CDMA systems.

Masahiro SUZUKI

He received his Ph.D. degree in psychology from Chukyo University in Nagoya, Aichi, Japan in 2002. He then joined the Human Media Research Center of Kanagawa Institute of Technology in Atsugi, Japan in 2006 as a postdoctoral researcher. He joined the Department of Psychology of Tokiwa University in Mito, Ibaraki, Japan in April 2017 as an assistant professor. Dr. Suzuki is currently engaged in research on digital fabrication and mixed reality.

Kazutake UEHIRA (*Member*)

He received his B.S., M.S., and Ph. D in Electronics in 1979, 1981, and 1994 respectively from the University of Osaka Prefecture, Japan. In 1981, he joined NTT Electrical Communication Laboratories in Tokyo, where he was engaged in research on imaging technologies. In 2001, he joined Kanagawa Institute of Technology, Atsugi, Japan, as a professor and is currently engaged in research on information embedding technology for digital fabrication.

IIEEJ **Paper** *-- Special Issue on Extended Papers Presented in IEVC2019 --*

Feasibility Study of Deep Learning Based Japanese Cursive Character Recognition

Kazuya UEKI† (*Member*) , Tomoka KOJIMA†

† School of Information Science, Meisei University

<**Summary**> In this study, to promote the translation and digitization of historical documents, we attempted to recognize Japanese classical 'kuzushiji' characters by using the dataset released by the Center for Open Data in the Humanities (CODH). 'Kuzushiji' were anomalously deformed and written in cursive style. As such, even experts would have difficulty recognizing these characters. Using deep learning, which has undergone remarkable development in the field of image classification, we analyzed how successfully deep learning could classify more than 1,000-class 'kuzushiji' characters through experiments. As a result of the analysis, we identified the causes of poor performance for specific characters: (1) 'Hiragana' and 'katakana' have a root 'kanji' called 'jibo' and that leads to various shapes for one character, and (2) shapes for hand-written characters also differ depending on the writer or the work. Based on this, we found that it is necessary to incorporate specialized knowledge in 'kuzushiji' in addition to the improvement of recognition technologies such as deep learning.

Keywords: character recognition, deep learning, data augmentation, Japanese cursive character ('kuzushiji')

1. Introduction

Currently, the Japanese language uses three types of scripts for writing: 'hiragana', 'katakana', and 'kanji'. These characters have changed in different periods, and it is currently difficult for non-experts to read classical Japanese literature. By deciphering historical literature, we are able to know what was accomplished in that era. Therefore, a large amount of research on the reprinting of historical literature has been conducted. However, a large number of literary works have not yet been digitized. One of the considerable barriers to this digitization is that Japanese classical literature was written in a cursive style using 'kuzushiji' characters that are very difficult to read for contemporary people. Characteristics of 'kuzushiji' characters written in classical documents are summarized in three points: first many of them were written with a brush, second many characters are connected, and third the same character may experience many variations in shape. In response to these problems, several attempts were made using deep learning methods to digitize literary works and improve the convenience of reprinting. The recognition rate for handwritten characters is becoming relatively high with the development of deep learning technology, however 'kuzushiji' character classification is still insufficiently developed. The root of the problem is that 'kuzushiji' characters used in classical documents are not standardized in the same way as modern characters; they can appear quite different even based on the same underlying character, and, in addition, other characters may appear similar.

In this study, we trained deep learning models using more than 1,000-class character images and checked how well our trained models performed. Furthermore, we analyzed classification results to identify causes of poor performance, and considered how to tackle these problems. The contribution of this work is the following three-fold.

1. In previous research on 'kuzushiji' characters, experiments were conducted mainly with approximately 50 different 'hiragana', whereas in this study, we clarified what kind of problems existed when we recognized more than 1,000 different 'kuzushiji' characters including 'katakana' and 'kanji'.
2. In addition to adapting machine learning techniques to improve the classification rate, we found some problems specific to 'kuzushiji' characters and discussed several plans of improvement.
3. We established a method to automatically judge which characters should not be judged by the system and passed on to the expert to make the final decision. This function will make it easy for transcribers in the post-process to judge from the context, that

is, the previous and subsequent characters.

An overview of the remainder of paper is as follows: in section 2, we describe previous work, and in section 3, we explain the Japanese cursive character image dataset. In section 4, we present experimental results for deep learning models, and in section 5, we discuss conclusions and future work.

Here, to avoid confusion, we explain the Japanese terms used throughout this paper.

- 'Hiragana': One of the three different character sets used in the Japanese language. Each 'hiragana' character represents a particular syllable. There are 46 basic characters.
- 'Katakana': In the same way as 'hiragana', 'katakana' is one of the three different character sets used in the Japanese language. 'Katakana' is also a phonetic syllabary: each letter represents the sound of a syllable. There are 46 basic characters as well.
- 'Kanji': 'Kanji' is another one of the three character sets used in the Japanese language. Along with the syllabaries, 'kanji' is an ideographic character: each letter symbolizes its meaning. Most of them were imported from China, but some 'kanji' characters were developed in Japan. It is said that approximately 50,000 'kanji' characters exist. However, approximately 2,500 are actually used in daily life in Japan.
- 'Kuzushiji': Anomalously deformed characters. They were written in cursive style and they are mainly seen in works from the Edo period. The Edo period is the period between 1603 and 1868 in the history of Japan.
- 'Jibo': Root 'kanji' characters of 'hiragana' and 'katakana'. For example, the character "あ" was derived from a different 'jibo' such as "安" and "阿".

2. Related Work

In conventional research on handwritten character classification, a relatively high accuracy rate can be achieved using high-quality images. This trend was based on a CNN called LeNet with a convolution and pooling structure proposed by LeCun et al.[1),2)], which succeeded in recognizing handwritten digits. CNNs were also widely used for recognizing 'kuzushiji' characters (especially 'hiragana') written in the classical literature, and achieved relatively high accuracy[3),4)]. However, because of noise and defects inherent in character images in ancient documents, the classification accuracy may be adversely impacted. Hayasaka et al. reported that a 75% classification rate was achieved for 48 types of 'hiragana' such as "あ", "い", ... , "ゑ", "を", and "ん"[3)]. Ueda et al. also used deep learning to recognize 'hiragana' character[4)]. They used the fact that the aspect ratio differs between characters and combined it with the result of a deep learning based approach. Their classification accuracy was approximately 90% for 46 'hiragana' characters.

In addition, there is another research on tasks that are close to actual transcription, such as working on the recognition of consecutive characters[5)]. They proposed a method for recognizing images of continuous characters in the vertical or horizontal directions. Recognition of three characters in the vertical direction was achieved by a structure that consists of three components of a CNN, a bi-directional long short-term memory (BLSTM)[6)] and a connectionist temporal classifier[7)]. Recognition of three or more characters in the vertical and horizontal directions was achieve by a two-dimensional BLSTM and a faster region-CNN that for object detection.

Most research on 'kuzushiji' recognition have focused on the classification of 'hiragana' as mentioned above. However, classical documents are not limited to 'hiragana', as they also include 'katakana' and 'kanji'. To read classic documents electronically, it is necessary to identify a wide range of characters and improve the accuracy rate on them. Based on this, we focused on recognizing a wide range of characters including 'hiragana', 'katakana', and 'kanji' using the publicly available 'kuzushiji' dataset[8)].

On a separate topic, Yamamoto et al. proposed a new type of OCR technology to save on labor in high-load reprint work[9)]. It was deemed important to divide reprinting work among experts, non-experts and an automated process rather than completely automating processing. The objective was not to achieve a decoding accuracy of 100% with OCR automatic processing alone; instead ambiguous letters were left as "〓 ('geta')" and passed on to the expert in charge of post-processing to make a decision. As a result, it was possible to achieve quick and high-precision reprinting. Therefore, we will try to confirm whether we can automatically detect difficult characters using machine learning technique.

3. Japanese Cursive Character Image Dataset

In this work, we used the Japanese cursive 'kuzushiji' character image dataset[8)] released by the Center for Open Data in the Humanities (CODH). This 'kuzushiji' database includes cropped images of three different sets of characters, namely 'hiragana', 'katakana', and 'kanji'. These images were cropped from fifteen literary works from the Edo period, such as "The Year of My Life" and

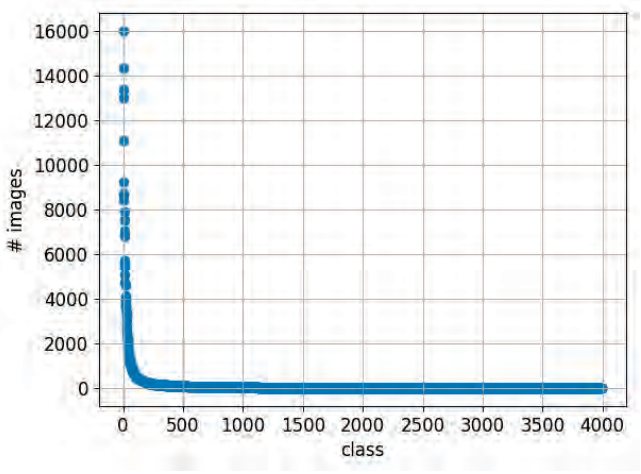

Fig. 1 The number of images in each class in the 'kuzushiji' dataset[8)]

"Ugetsu Monogatari," famous stories from the Edo period, and cooking books that inform us of the food culture in the Edo period. As of November 2018, 403,242 images with 3,999 character classes are publicly available. Additionally, deep learning based sample programs in Python are also provided, helping us readily conduct 'kuzushiji' character classification experiments. The number of images in each character class is reported in **Fig. 1**. The number of images in each class is heavily unbalanced. For example, the class with the largest number of images is "に" (Unicode: U+306B), which has 15,982 images. By contrast, many classes only have a few images, and 833 classes only have one image. For this reason, in this work, we only used character classes with more than 20 images. As a result, the total number of images used in our experiments is 389,267, and the number of classes is 1,195.

As we checked images in the dataset, there were many characters that were difficult to distinguish clearly from others due to the versatility in their shape as indicated in **Fig. 2**. Character "り" (Unicode: U+308A) shown on the left of Fig. 2 was originally derived from 'jibo' "利". Character "わ" (Unicode: U+308F) shown on the right of Fig. 2 was originally derived from 'jibo' "和". There were also identical characters whose appearances differ greatly as shown in **Fig. 3**. These example images show various shapes for the one character "あ" (Unicode: U+3042). Here, 'Jibo' on the left is "安", and 'jibo' on the right is "阿". This is because 'hiragana' and 'katakana' characters originally derived from 'kanji' characters called 'jibo' (maternal glyph), and some 'hiragana' and 'katakana' characters derived from different 'jibo'. Moreover, identical characters may have the same 'jibo' but be represented differently depending on the work or the writer as shown in **Fig. 4**. Figure 4 shows example images of the character "な" (Unicode: U+306A), which was originally derived from the same 'jibo' "奈".

Fig. 2 Examples of similar shapes despite characters being different

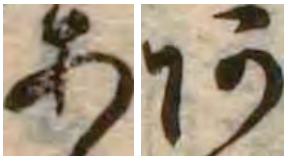

Fig. 3 Examples of separate deformation caused by different 'jibo'

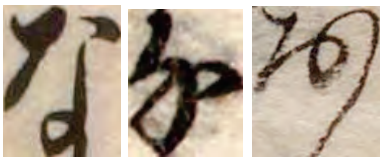

Fig. 4 Examples of differences in deformation despite being linked to the same 'jibo' depending on the work or the writer

4. Character Recognition Experiments

In this section, we will evaluate how deep learning approaches can effectively deal with the problem of 'kuzushiji' character classification.

4.1 Investigation of baseline classification accuracy

To validate the baseline accuracy of 'kuzushiji' recognition, we conducted experiments using 389,267 character images with 1,195 classes from the 'kuzushiji' dataset presented in section 3. The data was divided into training data (194,633 images) and test data (194,634 images) so that the number of datapoints in all literary works was as uniform as possible. The number of training images for each class is shown in **Fig. 5**. It is quite visible that the number of datapoints available for training is extremely small in most classes.

In our experiments, Python based deep learning tools implemented by CODH were used. All images were converted to grayscale and resized to 28×28 to serve as input for a convolutional neural network (CNN). The network model structure used was the same as the one that aimed to classify MNIST handwritten digit images; it consists of two convolution layers including pooling layers and one fully-connected layer with a softmax function to output probabilities for each character class. With regard to the other layers, a rectified linear unit (ReLU) activa-

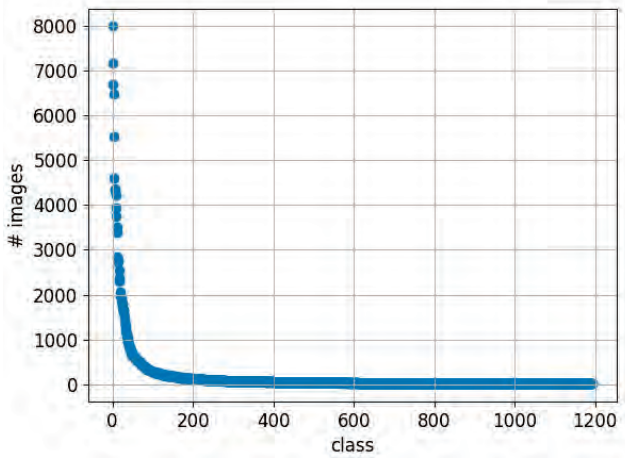

Fig. 5 Number of training images in each character class

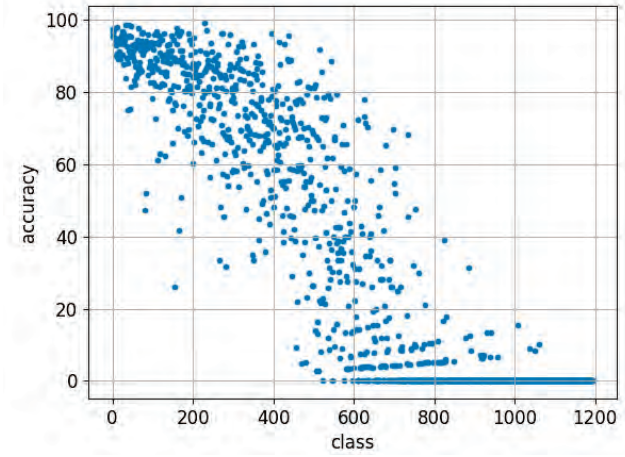

Fig. 6 Classification rate for each character class (baseline)

tion function was used. Models were trained with the AdaDelta algorithm.

We conducted training for 120 epochs on the entire training data and chose a model for which our test loss was at its minimum (50 epochs in our experiments). At this point, although the classification accuracy achieved was 84.75%, the average accuracy of each class was 37.93%. The classification rate for each class is reported in **Fig. 6**. It is apparent that the data linked to many classes with a small number of training samples was not classified correctly.

4.2 Improvements on the classification rate with data augmentation

For classes with a limited number of training samples, the classification accuracy deteriorates. Data augmentation is a widely used technique in many tasks such as image classification, and can help us tackle this problem. Specifically, for classes with less than one hundred images, pictures were augmented using the following transformations so that the number of datapoints in each class became more than a hundred.

Fig. 7 Example of data augmentation

- Rotation ($\leq$ 3 degrees)
- Width shift ($\leq 0.03 \times image\_width$)
- Height shift ($\leq 0.03 \times image\_height$)
- Shear transformation ($\leq \pi/4$)
- Zoom ($[1-0.03 \times image\_size, 1+0.03 \times image\_size]$)
- RGB channel shift (≤ 50)

In our program implementation, first, RGB values were changed, then color images were changed to gray-scale images to input to CNN. When the RGB values were changed into gray-scale, the intensity values were changed as well. After all, RGB channel sift was equivalent to changing the brightness value. Examples of augmented images are shown in **Fig. 7**. The original images are located on the upper left. The other nine images are created by data augmentation. Using 261,407 images including augmented ones, we trained the model one more time for 120 epochs, and retained the best configuration (95 epochs in our experiment). By evaluating test data using this model, the classification rate improved from 84.75% to 88.98%, and the average classification rate over all classes greatly improved, rising from 37.93% to 78.02%. The classification rate for each class is indicated in **Fig. 8**. Significant improvements were seen in classes with a limited number of training samples.

4.3 Experimental results and discussion

Analyzing instances where performance remained poor for specific characters even after data augmentation, we identified certain root causes. An example character is displayed in **Fig. 9**. The classification rate of the character "衛" (Unicode: U+885B) was very low, at 13.6% (=3/22). These characters were deformed differently based on the literary work or the writer. In another example, we found that images of a daily used 'kanji' "衛" were mostly mis-classified as an old character form "衞" as shown in **Fig. 10**. These characters were assigned

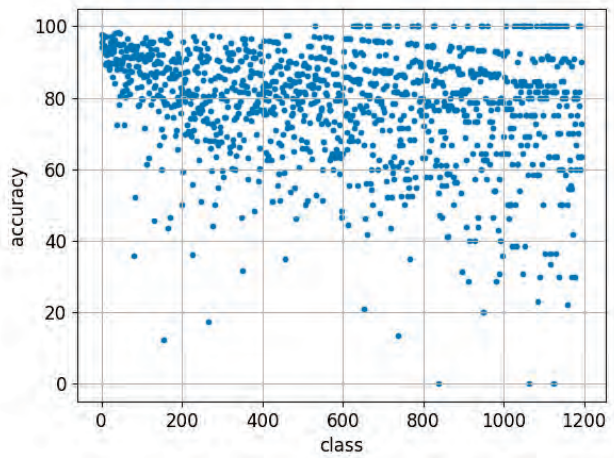

Fig. 8 Classification rate for each character class after data augmentation

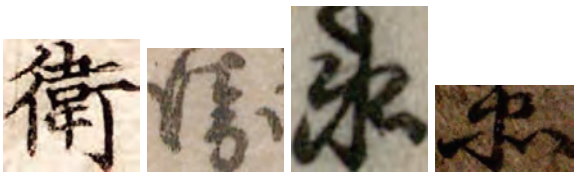

Fig. 9 The identical character "衛" (Unicode: U+885B) in the different literary works

Fig. 10 The character "衛" (Unicode: U+885E) is the old form of character of "衛"

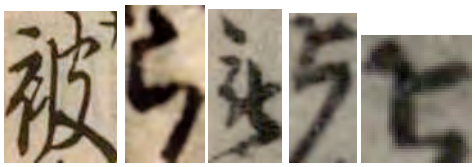

Fig. 11 The example of the character "被" (Unicode: U+88AB)

different codes in the database, but as they were usually treated as the same 'kanji', it was difficult to recognize them. Another example character is shown in **Fig. 11**. The classification rate for the character "被" (Unicode: U+88AB) was 0% (=0/13). We believe the poor performance comes from the versatility of characters, as well as the occurrence of blurred or partially missing images. As the writings included a series of connected characters, parts of the symbols were missed by cropping characters individually. To deal with this problem, instead of identifying characters separately, we need to recognize consecutive characters simultaneously.

There were 'odoriji' (Japanese iteration mark) among the characters with low classification rate. For example, the classification rate was 12.4% (=21/169) and 17.3% (=14/81) for character "ゝ" (Unicode: U+30FD) and character "ゞ" (Unicode: U+303B), respectively. 'Odoriji' was used to represent repeated occurrences of the previous character. There are several types of 'odoriji', and a rule dictates that the character differs based on previous characters. However, some 'odoriji' characters are similar in appearance even as they are assigned separate character codes. Moreover, there are other characters similar in appearance to 'odoriji', such as "し (之)" or "く (久)". For these reasons, many 'odoriji' characters were not correctly classified. To classify separate 'odoriji', we must examine the previous symbol, and make a decision based on context, particularly for similar characters. Another reason for the accuracy drop in 'odoriji' is that some 'odoriji' images suffered quality distortions such as blur and defects.

Moreover, the classification rate for a character "っ" (Unicode: U+3063) was 0% (=0/11). All images of "っ" were misclassified as "つ", because "つ" and "っ" have an exactly identical shape. As it is difficult to identify these characters in isolation, it is necessary to determine the previous and following characters.

4.4 Use of context for actual transcription work

As mentioned in the previous section, simply recognizing characters using machine learning cannot solve the problems specific to 'kuzushiji' characters. In actual transcription process, it is important to eliminate false recognition as much as possible and leave only the correct recognition results. In addition, we found that when the maximum output probability values from softmax function tended to be low if character images, which were not correctly classified, were input to CNN. For the above reasons, in this study, we confirmed whether it was possible to eliminate erroneously classified characters with low maximum output probability values (hereinafter referred to as confidence values) by only using characters with high confidence values. Specifically, the confidence values were used as a threshold, and characters below the threshold were reserved as unknown characters. As shown in the paper[9], efficient transcription can be achieved by leaving low-confidence characters as "〓 ('geta')," and asking experts in the post-process to make a final judgment. When the recognition results of the original book is displayed as type, it is necessary to tell which characters have low confidence values to the following process. **Figure 12** shows an example of characters with low confidence values displayed in red rectangles for one page from a Japanese classical book called "飯百珍伝." An original

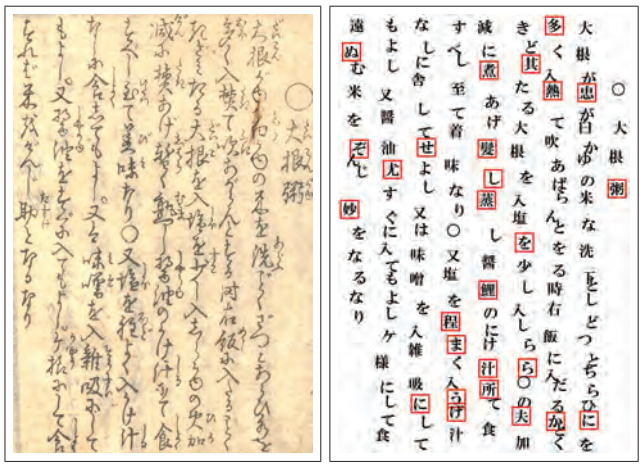

Fig. 12 Example of the recognition result of one page from "飯百珍伝"

image of "飯百珍伝" is shown on the left, and image showing the recognition results in print is shown on the right. On the right of Fig. 12, characters with confidence values of less than 50% are surrounded by red rectangles. This function will be easier for the post-process to estimate the characters with low confidence values from the previous and next characters with high confidence values.

5. Summary and Future Work

In this paper, we discussed the experiments we conducted to classify Japanese cursive 'kuzushiji' characters using a large-scale dataset. Here we summarize our three contributions as follows.

First, we showed the experimental results of 'kuzushiji' classification for 1,195 character classes using deep learning. By augmenting data for classes with a limited number of training samples, we achieved relatively high performance despite the huge number of classes: the classification rate was 88.98%, and the average classification rate over all classes was 78.02%. This results could not be directly compared with related works, because the database used and the number of classes were significantly different. But the task we worked on was much more difficult than the previous work because of two reasons: (1) recognizing 1,195 classes of characters is more difficult than recognizing approximately 50 'hiragana' characters, and (2) the number of images between classes were unbalanced. Therefore, the performance of our method can be considered good enough in this difficult environment.

Second, we identified certain root causes of poor performance for specific characters that could not be classified correctly using deep learning. For instance, when we looked at the incorrectly classified images, there were identical characters whose appearances differ greatly. This was caused by separate deformation caused by different 'jibo'. There were also 'odoriji' characters that differ based on previous characters. To deal with these prolems specific to 'kuzushiji' characters, we will have to make use of previous and subsequent characters. Thus, we will plan to recognize characters at word-level, phrase-level, or sentence-level. It is necessary to introduce new approaches based on expert knowledge of Japanese classical literature in addition to strengthening machine learning techniques. Another future work for using expert knowledge is to create a new dictionary of 'kuzushiji' characters by dividing identical character code into multiple 'jibo', or separating data depending on the era.

Third, we considered the actual transcription process and proposed a method to automatically judge either the system or the expert should make a final decision. This was achieved by using the maximum output probability of CNN. Using this method, experts can see which characters should be checked by their eyes to alleviate the misjudgement. When experts make a final decision, they can see the results of the previous and next characters. Therefore, this method will be able to help make the transcription process easier and faster.

References

1) Y. LeCun, B. Boser, J. S. Denker, D.Henderson, R. E. Howard, W. Hubbard, L. D. Jackel: "Backpropagation Applied to Handwritten Zip Code Recognition", Neural Computation, Vol.1, No.4, pp.541–551 (1989).
2) Y. LeCun, L. Bottou, Y. Bengio, P. Haffner: "Gradient-Based Learning Applied to Document Recognition", Proc. of the IEEE, Vol.86, No.11, pp.2278–2324 (1998).
3) T. Hayasaka, W. Ohno, Y. Kato, K. Yamamoto: "Recognition of Hentaigana by Deep Learning and Trial Production of WWW Application", Proc. of Information Processing Society of Japan (IPSJ) Symposium , pp.7–12 (2016). (in Japanese)
4) K. Ueda, M. Sonogashira, M. Iiyama: "Old Japanese Character Recognition by Convolutional Neural Net and Character Aspect Ratio", ELCAS Journal, 3: pp.88–90 (2018). (in Japanese)
5) H. T. Nguyen, N. T. Ly, K. C. Nguyen, C. T. Nguyen, M. Nakagawa: "Attempts to Recognize Anomalously Deformed Kana in Japanese Historical Documents", Proc. of International Workshop on Historical Document Imaging and Processing (HIP 2017) (2017).
6) A. Graves, S. Fernández, J. Schmidhuber: "Bidirectional LSTM Networks for Improved Phoneme Classification and Recognition", Artificial Neural Networks: Biological Inspirations (ICANN 2005), Vol.3697, pp.799–804 (2005).
7) A. Graves, S. Fernnández, F. Gomez, J. Schmidhuber: "Connectionist Temporal Classification: Labelling Unsegmented Sequence Data with Recurrent Neural Networks", Proc. of the 23rd International Conference on Machine Learning, pp.369–376 (2006).
8) T. Clanuwat, M. B.-Irizar, A. Kitamoto, A. Lamb, K. Yamamoto, D. Ha: "Deep Learning for Classical Japanese Literature", arXiv:1812.01718 (2018).
9) S. Yamamoto, and O. Tomejiro: "Labor Saving for Reprinting

Japanese Rare Classical Books", Journal of Information Processing and Management, Vol.58, No.11, pp.819–827 (2016). (in Japanese)

(Received September 11, 2019)
(Revised January 11, 2020)

Kazuya UEKI (*Member*)
He received a B.S. in Information Engineering in 1997, and a M.S. in the Department of Computer and Mathematical Sciences in 1999, both from Tohoku University, Sendai, Japan. In 1999. he joined NEC Soft, Ltd, Tokyo, Japan. He was mainly engaged in research on face recognition. In 2007, he received a Ph.D from Graduate School of Science and Engineering, Waseda University, Tokyo, Japan. In 2013, he became an assistant professor at Waseda University. He is currently an associate professor in the School of Information Science, Meisei University. His current research interests include pattern recognition, video retrieval, character recognition, and semantic segmentation. He is researching on the video retrieval evaluation benchmark (TREVID) sponsored by National Institute of Standards and Technology (NIST), and is contributing to the development of video retrieval technology. In 2016 and 2017, his submitted system achieved the highest for the second consecutive year in the TRECVID AVS task.

Tomoka KOJIMA
She is a third-year student in the School of Information Science, Meisei University. She has been studying on 'kuzushiji' recognition since the first year in University. Her current research interests include 'kuzushiji' recognition and Japanese classical literature.

IIEEJ Paper -- Special Issue on Extended Papers Presented in IEVC2019 --

Elastic and Collagen Fibers Segmentation Based on U-Net Deep Learning Using Hematoxylin and Eosin Stained Hyperspectral Images

Lina SEPTIANA†, Hiroyuki SUZUKI††, Masahiro ISHIKAWA‡(*Member*), Takashi OBI††,
Naoki KOBAYASHI‡(*Fellow*), Nagaaki OHYAMA††, Takaya ICHIMURA‡‡, Atsushi SASAKI‡‡,
Erning WIHARDJO§, Harry ARJADI§§

†Tokyo Institute of Technology, Department of Information and Communication Engineering,
††Tokyo Institute of Technology, Research Institute for Innovation in Science and Technology,
‡Saitama Medical University, Faculty of Health and Medical Care, ‡‡Saitama Medical University, Faculty of Medicine,
§Krida Wacana Christian University, Faculty of Engineering and Computer Science, Indonesia,
§§Indonesian Institute of Sciences, Research Center for Quality System and Testing Technology (P2SMTP-LIPI), Indonesia.

<Summary> In Hematoxylin and Eosin (H&E) stained images, it is difficult to distinguish collagen and elastic fibers because these are similar in color and texture. This study tries to segment the appearance of elastic and collagen fibers based on U-net deep learning using spatial and spectral information of H&E stained hyperspectral images. Groundtruth of the segmentation is obtained using Verhoeff's Van Gieson (EVG) stained images, which are commonly used for recognizing elastic and collagen fiber regions. Our model is evaluated by three cross-validations. The segmentation results show that the combination of spatial and spectral features in H&E stained hyperspectral images performed better segmentation than H&E stained in conventional RGB images compare to the segmentation of EVG stained images as ground truth by visually and quantitatively.

Keywords: pathology image, Hematoxylin Eosin (H&E), Verhoeff's Van Gieson (EVG), U-net, hyperspectral, segmentation

1. Introduction

Specimen staining is one important process in pathology diagnosis. The color information produced from tissue structure can show the tissue condition, which is useful for further analysis. Standard staining methods in pathology diagnosis is Hematoxylin and Eosin (H&E) stain, it is used to show the morphological structure of tissue[1]. This staining method is always done in histology processing.

An obvious correlation between the abnormality of elastic fibers and diseases was reported in medical papers[2)-4)]. Specifically, it is important for the diagnosis of pancreatic ductal carcinoma to the quantified measurement of specific density and distribution of elastic fibers in the walls of vessels and ducts associated with the tumor phenomenon[4]. Commonly, Verhoeff's Van Gieson (EVG) stained image is being used to recognize elastic fiber from collagen fiber for pathological diagnosis using microscopic observation. EVG stained images can discriminate elastic and collagen fibers easily with not only human eyes but also computer analysis, because EVG stained images have significant color differences between elastic and collagen fibers. It has been reported that the usage of Linear Discriminant Analysis (LDA) on EVG stained image based on three color features can produce good classification results between elastic and collagen fibers[5]. However, in pathology diagnosis, the EVG stain is an additional staining method, and it is produced while the H&E stain has been done. It means that to produce the EVG stain needs an extra additional effort than the H&E stain both in the staining process and in cost[6]. Therefore, we approach the possibility to distinguish elastic fibers from collagen ones using H&E stained images to improve the efficiency in pathology diagnosis.

However, the appearance of elastic fibers is not easy to be recognized from conventional H&E stained RGB image with three color bands due to the similar color and pattern with collagen fibers. Hence we use hyperspectral imaging systems that can analyze tissue samples in more narrow and various wavelength bands than using general RGB cameras. The hyperspectral image provides valuable and comprehensive information about the object characteristic on biomedical tissues[7)-12)] , and it can be potentially used to recognize the elastic and collagen fibers from H&E stained images, which might include a small color difference between elastic and collagen regions. Therefore, we investigate the possibility of distinguishing elastic and collagen fibers without EVG stained specimens but with H&E stained ones by applying hyperspectral image analysis.

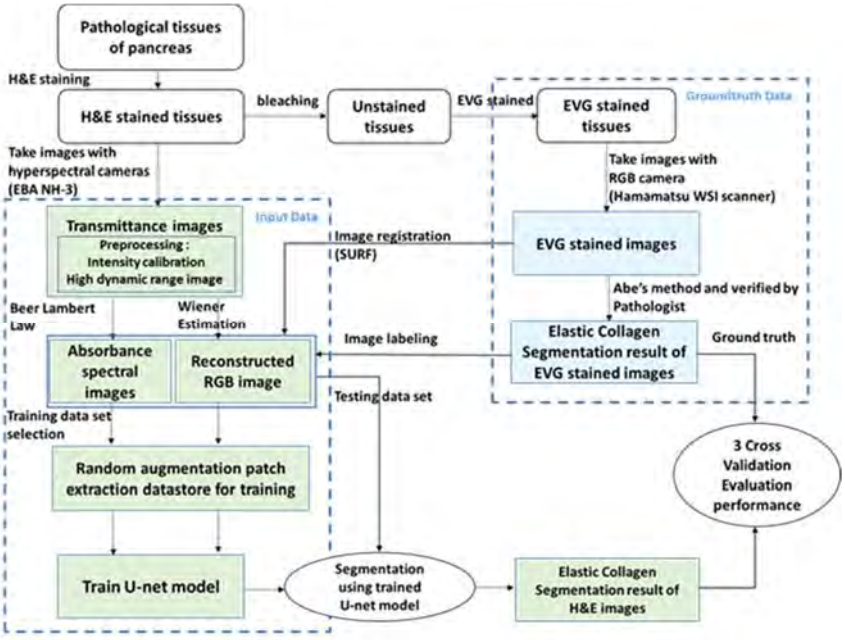

Fig.1 Block diagram of proposed method

In our previous study, we did the pixel-wise classification of elastic and collagen fibers from H&E stained hyperspectral images of pancreatic tissues using spectral information, we showed that spectral data was more effective in classifying those elastic and collagen fibers regions by applying Linear Discriminant Analysis (LDA) compare to RGB images.

Continuing our study[12], we consider the fact that commonly elastic fibers exist in specific areas[13], i.e., in blood vessel wall regions. Different from elastic fibers, collagen fibers may exist in almost all connective tissue[13]. Hence the spatial feature provides meaningful information to distinguish elastic and collagen fibers. Beside of that, the previous research by Ushiki[14] had observed the micro-level texture with the high magnification about differences between elastic and collagen fibers. It found some significant differences in basic structure and arrangement between elastic and collagen fibers based on a morphological viewpoint in high-resolution images. It means that the effective differences of textures for elastic and collagen fiber might be shown in normal pathological magnification images (20x)[14][15]. Besides that, the absorbance intensities of images have different values in every different wavelength, therefore the texture differences of elastic and collagen fibers can be more emphasized in hyperspectral image[16]-[18]. For those reasons, in this study, we propose a pixel-wise classification method using not only spectral features but also the combination of spectral and spatial features of H&E stained hyperspectral images. This method can provide more comprehensive information to increase classification accuracy.

The difficulty of applying the combination of spectral and spatial information to the classification of elastic and collagen fibers is that both features have different scales and units. The use of conventional machine learning method such as Linear Discriminant Analysis (LDA) needs lots of calculations for getting many spatial features in images corresponding to each wavelength to map and to fuse both features. It means hyperspectral images needs much significant processing times compared to RGB images in conventional machine learning method[19],[20].

Refer to the previous study[21], U-net is a powerful segmentation technique for medical images based on spatial and channel features. The network works by processing spatial and spectral information in contracting and expansive path. U-net enables to train spatial and spectral features automatically without any redundancy from many calculations process as happened in conventional machine learning. U-net also works well using only a few number image samples, with small and thin image boundaries. For these reasons, we employ U-net based architecture to investigate the combination of spectral and spatial features for classification of elastic and collagen fibers using H&E hyperspectral images.

For quantitative evaluation, the segmentation accuracy is confirmed visually and quantitatively by comparing ground truth based on EVG stained images with Abe's method[5], which have been corrected by the pathologist.

2. Proposed Method

Figure 1 shows the pipeline of our proposed method for elastic and collagen segmentation in the H&E stained

image. Procedures in this study consist of several steps, i.e., image acquisition, preprocessing, training, segmentation, and verification. Details of the above procedures are described in the following sections.

2.1 Image acquisition

Human pancreas tissues of H&E stained specimen and its EVG images were provided by BioMax Inc. These tissues were collected under the highest ethical standards, with the donor being informed completely with their consent and collected under HIPPA approved protocols. Two types of stained images have almost the same biological structures because the EVG stained specimens were obtained by dying unstained specimens that were obtained by bleaching the H&E stained specimens.

H&E hyperspectral images were captured by an optical microscope (Olympus BX-53) with a halogen lamp as the light source and a 61 band hyperspectral camera from EBA Japan NH-3, with 20x magnification, one pixel has dimensions 0.25x0.2758 μm^2, image size is 120x207.4 μm^2 or 480 x 752 pixels, wavelength range is 420nm to 720nm with 5nm wavelength interval. We did intensity calibration to take into account the difference in the spectrum of light sources and generated a high dynamic range image by replacing the overexposure part of the image with the lower one. EVG stained tissues were captured by using Hamamatsu Whole Slide Image (WSI) scanner as RGB image.

To make the object recognition on H&E stained specimen easier to be analyzed, we used absorbance spectral images, which were converted from a captured transmittance hyperspectral images, based on Beer-Lamber law equation as follows[16)-18)],

$$I_{a_i}(\lambda) = -\log\left\{\frac{I_i(\lambda)}{I_{o_i}(\lambda)}\right\}, \quad (1)$$

where $I_{a_i}(\lambda)$ is absorbance spectra, $I_i(\lambda)$ is a captured transmittance spectra, and $I_{o_i}(\lambda)$ incident spectral of ith pixel.

Figure 2 shows the intensity of absorbance spectra from some random pixel points in H&E hyperspectral image, blue and red lines denote elastic and collagen fibers, respectively. Those spectral information show more comprehensive information with small color differences than the RGB images which has only three channel bands.

We also generated H&E stained RGB images from the hyperspectral image by employing Wiener estimation[22)23)], to compare the performance of classification using hyperspectral images to RGB images.

As a pre-process to classify elastic and collagen fiber using H&E stained image, we employ image registration method based on Speed up robust features (SURF)[24)] to trace the fiber region of the EVG image to corresponding

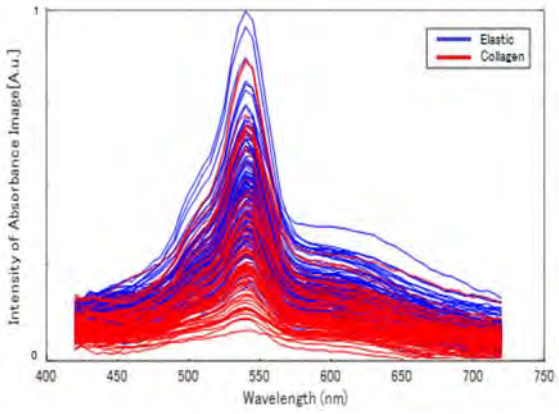

Fig.2 Absorbance spectrum of elastic and collagen samples obtained from H&E stained hyperspectral images

one of an H&E stained image. To obtain the ground truth images, we make segmentation of EVC images using Abe's method[5)] and identified elastic and collagen fiber regions. Two of our author members who are pathologists from Saitama Medical University verified these results, and the appropriateness of Abe's method was confirmed. Thus, we use it to get labels of elastic and collagen fiber.

In this study, we focus on the classification of elastic and collagen fibers only, because it is most difficult for pathologists to distinguish these two components in H&E stained image, which have a very similar color and pattern. The other components, i.e. cytoplasm and nucleus can be recognized easily by pathologists as these have different patterns or colors. For this reason, we extract the region of interests (ROIs), which contain both elastic and collagen fiber areas in H&E stained images by applying Abe's method on EVG stained image which used as a label. After extracting the fiber regions, we classify the elastic and collagen fibers from the ROIs.

2.2 U-net based classification method for spatial-spectral features

In this study, we use a U-net[21), 25)] based architecture, as seen in **Fig. 3.** A blue box represents a multi-channel feature map, and a number on the top of each box denotes the number of channels. Another number at the lower-left edge of the box denotes the image size. A white box denotes the copied feature map. The proposed network architecture using 61 feature channels, consists of a downsampling path and an upsampling path. The downsampling path employs 3x3 zero-padded convolutions, which treats the edge area of the input image by zero to keep the patch size as it is. The 3x3 zero-padded convolution is repeated twice for each feature map, and then the convolution results are modulated by a rectified linear unit (ReLU), as shown in the blue arrow.

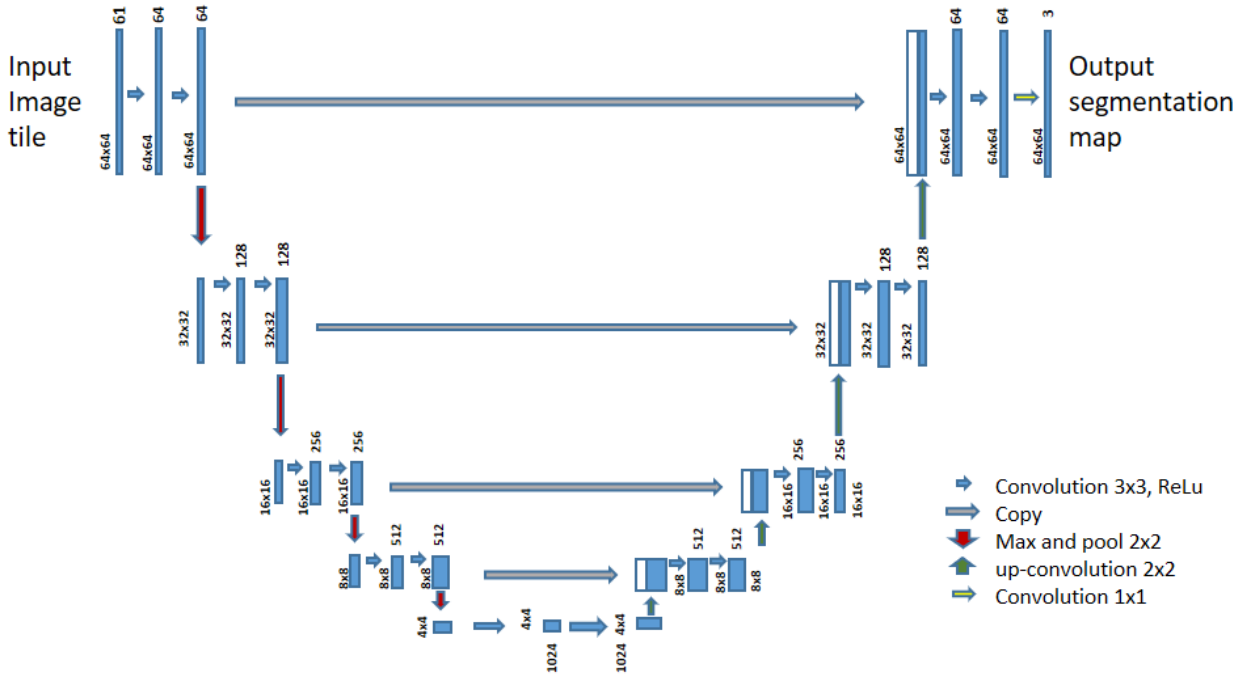

Fig. 3 U-net based architecture for elastin and collagen segmention using H&E stained hyperspectral images

In this process, we extend the number of feature channels from 61 to 64, because 64 feature channels are standards for U-net architecture[5] , which is commonly used. After that, a 2x2 max pooling operation is employed shown in the red arrow. In the second layer, we double the number of feature channels from 64 to 128 at each downsampling step. For the upsampling path, each step of the feature map is followed by a 2x2 convolution that divides the feature channels number into half, a concatenation with the corresponding feature map from the downsampling path, and two 3x3 convolutions and modulations by a ReLU. At the final layer, a 1x1 convolution is used, it is not looking at anything around itself. It is used only to reduce the number of feature channels.

The details of the U-net based architecture, such as the selected optimum parameters for the histopathology analysis are as follows:

- We use hyperspectral images with 61 channels to feed the U-net architecture. Input images are small patch images, including elastic and collagen fiber regions, which are crapped from H&E stained images. Output images are 3 channels, elastic fiber, collagen fiber, and the other component.
- The filter size for convolution is 3x3. It is the most suitable size to preserve the small and thin structures in the image, according to the previous study[26].
- The patch size is 64 × 64. The smaller size will reduce the accuracy of the machine learning, while the bigger size will increase the processing time as the accuracy is keeping the same level. In this experiment, for each cross-validation, 36 patches are prepared from 2 images (18 patches per image) samples. They are trained randomly as many as 100 and 1,000 patches from those 36 patched data, using reflection and 90-degree rotation augmentation image, it produces 1600, and 16,000 augmentation patches respectively from 100 and 1,000 patches (16 variant patch per image), which effectively increase the segmentation performance with a small number of training data.
- Initial Learning rate 0.001, epoch 5, those for the optimal learning process with the minimum processing time
- We propose to use U-net pre-trained model which was trained using remote sensing multispectral dataset[27] firstly before used in this segmentation[28].

3. Experiments

3.1 Sample tissue mages

We used three sample tissue images for three-fold cross-validations, as shown in **Fig. 4**. In the figure, group(a) and group(b) show H&E stained images and EVG

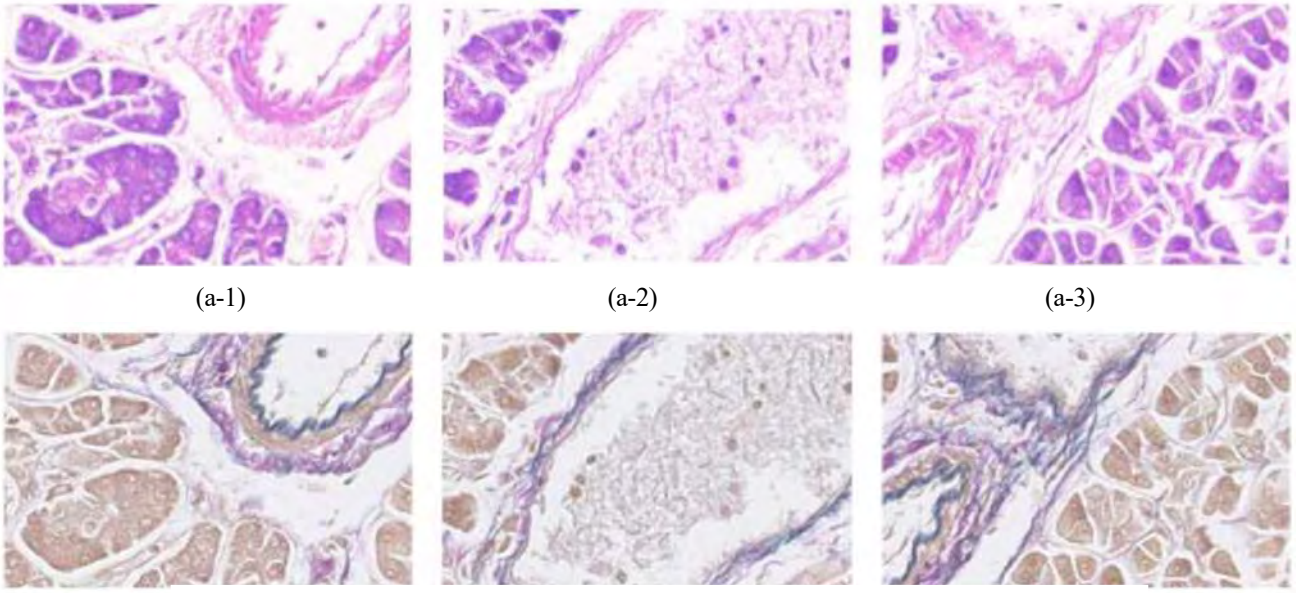

Fig. 4 H&E stained images of sample 1,2,3: (a-1), (a-2), (a-3); and EVG stained images of sample 1,2,3:(b-1), (b-2), (b-3)

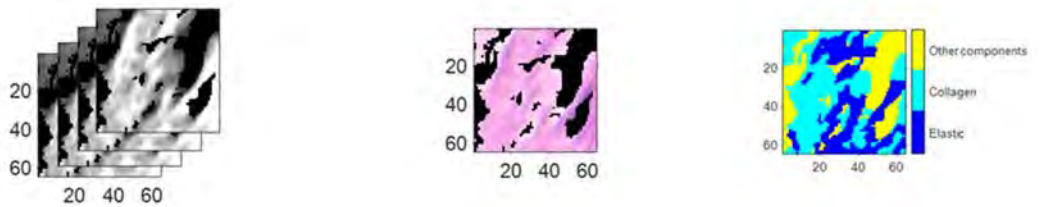

Fig. 5 64 × 64 patch (a) Hyperspectral image (4 band images are extracted from 61 band ones), (b) Corresponding RGB image, (c) Label

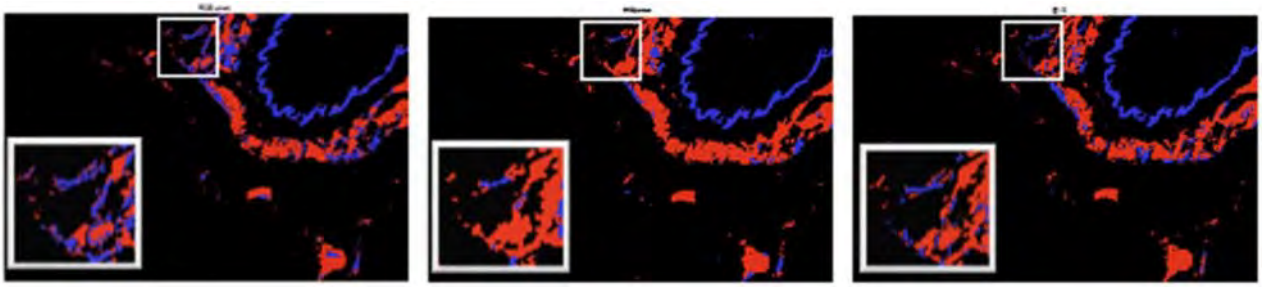

Fig. 6 Cross-validation 1 segmentation result (a) RGB image, (b) Hyperspectral image, (c) Groundtruth image

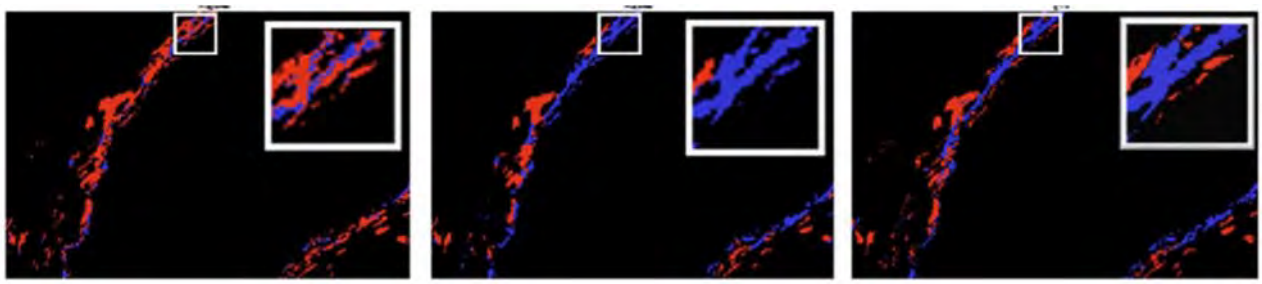

(a) (b) (c)

Fig. 7 Cross-validation 2 segmentation result: (a) RGB image, (b) Hyperspectral image, (c) Groundtruth image

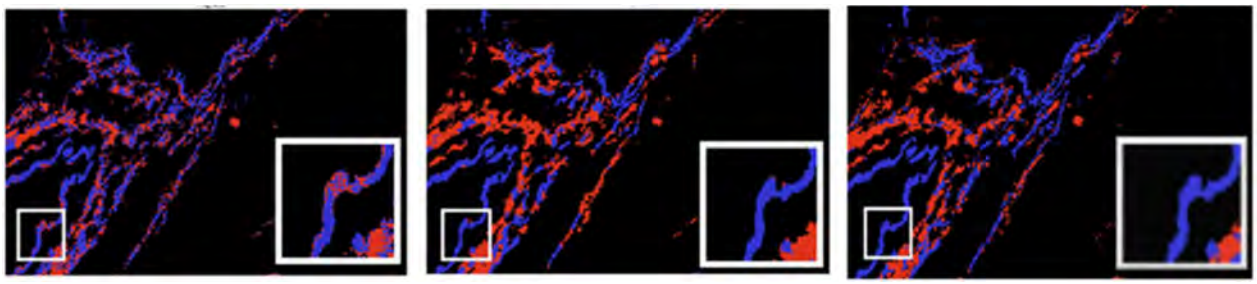

(a) (b) (c)

Fig. 8 Cross-validation 3 segmentation result: (a) RGB image, (b) Hyperspectral image, (c) Groundtruth image

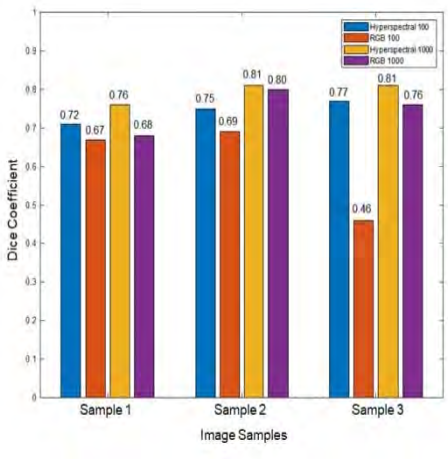

Fig. 9 Dice coefficients of hyperspectral and RGB images using spectral-spatial features (U-net)

stained images, respectively. We used three images for cross-validations as follows,

- Cross-validation 1: we extract the fiber area from samples 2 and 3, then be tested in sample 1.
- Cross-validation 2: we extract the fiber area from samples 1 and 3, then be tested in sample 2.
- Cross-validation 3: we extract the fiber area from samples 1 and 2, then be tested in sample 3.

Training process use parameter mentioned in section 2.2. **Figure 5** (a)-(c) show examples of 64×64 patch of a hyperspectral image, a corresponding RGB image, and its label, respectively. The label in (c) consists of three classes, i.e., elastic, collagen, and other components obtained by applying Abe's method to EVG stained images[5] and corrected by the pathologist.

3.2 Segmentation result

We obtained segmentation results of elastic and collagen fiber regions using three cross-validations. We compared the segmentation result of the hyperspectral images to the conventional RGB images.

Figure 6, 7 and **8** show the results of segmentation using cross-validation 1,2 and 3, respectively. In each figure, (a) and (b) denote segmentation result images obtained from hyperspectral and RGB images, respectively, and (c) denotes

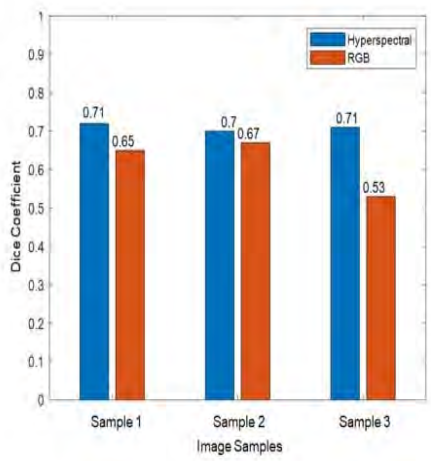

Fig. 10 Dice coefficients of hyperspectral and RGB images using spectral features (LDA)

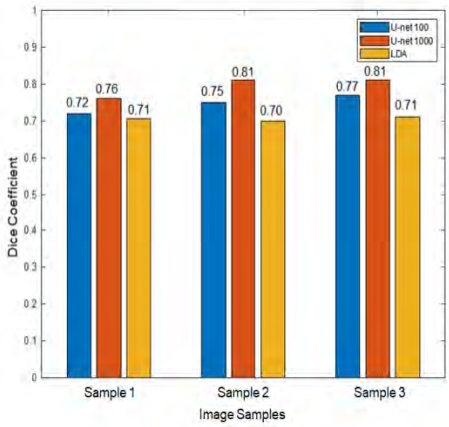

Fig. 11 Dice coefficients of hyperspectral images using spectral-spatial features (U-net) and spectral features (LDA)

a ground truth image obtained from EVG stained image[5]. The blue and red color represents elastic and collagen fiber, respectively. These results show that RGB results have more misclassification than hyperspectral images compared to ground truth images.

We also evaluate the segmentation results quantitatively by calculating the classification accuracy using the following equation[29],

$$\text{Dice Coefficient} = \frac{2TP}{2TP+FP+FN} \qquad (2)$$

True Positive (TP) is the number of pixels where elastic fibers are decided as elastic fiber correctly, False Positive (FP) is the number of pixels where collagen fibers are decided as elastic fibers incorrectly, and False Negative (FN) is the number of pixels where elastic fibers are decided as collagen fibers incorrectly in the segmented images.

red bars show the dice coefficients of RGB images for 100 patches, yellow bars show the dice coefficients of hyperspectral images for 1,000 patches, and purple bars show the dice coefficients of RGB images for 1,000 patches. From these data, we can see that the proposed U-net using hyperspectral images performs better than RGB both using 100 and 1,000 patch numbers.

4. Discussion

In section 3, it has been observed that the proposed method has a significantly better performance than RGB images . Also, we compared the proposed method based on spectral-spatial features to the previous sudy based on spectral features [12].

Table 1 Average learning time

Number of patch images	Average learning time
100	200 [sec]
1,000	1,850 [sec]

Figure 10 shows the dice coefficients of hyperspectral and RGB images using spectral features with LDA. Blue bars show the dice coefficient of the hyperspectral images, and red bars show the dice coefficient of RGB images.

Figure 11 shows the dice coefficients of hyperspectral images using spectral-spatial features with U-net and hyperspectral images using spectral features with LDA. Blue and red bars show the dice coefficients of U-net using 100 and 1000 patches, respectively, and yellow bars show the dice coefficients of LDA.

These results indicate that the segmentation of elastic and collagen fibers using hyperspectral images perform better results than RGB images in case of both using the spectral feature only and the combination of spectral-spatial features. In a comparison of spectral-spatial features with U-net and spectral features with LDA, the former ones can classify the elastic and collagen fiber regions with better accuracy. These results were also subjectively evaluated by pathologists from Saitama Medical University, and they gave comments that the segmented images were almost equivalent to the diagnostic outcome by pathologists, and the results of spectral-spatial features with U-net were especially well-classified.

Table 1 shows the average learning time for validations in this experiment. The software for calculation is Matlab 2019a, and the processor is NVIDIA™ Titan X. This result shows that 1000 patch images take more than 9 times of 100 patch images, whereas data size of training is 10 times.

This experiment is our first trial for the segmentation of elastic and collagen fibers. Thus, the developed U-net might have much room to improve because we have tried only a few kinds of parameters such as the architecture of U-net, type of input data, number of training data set, and so on. If we will repeat more trial-and-errors, it is sure that the accuracy will increase.

5. Conclusion

In H&E stained images, it is difficult to distinguish collagen and elastic fibers because these are similar in color and texture.This study observed the segmentation of elastic and collagen fibers from the H&E stained images through hyperspectral transmittance using U-net based spectral-spatial analysis. Groundtruth of the segmentation is obtained using EVG stained images, which are commonly used for recognizing elastic and collagen fiber regions. Our model is evaluated by three cross-validations. The segmentation results show that the combination of spatial and spectral features in H&E stained hyperspectral images performed better segmentation than H&E stained conventional RGB images both in visual appearance and quantitative verification.

This method is not only for visualization but also for pixel wise classification. We believe that this method may help the diagnostic accuracy increase.

Acknowledgment

The authors appreciate to Indonesia Endowment Fund for Education (LPDP) and Join research program between Japan Society for the Promotion of Science (JSPS) and Indonesian Institute of Sciences (LIPI), for providing financial support.

References

1) M. Titford: “The Long History of Hematoxylin”, Biotechnic & Histochemistry. Vol.80 , No.2, pp.73–78 (2005).

2) J. Uitto, L. Ryhanen, P.A. Abraham, A.J. Perejda: “Elastin in Diseases”, The Journal of Investigative Dermatology, Vol. 79, Issue 1, Supplement, pp.160–168 (1982).

3) Y. Yasui, T. Abe, M. Kurosaki, M. Higuchi, Y. Komiyama, T. Yoshida, T. Hayashi, K. Kuwabara, K. Takaura, N. Nakakuki, H. Takada, N. Tamaki, S. Suzuki, H. Nakanishi, K. Tsuchiya, J. Itakura, Y. Takahashi, A. Hashiguchi, M. Sakamoto, N. Izumi: “Elastin Fiber Accumulation in Liver Correlates with the Development of Hepatocellular Carcinoma”, PloS one, Vol.11, No.4, e0154558 (2016).

4) E.Lakiotaki, S. Sakellariou, K, Evangelou, G. Liapis, E. Patsouris, I. Delladetsima, Vascular and Ductal Elastotic Change in Pancreatic Cancer, Acta Pathologica, Microbiologica et Immunologica Scandinavica, John Wiley and Son (2015).

5) T. Abe, A. Hashiguchi, K. Yamazaki, H. Ebinuma, H. Saito, H. Kumada, N. Izumi, N. Masaki, M. Sakamoto: “Quantification of Collagen and Elastic Fibers Using Wholeslide Images of Liver Biopsy Specimens”, Pathology International Vol.63, Issue 6, pp 305–310, QA, June (2013).

6) www.polyscience.com, accessed on 12 October (2019)

7) M. Ishikawa, C. Okamoto, K. Shinoda, H. Komagata, C. Iwamoto, K. Ohuchida, M. Hashizume, A. Shimizu, N. Kobayashi: “Detection of Pancreatic Tumor Cell Nclei via a Hyperspectral Analysis of Pathological Slides Based on Stain Spectra”,Biomedical Optics Express, Vol. 10, No. 9, pp.4568–4588 (2019).

8) D. L. Farkas, C. Du, G. W. Fisher, C. Lau, W. Niu, E. S. Wachman, R. M. Levenson: “Non-invasive Image Acquisition and Advance Processing in Optical Bioimaging”, Computerized Medical Imaging and Graphics Vol. 22, No.2, pp.89–102 (1998).

9) B. C. Wilson, S. L. Jacques: “Optical Reflectance and Transmittance of Tissues: Principles and Applications”, IEEE Journal of Quantum Electronics; Vol.26, Issue 12, pp.2186–98 (1990).

10) G. Lu, J. V. Little, X. Wang, H. Zhang, M. R. Patel, C. C. Griffith, M. W. El-Deiry, A. Y. Chen, B. Fei: “Detection of Head and Neck Cancer in Surgical Specimens using Quantitative Hyperspectral Imaging”, Clin Cancer Res.; 23(18): pp.5426–5436. September 15 (2017).

11) P. A. Bautista, T. Abe, M. Yamaguchi, Y. Yagi, N. Ohyama: “Digital Staining for Multispectral Images of Pathological Tissue Specimens Based on Combined Classification of Spectral Transmittance”, Computerized Medical Imaging and Graphics Vol.29, Issue 8, pp. 649–657 (2005).

12) L. Septiana, H. Suzuki, M. Ishikawa, T. Obi, N. Kobayashi, N. Ohyama, T. Ichimura, A. Sasaki, E. Wihardjo, D. Andiani: “Elastic and Collagen Fibers Discriminant Analysis using H&E Stained Hyperspectral Images”, Journal of Optical Review, Vol. 26, Issue 4, pp. 369–379. Springer (2019).

13) V. P. Eroschenko, S. H. Mariano: “DiFiore's Atlas of Histology with Functional Correlations”, 12th ed. Philadelphia, PA: Wolter Kluwer Health/Lippincott Williams and Wilkins (2013).

14) T. Ushiki, Collagen Fibers: “Reticular Fibers and Elastic Fibers. A Comprehensive Understanding from a Morphological Viewpoint”, Arch. Histol. Cytol., Vol. 65, No. 2 (2002).

15) T. L. Sellaro, R. Filkins, C. Hoffman, J. L. Fine, J. Ho, A. V. Parwani, L. Pantanowitz, M. Montalto: “Relationship between Magnification and Resolution in Digital Pathology Systems”, Journal of Pathology Informatics, (22 Aug.) Wolters Kluwer-Medknw (2013).

16) D. L. Omucheni, K. A. Kaduki, W. D. Bulimo, H. K. Angeyo: “Application of Principal Component Analysis to Multispectral-Multimodal Optical Image Analysis for Malaria Diagnostics”, Malaria Journal, 13:485 (2014).
17) L. Septiana, H. Suzuki, M. Ishikawa, T. Obi, N. Kobayashi, N. Ohyama: “Staining Adjustment of Dye Amount to Clarify the Appearance f Fiber, Nuclei, and Cytoplasm in HE-stained Pathological Kidney Tissue Image”, International Multidiciplinary Conference and Productivity and Sustainability, Ukrida press (2017).
18) T. Abe, Y. Murakami, M. Yamaguchi, N. Ohyama, Y. Yagi : “Color Correction of Pathological Images Based on Dye Amount Quantification”, Optical Review 12: 293 (2005).
19) H. Yuan, Y. Y. Tang, Y. Lu, L. Yang, H. Luo: “Spectral-Spatial Classification of Hyperspectral Image Based on Discriminant Analysis”, IEEE Journal of Selected Topics in Applied Earth Obsevations and Remote Senssing Vol. 7, Issue 6, pp.2035–2043, June (2014).
20) M. Fauvel, J. A. Benediktsson, J. Chanussot, J. R. Sveinsson: “Spectral and Spatial Classification of Hyperspectral Data Using SVMs and Morphological Profiles”, IEEE Trans. on Geoscience and Remote Sensing, Vol.46, No.11, November (2008).
21) O. Ronneberger, P. Fischer, T. Brox: “U-Net: Convolutional Networks for Biomedical Image Segmentation”, Computing Research Repository (CoRR), abs/1505.04597 (2015).
22) M. Stokes, M. Anderson, S. Chandrasekar, R. Motta: “A Standard Default Color Space for the Internet sRGB”, Microsoft and Hewlett-Packard Joint Report, November 5 (1996).
23) H. L. Shen, P. Q. Cai, S. J. Shao, J. H. Xin : “Reflectance reconstruction for multispectral imaging by adaptive Wiener estimation”, Optics Express, Vol 15, Issue.23, pp.15545-15554, Nov. (2007).
24) Mathwork. (2018). “Computer Vision System Toolbox Documentation” (r2018). Retrieved December 15, (2018).
25) Mathwork, (2019). “Semantic Segmentation of Multispectral Images using Deep Learning”, Image Processing Toolbox document R2019a.Retrieved March 28, (2019).
26) P. S. Chavez, B. Bauer: “An Automatic Optimum Kernel-Size Selection Technique for Edge Enhancement”, Remote Sensing Of Environment Vol.12, Issue 1, pp.23–38 (1982).
27) http://www.cis.rit.edu/~rmk6217/rit18_data.mat, Retrieved December 28, (2018).
28) R. Kemker, C. Salvaggio, C. Kanan: “High-Resolution Multispectral Dataset for Semantic Segmentation”, Computing Research Repository (CoRR), abs/1703.01918. (2017).
29) A. A. Taha, A. Hanbury: “Metrics for Evaluating 3D Medical Image Segmentation: Analysis, Selection, and Tool”, BMC Medical Imaging 15:29, (2015).

(Received July 27, 2019)
(Revised December 24, 2019)

Lina SEPTIANA
She received B.Eng degree from Electronic Eng. Dept., Satya Wacana Christian Univ., Indonesia. M. Sc degree from Electrical Eng. and Computer Science Dept., Chung Yuan Christian Univ., Taiwan. Currently, she is a doctoral student in Information and Communication Eng. Dept. Tokyo Institute of Technology, Japan, and Lecturer at Engineering and Computer Science Fac. Krida Wacana Christian Univ. Indonesia.

Hiroyuki SUZUKI
He received B.E., M.E., and Ph.D. degree from Tokyo Inst. of Tech. in 1998, 2000, and 2006, respectively. He was a Reseacher from 2003 to 2016. He has been an Assistant Professor with Institute of Innovative Research, Tokyo Inst. of Tech since 2016. His research interests include optical information security, hologram, biometric authentication, and medical healthcare information system.

Masahiro ISHIKAWA *(Member)*
He received a Ph.D degree from Niigata University, Japan in 2006. He is currently an Assistant Professor at the Saitama Medical University. His current research interests include image processing and computer aided diagnosis.

Takashi OBI
He earned B.S. degree in Physics, M.S. and Ph.D. degree in Information Physics from Tokyo Inst. of Tech, Japan in 1990, 1992, and 1996 respectively. Currently, he is an Associate Professor of Laboratory for Future Institute of Innovative Research, Tokyo Inst. of Tech. His Research focuses on medical informatics, information system and security, etc. He is a member of IEICE, JAMIT, JSAP, JSNM, JSMP, and IEEE.

Naoki KOBAYASHI *(Fellow)*
He earned B.Sc., M.E. degree from Tokyo Inst. of Tech, in 1979, 1981 respectively. Ph. D degree from Niigata Univ in 2000. He worked for NTT Lab. In 1981-2008. He has been at professor at School of Biomed. Eng, Fac. of Health and Medical Care, Saitama Medical Univ. since 2008. His research interests include medical image processing, image compression, and biosignal processing, He is a member of IECE, IIEEJ, JSMBE, and IEEE.

Nagaaki OHYAMA
He earned Doc. Eng. degree in Information Physics from Tokyo Inst. of Tech. in 1982. His academic career on Tokyo Inst. of Tech has been started since 1982. Become professor in Tokyo Inst. of Tech since 1993. His current research project is related to Japan government's information policy (formulation of electronic preservation standards for medical images, onlin request for claims, introduction of public personal authentication service, etc.)

Takaya ICHIMURA
He earned M.D., Ph.D. degress and is an assistant professor of the Saitama Medical University. He received the Ph.D. degree from Kumamoto University, Kumamoto, Japan, in 2005. His current research interests include nuclear atypia and the molecular nature of chromatin.

Atsushi SASAKI
He earned M.D., Ph.D. degrees from Gunma Univ. School of Medicine in 1980, 1984, respectively. He received the Neuropathology Best Paper Award in 2001, Brain Tumor Pathology Best Paper Award in 2002. He is currently a professor at the Dept. of Pathology, Saitama Medical Univ. His research interests include brain tumor pathology and microglia. Dr. Sasaki is a member of the International Society of Neuropathology and American Association of Neuropathologists.

Erning WIHARDJO
He earned B.Sc., M.Sc. in Physics from Padjajaran Univ. Indonesia in 1976. M. Eng in Opto-Electronics, Univ. of Indonesia in 1979. M. Eng., Doc. Eng. in Physical Information from Tokyo Inst. of Tech. in 1983 and 1986 respectively. He was a scientist at the Indonesia Inst. of Science and Polycore Optical. Ltd., Singapore in 1986-1995. He continued his career at Hoya Lens Ltd in 1995-2012, with the latest position as Director of Hoya Asia H.Q, Singapore. He was awarded professorship from the He Univ. of Ophthalmology and Visual Science, China in 2008. He is the president of Krida Wacana Christian. Univ. Indonesia 2016 - 2020.

Harry ARJADI
He is a senior scientist at Indonesian Institute of Sciences, Research Center for Quality System and Testing Technology (P2SMTP-LIPI), Indonesia. He earned B.Sc., in Physical Eng. from Bandung Inst. of Tech. Indonesia in 1981, M. Sc. In Electronic Intrumentation Design, Ph. D. in Bio-Electromagnetic from Salford Univ. U.K. in 1988 and 1992 respectively.

IIEEJ **Paper** *-- Special Issue on Extended Papers Presented in IEVC2019 --*

Pressure Sensitivity Pattern Analysis Using Machine Learning Methods

Henry FERNÁNDEZ† , Koji MIKAMI† , Kunio KONDO† (*Fellow*)

† Tokyo University of Technology

<**Summary**> As a consequence of a lack of balance between the levels of difficulty of a game and the players' skills, the resulting experience for players might be frustrating (too difficult) or boring (too easy). Players having a bad experience could impact game creators negatively, leading to irreparable damage. The main motivation of this study was to find effective ways to reduce the gap between skills and difficulty, to help developers create a more suitable experience for players. This paper shows the results of applying Neural Networks and Support Vector Machines to data collected from the pressure exerted to a gamepad's button with the purpose of finding patterns that can help predict: difficulty, fun, frustration, boredom, valence, arousal and dominance at a determined time. We obtained results with an accuracy of 83.64 % when predicting boredom, around 70 % of accuracy classifying frustration, fun, difficulty and dominance.

Keywords: game design, game development, pressure sensitivity, gamepad, machine learning, feelings, neural networks, support vector machines, behavioral pattern

1. Introduction

The ultimate goal of our research is to adapt the experience for players with different skills. We wanted to find new ways to correct the imbalance that sometimes appears in games due to differences between challenges' difficulty and the ability of players to overcome those challenges. A large gap between the players' skills and levels of difficulty for challenges that they encounter in a game, might impact the overall experience in a negative way, in consequence, making players quit[1)–4)]. Enjoyment, fun, engagement, have been topics of study for a wide range of researchers in the academia[5)–11)], we would like to contribute by exploring this topic using behavioral patterns and how they relate to the player's status and perceptions while playing.

So far we have been working with Dynamic Difficulty Adjustment, Procedural Content Generation and Brain Computer Interface applied to 2D platform games and the focus of those studies was to understand the possible relationships between player experience and perception of difficulty[12),13)]. Our second approach involves behavioral patterns, specifically, the relationship between the pressure exerted on a gamepad's button and players' emotions, including how players perceive the current status of the game.

We divided the problem in three steps: (1) data collection, (2) classification method and (3) difficulty adaptation. Step (1) has been already completed. Is constituted of an analysis of the data obtained from experiments in a 2D shooting game, demonstrating that there is a clear relationship between the evaluated parameters and the force exerted on the gamepad's button[14)]. This paper summarizes the results of step (2), in which we used the data collected from an experiment conducted with 20 different players and tested it with machine learning methods to understand the player's experience in real time. Using machine learning methods would help us to find patterns that could be used by developers to adapt in-game parameters according to what players are experiencing and improve the final result. Step (3) is part of our future work.

Support vector machines and neural networks are widely used to classify data and make predictions in real time[15)–17)]. For our specific problem, which involves behavioral patterns related data, emotions and player's perceptions, some researchers working on the same topic have achieved good results using machine learning methods[18)–20)], which is the main reason why we decided to use neural networks and support vector machines in our research.

Experiments were designed to make players interact as much as possible with the gamepad's button to be able to collect large amounts of data. Players played 6 levels

of a 2D space shooter, after finishing each level, questionnaires to measure their perception towards the game were applied. The parameters measured in the questionnaires are: difficulty, fun, frustration, boredom, valence, arousal and dominance. In addition, in-game data was collected for future analysis.

All the collected data was used with a set of different machine learning algorithms, three different types of neural networks and support vector machines for each parameter measured in the questionnaires were designed. We tested several times to obtain the best possible results and input values for each method. One of the clearest results of our analysis was that support vector machines can classify pressure sensitivity with better accuracy than neural networks, for neural networks with an average accuracy result of 68.55 % and for support vector machines, an average result of 70.69 %.

In this paper, our results also demonstrated that the easiest parameters to classify are: boredom (83.64 %), difficulty (72.17 %), dominance (71.13 %), frustration (70.27 %) and fun (70.14 %), and the rest of the results' accuracy was above 60 %. Although the way we analyzed the presented results and this previous research[19] are not exactly the same, we were able to achieve more than 60 % of accuracy for all parameters, while Chanel et al. AI could classify boredom, engagement and anxiety with 53.33 % of accuracy.

2. Related Work

In a previous research, Sykes et al. used a PlayStation 2 controller to measure pressure sensitivity and its correlation with arousal in experiments conducted using a clone of 'Space Invaders'[21]. This was one of the first known studies that proved that pressure sensitivity was directly related to the player's emotions. We decided to use some of the elements from this research, our experiment was conducted with a 2D shooter and a PlayStation 3 gamepad (with the same pressure sensitivity capability).

As a relevant result from the research of van den Hoogen et al., when players felt more aroused and dominant while playing a racing game they put more pressure on the controller, demonstrating the relationship between pressure and emotions[22]. Unlike our research, which is focused on the force applied to the button of a gamepad, these researchers measured the pressure on the controller itself, a different approach to measuring physical behaviors. The same group of researchers demonstrated that player experience can be quantified through the behavior of players, measuring the force applied to a keyboard, they obtained levels of arousal[23].

In previous studies, researchers designed a method to inform developers when a series of actions performed inside a game represent a frustrating event for players[24]. The focus of this research was to detect emotions such as boredom, frustration or the state of flow. Their method was specific for a particular game but we think that the approach could be used for a more general purpose.

For a different group of participants in a field not related to games, a group of programmers were analyzed by using biometric sensors and self-reports to classify their emotions[25]. They obtained an accuracy of 71.36 % and progress in 67.70 %, their research involved flow theory, boredom, basically the same parameters that we used in our study.

We designed the questionnaires for the experiments using Self-Assessment Manikin (SAM), which was successfully applied for studying emotions in people while playing sounds in Portuguese[26], this scale was also successfully used to predict playing time and preferences in games[27]. In our research, we measured valence, arousal and dominance of players after playing each game session.

There are several studies that involve the recognition of emotions and in-game player related parameters. Creating a recognition system using Support Vector Machines, researchers classified affective states from players and collecting speech signal data and an eye tracker[20]. Results showed high accuracy by applying these methods and they are being considered for improving the player interaction.

In order to predict valence, arousal and dominance, researchers focused on using random forests to prevent undesired emotions when playing videogames[18]. As a result from this study, Frommel et al.[18] proposed an architecture to react to player's emotions using procedural content generation and emotion detection.

Physiological and self-reported data, in combination with support vector machines were used to predict emotions and to keep players engaged while playing a game by adapting its difficulty automatically according to the predicted outputs[19]. Although our approach is similar to this research, there are significant differences:

- Instead of using physiological data, we focused on pressure exerted on the button of a gamepad which opens up the possibility for adding real time changes

based on behavioral patterns.

- Our approach did not only involve Support Vector Machines, we tested Neural Networks, which proved to be successful too.
- We predicted fun, frustration, boredom, valence, arousal and dominance using pressure sensitivity as input. In the previous research, these parameters were used to adapt the game difficulty.
- The accuracy of our results is higher.

Using physiological signals, it was shown that game experience can be accurately predicted[28]. A machine learning method was implemented to classify difficulty, immersion and amusement from players while playing FIFA 2016. This study involved physiological signals, facial recognition, game screen recording and in-game data.

Using flow theory and cognitive load theory to trigger engagement on players, researchers designed a new adaptive method that yielded successful results by comparing their proposal with traditional gameplay and choice-based gameplay[29),30].

Considering that previous research has demonstrated that players' behavior is not only directly related to what they experience but also can be classified and estimated, we decided to combine similar elements from previous studies and include them in our approach. We attempt to measure and understand players' emotions and game related parameters using machine learning methods.

3. Game Details

The game we designed for data collection was a 2D space shooting game with basic features. Players control a spaceship that could move throughout the screen without rotation, having the possibility to shoot straight at any time and with no constraints of ammo or time limitations. As main goal for the game, players are required to clear several waves of enemies that approach from the upper part of the screen and shot in different ways. Three lives and three bars of health are included, with the possibility to recover them using items. A sample of gameplay can be seen in **Fig. 1**. For more information about the details of design and implementation, please refer to[14].

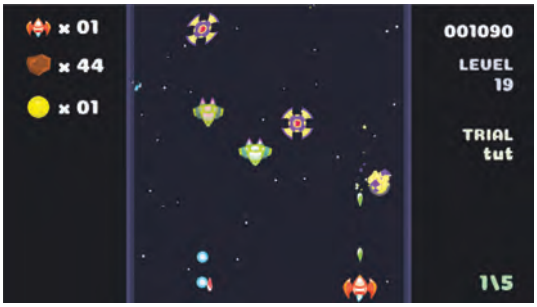

Fig. 1 A screenshot of a gameplay scene (Player: orange spaceship; Enemies: have to be destroyed by the player)

There are several reasons for choosing this type of game for our research:

- We wanted a game in which players are required to press the controller's button repeatedly in order to collect enough data for the analysis
- This type of shooting game is well-known by a wide audience
- The same type of game was used in a previous research, showing successful results[21], giving us the possibility to have a comparison referent

The level design was established using several parameters to decide what enemies and how many of them would appear in each wave. Difficulty is changed by modifying the enemies' skills and behavior.

Enemies are able to shoot from 1 to 4 bullets at the same time. In addition, enemies had different movement patterns and health, creating a more challenging and varied gameplay. Specific implementation details can be seen in our previous work[14].

4. Experiment

Experiments are designed to collect data from the pressure exerted on the button's controller. These are the parameters that we measured in the experiment: difficulty, fun, boredom, frustration, valence, arousal and dominance. **Figure 2** shows a diagram of the experiment. Threshold method was used to decide the baseline for the difficulty and 6 levels were played after that.

4.1 Structure

As illustrated by Fig. 2, the experiment is structured in two parts:

1. Threshold method: which served as a baseline to know the players' skills, letting them play until they died

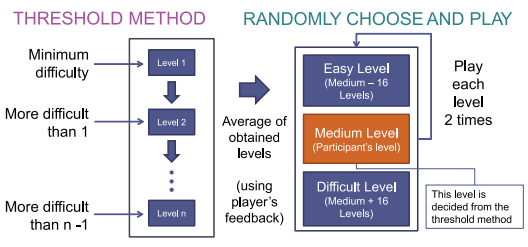

Fig. 2 Experiments layout

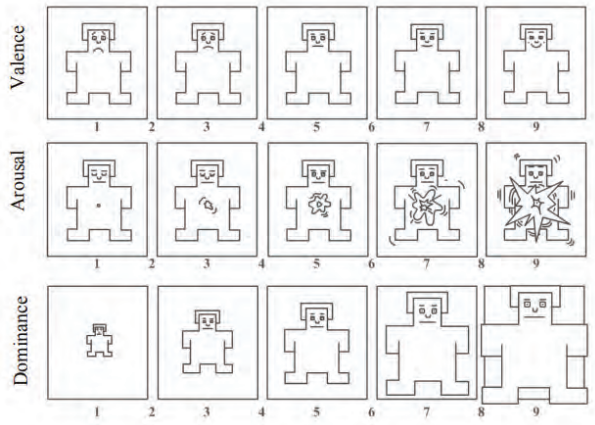

Fig. 3 Self-Assessment Manikin test

2. Randomly choose and play: which included easy (easier than the medium level), medium (last level played in the threshold method) and difficult (harder than the medium level) levels that were presented to players in a random order.

4.2 Experience questionnaire

Players were asked to fill out a questionnaire about their experience after playing one level. Questions were divided in two parts: (1) game-related questions and (2) SAM questions.

For part 1, players were questioned about: difficulty of the level, how much fun they had, how frustrated they felt and how bored they felt. All questions were designed using a Likert scale of 5 points.

The second part of the questionnaire was focused on measuring the player's feelings. For this section, we used a Self-Assessment Manikin (SAM) test, in which players were required to quantify their emotions using a predefined scale (see Fig. 3) towards the game from the experiment in three different categories: valence, arousal and dominance. Looking at the numbers from 1 to 9 and using the images as a reference, participants had to choose the value that best represented their feelings in each category.

4.3 Pressure sensitivity

Pressure exerted on the button of a PS3 controller gamepad was saved and used to create the model. Pressure is a value between 0 and 1 that indicates how hard the player presses a button in the controller. 1 means fully pressed and 0 means the button is not pressed.

Figure 4 shows the results of a sample taken from one session. The horizontal axis shows the time in seconds and vertical axis shows the pressure values recorded when pressing the shooting button.

Table 1 Number of samples per class

Cla	Dif	Fun	Fru	Bor	Val	Aro	Dom
1	38092	49921	34067	29263	53513	65464	64987
0	85394	73565	89419	94223	69973	58022	58499

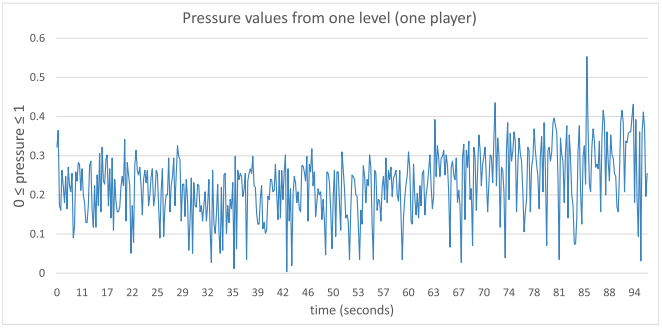

Fig. 4 Sample taken from one player after playing one level of the game

5. Machine Learning: Data Classification

One neural network and one support vector machine were created for each parameter (fun, frustration, etc.), they were trained and tested separately and independently from each other with different parameters and configuration.

5.1 General idea

Data was pre-processed before being used with the models and the output for each system was converted to the space of 0s and 1s, the general approach is represented in **figure 5**.

5.1.1 Input data

Collected data from all users (20 people) constituted a total number of 123486 samples. We used the method Leave One Out (LOO), which is a special case of cross-validation where one participant's data is used to test and the rest of the data to train the model; this process is repeated until all participants' data is used[31].

This validation model ensures that the systems can classify input data from a new user in a reliable way. We did not divide the data or the players' results by proficiency when designing and validating our models. The input length of our models was 5, we determined this value by testing with different input sizes and choosing the one with the best result.

Table 1 shows the details of each class for each parameter.

5.1.2 Pre-processing and labeling

All data was separated and labeled according to the answers given by players while doing the experiment. After completing one full session in the game, all the collected data for that specific session was classified using the given

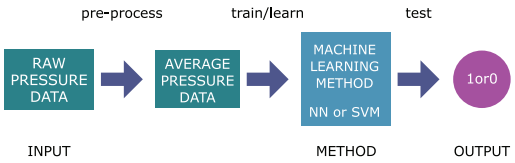

Fig. 5 General approach: Use input data in a machine learning method to predict parameters

answers, as an example, if the player rates one session as 'very difficult', all the input will be labeled as 'very difficult' for that session.

Since the pace in one level can change from easier to harder while progressing, labelling all the input values in one specific category could lead to loss of granularity about what the player is really feeling in each part of the game, this is why we decided to pre-process the data and calculate the average of each input by the time the input was stored. Using the average data of each input value, allowed us to work with the tendency of that session instead of values in a specific time.

5.1.3 Output data codification

As we mentioned in section 4.2, questions for the first four parameters were designed using a Likert scale of 5 points; the second part of the questionnaire was designed using the SAM method which consisted of 9 different answers for each parameter.

In order to use the collected data for the mentioned machine learning methods, we grouped the output vector according to three different categories: low, medium and high. Parameters that were originally codified with 5 outputs were transformed to a binary output and parameters that were originally codified as 9 outputs, were transformed to a binary output as well. That is to say that we created one specific machine for each parameter (7 parameters); for each group of that parameter (3 groups); for each method (2 methods); for a total of 42 different machines.

5.2 Implementation

All the evaluation was conducted using the free software machine learning library Scikit-learn. We conducted a series of preliminary simulations for each system and we chose the parameters with the best results, which are the results presented in this paper.

- Neural Network's Parameters:
  - Rate: Constant
  - Activation function: Relu
  - Number of hidden nodes: 100
  - Max. iterations: 1000
  - Solver: lbfgs
- Support Vector Machine's Parameters:
  - Kernel: Radial Basis Function
  - Degree: 3
  - C-Parameter: 1
  - Gamma: $\frac{1}{n}$ (being n the number of features)

5.3 Accuracy calculation

Accuracy for each model was calculated by obtaining the mean value of all accuracy results for each iteration of the LOO cross validation. Equation (1) shows the formula to calculate the overall accuracy for each model.

$$M(X,Y) = \frac{1}{n}\sum_{i=0}^{n-1} A(X_i, Y_i) \tag{1}$$

where:

- X represents a set with all the Leave One Out training data; Y is a set with all the expected outcomes for X.
- $A(X_i, Y_i)$ is the accuracy calculated for the specific set i. This function is defined in equation (2).

$$A(x,y) = \frac{1}{n}\sum_{i=0}^{n-1} f(x=y) \tag{2}$$

where:

- x represents the test data; y the expected outcome for x.
- $f(x=y)$ indicates whether x is equal to y or not.

6. Results and Discussion

Examined data was collected from 20 participants with different game skills and characteristics. 75% of the players were male and their age was ranged between 12 and 44 years old. Players with low, medium and high experience were tested.

6.1 Survey of the results

All the average results can be seen in **Figure 6**, showing all the evaluated parameters from the questionnaires in the horizontal axis, vertical axis shows the calculated accuracy.

The best result was achieved for boredom, with 83.64 % of accuracy with SVM; difficulty, fun, frustration and dominance, were predicted with around 70 % of accuracy.

In general, support vector machines performed better than neural networks for all parameters except frustration. The average accuracy (all parameters) for neural

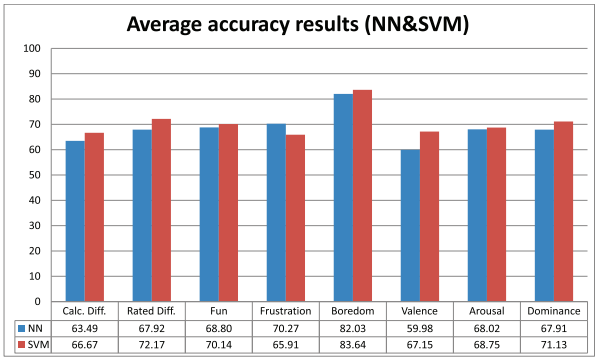

Fig. 6 Average accuracy results for Neural Networks and Support Vector Machines

networks was 68.55 % and for support vector machines was 70.69 %.

Figures 7 and **8** show the best achieved results with support vector machines and neural networks respectively. All previously explained parameters (difficulty, frustration, etc.) were tested with every output configuration explained in section 5.1.3: low, medium and high configuration, for a total of 7 parameters and 3 configurations, we tested 21 different models for each machine learning method (NN and SVM). Vertical axis shows the accuracy for each parameter and with each output configuration. The horizontal axis shows all the evaluated parameters, obtained from data collected using the questionnaires about emotions and player's perception.

From these two graphs and the calculated average result of each output configuration, we can see that recognition of the low codification model was the best (77.03 % for SVM and 75.46 % for NN), followed by the high codification model (72.17 % for SVM and 69.65 % for NN), and medium codification model yielded the worst results (62.88 % for SVM and 60.55 % for NN).

6.2 Output codification

The importance of understanding which output codification works best, gives us a hint about what would be better to use when designing a general method to predict these parameters' status. Considering that none of the evaluated methods is fully accurate in their predictions, it would be useful to understand what setup could contribute to achieve better results.

Another relevant conclusion from this specific part of the analysis is that we could use different output configurations for different parameters. For instance, calculated difficulty and frustration's models work best with a high configuration, in contrast, the rest of the parameters' models would predict better using the low configuration.

6.3 How to use these parameters

Supported by the results presented in this paper, we can estimate that the best setup for predicting game experience related parameters and emotions would be using different support vector machines as classification method. The idea is to use a specific output configuration depending on the parameter that we want to classify. One possible approach would be to choose the highest accuracy model for each parameter and use it as is; a different approach could be to combine different models to corroborate the results and use them. These estimations need further testing with new experiments and new proposals.

7. Conclusion

In this paper we presented the results of the second step for our general approach: finding patterns between pressure and players' emotions and perceptions. Data from 20 participants was analyzed through machine learning methods.

Support vector machines demonstrated to be a better method to classify this type of data according to our results, neural networks average prediction accuracy was 68.55 % and support vector machines average prediction accuracy was 70.69 %.

Despite the fact that the analysis for both research was different, our best average result is better than the one

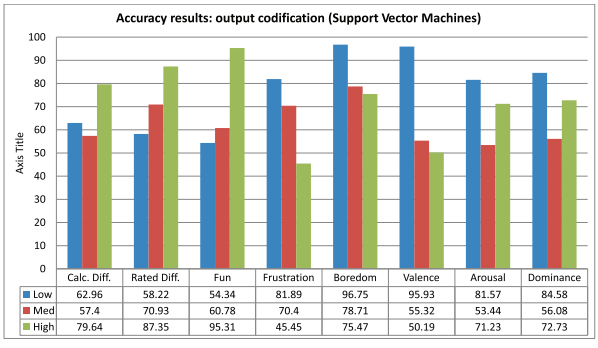

Fig. 7 Accuracy results Using Support Vector Machines

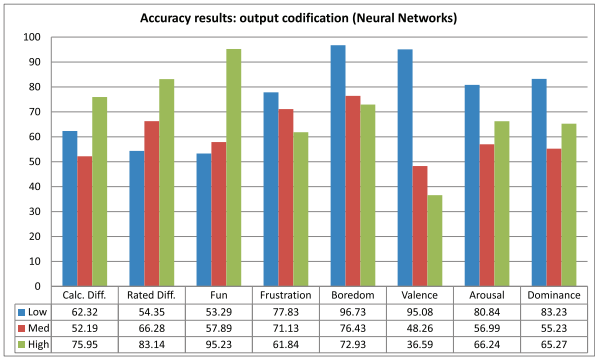

Fig. 8 Accuracy results Using Neural Networks

presented in previous research[19]. It would be meaningful to analyze the same parameters in the way that the previous research's study was conducted and compare to understand the contribution of both studies in a better way.

Results show that boredom was the parameter with the highest accuracy (83.64 %). This result can be used to include more exciting challenges or content when determining that the player is feeling bored, this could also mean that the game should stop at this point to give the player some time to relax or recover. In addition, frustration, fun, difficulty and arousal were predicted with around 70 % of accuracy.

Analyzing all the output configurations and their results, the conclusion for each configuration varies depending on each parameter. Calculated difficulty, rated difficulty and fun yielded their best results with a high output codification; the rest of the parameters yielded their best results with the low configuration. It's easier to classify the extreme configurations of each parameters.

We plan to use these results to design a new method to change the player experience according to what players feel or perceive while playing. Being able to understand the player's status opens up a range of possibilities to design more appropriate games or to have some kind of intelligent system that supports the player.

References

1) R. R. Wehbe, E. D. Mekler, M. Schaekermann, E. Lank, L. E. Nacke: "Testing Incremental Difficulty Design in Platformer Games", Proc. of the 2017 CHI Conference on Human Factors in Computing Systems, pp. 5109–5113 (2017).
2) E. Kraaijenbrink, F. Gils, Q. Cheng, R. Herk, E. Hoven: "Balancing Skills to Optimize Fun in Interactive Board Games", Proc. of 12th IFIP TC. 13 International Conference on Human-Computer Interaction (INTERACT '09), pp. 301–313 (2009).
3) J. E. Cechanowicz, C. Gutwin, S. Bateman: "Improving Player Balancing in Racing Games", Proc. of CHI PLAY 2014, pp. 47–56 (2014).
4) A. Baldwin, D. Johnson, P. A. Wyeth: "The Effect of Multiplayer Dynamic Difficulty Adjustment on the Player Experience of Video Games", CHI 2014 Extended Abstracts on Human Factors in Computing Systems, pp. 1489–1494 (2014).
5) S. Cheema, J. J. LaViola: "Wizard of Wii: Toward Understanding Player Experience in First Person Games with 3D Gestures", Proc. of the 6th International Conference on Foundations of Digital Games (FDG 2011), pp. 265–267 (2011).
6) L. Nacke, C. A. Lindley: "Flow and immersion in first-person shooters: measuring the player's gameplay experience", Proc. of the 2008 Conference on Future Play, pp. 81–88 (2008).
7) J. Dormans, S. Bakkes: "Generating Missions and Spaces for Adaptable Play Experiences", IEEE Trans. on Computational Intelligence and AI in Games, Vol. 3, No. 3, pp. 216–228 (2011).
8) A. Mourão, J. Magalhães: "Competitive Affective Gaming: Winning with a Smile", Proc. of the 21st ACM International Conference on Multimedia, pp. 83–92 (2013).
9) N. McMahon, P. Wyeth, D. Johnson: "Engaging in Videogame Play: An Activity-Centric Analysis of the Player Experience", Proc. of the Annual Meeting of the Australian Special Interest Group for Computer Human Interaction, pp. 101–108 (2015).
10) M. M. Khajah, B. D. Roads, R. V. Lindsey: "Designing Engaging Games Using Bayesian Optimization", Proc. of the 2016 CHI Conference on Human Factors in Computing Systems, pp. 5571–5582 (2016).
11) G. Chan, A. Arya, A. Whitehead: "Keeping Players Engaged in Exergames: A Personality Matchmaking Approach", Extended Abstracts of the 2018 CHI Conference on Human Factors in Computing Systems, pp. LBW064:1–LBW064:6 (2018).
12) H. Fernández, K. Mikami, K. Kondo: "Adaptable Game Experience Based on Player's Performance and EEG", 2017 Nicograph International (NicoInt 2017), pp. 1–8 (2017).
13) H. Fernández, K. Mikami, K. Kondo: "Perception of Difficulty in 2D Platformers Using Graph Grammars", International Journal of Asia Digital Art and Design Association, Vol. 22, No. 2, pp. 38–46 (2018).
14) H. Fernández, K. Mikami, K. Kondo: "Analyzing the Relationship Between Pressure Sensitivity and Player Experience", Proc. of the 16th ACM SIGGRAPH International Conference on Virtual-Reality Continuum and Its Applications in Industry, pp. 9:1–9:8 (2018).
15) K. Prasetya, Z. d. Wu: "Artificial Neural Network for Bot Detection System in MMOGs", Proc. of the 9th Annual Workshop on Network and Systems Support for Games, pp. 16:1–16:2 (2010).
16) X. Li, R. Miikkulainen: "Opponent Modeling and Exploitation in Poker Using Evolved Recurrent Neural Networks", Proc. of the Genetic and Evolutionary Computation Conference, pp. 189–196 (2018).
17) H. Yu, J. Yang, J. Han: "Classifying Large Data Sets Using SVMs with Hierarchical Clusters", Proc. of the 9th ACM SIGKDD International Conference on Knowledge Discovery and Data Mining, pp. 306–315 (2003).
18) J. Frommel, C. Schrader, M. Weber: "Towards Emotion-based Adaptive Games: Emotion Recognition Via Input and Performance Features", Proc. of the 2018 Annual Symposium on Computer-Human Interaction in Play, pp. 173–185 (2018).
19) G. Chanel, C. Rebetez, M. Bétrancourt, T. Pun: "Boredom, Engagement and Anxiety As Indicators for Adaptation to Difficulty in Games", Proc. of the 12th International Conference on Entertainment and Media in the Ubiquitous Era, pp. 13–17 (2008).
20) A. Alhargan, N. Cooke, T. Binjammaz: "Multimodal Affect Recognition in an Interactive Gaming Environment Using Eye Tracking and Speech Signals", Proc. of the 19th ACM International Conference on Multimodal Interaction, pp. 479–486 (2017).
21) J. Sykes S. Brown: "Affective Gaming: Measuring Emotion Through the Gamepad", CHI '03 Extended Abstracts on Human Factors in Computing Systems, pp. 732–733 (2003).
22) W. M. van den Hoogen, W. A. IJsselsteijn, Y. A. W. de Kort: "Effects of Sensory Immersion on Behavioural Indicators of Player Experience: Movement Synchrony and Controller Pressure", Proc. of the 2009 DiGRA International Conference: Breaking New Ground: Innovation in Games, Play, Practice and Theory (2009).
23) W. M. van den Hoogen, E. P. Braad, W. A. IJsselsteijn: "Pressure at Play: Measuring Player Approach and Avoidance Be-

haviour through the Keyboard", Proc. of the 2014 DiGRA International Conference (2014).
24) A. Canossa, A. Drachen, J. Rau, M. Sørensen: "Arrrgghh!!! -Blending Quantitative and Qualitative Methods to Detect Player Frustration", Proc. of the 6th International Conference on the Foundations of Digital Games (2011).
25) Müller, T. Fritz: "Stuck and Frustrated or in Flow and Happy: Sensing Developers' Emotions and Progress", Proc. of the 37th International Conference on Software Engineering, Vol. 1, pp. 688–699 (2015).
26) A. P. Soares, A. P. Pinheiro, A. T. P. Costa, C. S. Frade, M. Comesaña, R. Pureza: "Affective auditory stimuli: adaptation of the International Affective Digitized Sounds (IADS-2) for European Portuguese", Behavior research methods, Vol. 45, No, 4, pp. 1168–1181 (2013).
27) K. Poels, W. M. van den Hoogen, Y. A. W. de Kort, W. A. IJsselsteijn: "Pleasure to Play, Arousal to Stay : the Effect of Player Emotions on Digital Game Preferences and Playing Time", Cyberpsychology, Behavior, and Social Networking, Vol. 15, No, 1, pp. 1–6 (2012).
28) W. Yang, M. Rifqi, C. Marsala, A. Pinna: "Towards Better Understanding of Player's Game Experience", Proc. of the 2018 ACM on International Conference on Multimedia Retrieval, pp. 442–449 (2018).
29) D. Sharek E. Wiebe: "Measuring Video Game Engagement Through the Cognitive and Affective Dimensions", Simulation & Gaming, Vol. 45, pp. 565–592 (2014).
30) D. Sharek E. Wiebe: "Investigating Real-time Predictors of Engagement: Implications for Adaptive Videogames and Online Training", International Journal of Gaming and Computer-Mediated Simulations, Vol. 7, No, 1, pp. 20–37 (2015).
31) C. Sammut, G. I. Webb, Eds.: Encyclopedia of Machine Learning, pp. 600–601, Springer US (2010).

Henry FERNÁNDEZ
He obtained his PhD in Media Science at the Tokyo University of Technology, his Master's degree in Engineering from the same university and studied Computer Engineering at the Simón Bolívar University in Caracas, Venezuela. His research interests are game design, game production, programming and 2D art. He has been working as an independent game developer at Fiery Squirrel since 2014.

Koji MIKAMI
He worked at Nissho Iwai Corporation and MK Company as a producer. In 1998, he established "Creative Lab." at the Katayanagi Advanced Research Institute of Tokyo University of Technology (TUT), where research on Animation, Game and CG production technology are conducted. Currently, he is a professor at the School of Media Science, TUT. He received his Ph.D. degree at KEIO University in 2018. Now his research interests lie in game design and production technology for game and animation.

Kunio KONDO (*Fellow*)
He is a professor at the School of Media Science, Tokyo University of Technology. He received his Ph.D degree from the University of Tokyo in 1988. He was associate professor of Department of Information and Computer Sciences, Saitama University, and Technical staff of Nagoya University. He is the president of Asia Digital Art and Design Association. He was former President of The Institute of Image Electronics engineers of Japan, former President of The Society for Art and Science, and Chair of SIG on Computer Graphics and CAD of Information Processing Society of Japan.

IIEEJ Paper -- Special Issue on Extended Papers Presented in IEVC2019 --

Image Completion of 360-Degree Images by cGAN with Residual Multi-Scale Dilated Convolution

Naofumi AKIMOTO, Yoshimitsu AOKI (*Member*)

Keio University

<Summary> In this paper, we are tackling the problem of the entire 360-degree image generation process by viewing one specific aspect of it. We believe that there are two key points for achieving this 360-degree image completion: firstly, understanding the scene context; for instance, if a road is in front, the road continues on the back side; and secondly, the treatment of the area-wise information bias; for instance, the upper and lower areas are sparse due to the distortion of equirectangular projection, and the center is dense since it is less affected by it. Although the context of the whole image can be understood through using dilated convolutions in a series, such as recent conditional Generative Adversarial Networks (cGAN)-based inpainting methods, these methods cannot simultaneously deal with detailed information. Therefore, we propose a novel generator network with multi-scale dilated convolutions for the area-wise information bias on one 360-degree image and a self-attention block for improving the texture quality. Several experiments show that the proposed generator can better capture the properties of a 360-degree image and that it has the effective architecture for 360-degree image completion.

Keywords: generative adversarial networks, image completion, equirectanglur projection

1. Introduction

Equireqtanglar projection is one of the methods used for representing a 360-degree space as an omnidirectional image. Accompanied by the popularization of head-mounted displays for virtual reality (VR) and a handy 360-degree camera, there are increasing opportunities for 360-degree images like these to be used. However, there is plenty of difficulty and financial cost in designing a realistic 360-degree space with computer graphics. Therefore, as our method for easily designing a 360-degree image space, we favor the following approach: We can convert a picture with a narrow angle of view taken by a smartphone to one particular area of a 360-degree image by using internal camera parameters. Then, we can produce a whole 360-degree space by completing the remaining area with this one particular area as a necessary condition. The merit of this approach is that we can selectively use many normal camera images to determine the atmosphere of a newly generated space, since the image being generated is consistent with the conditional image. One example of the more concrete applications is that a distant view of a new VR space is easily attained. Additionally, since the completion is performed, it is possible use the same method to remove an object from the image of a 360-degree camera where an unnecessary object is easily reflected.

This paper tackles the problem of the whole 360-degree image being generated with one part as a condition, within the above whole approach to space generation. The goal of this problem setting is to reflect the specific properties of a 360-degree image in image generation. This involves two specific points: understanding the context of the scene and reflecting the differences in the amount of information in 360-degree images.

Figure 1 shows the 360-degree images and their spherical visualization using an image sample. If there is a road in front like in **Fig. 1** (a), it is better to estimate that the road continues on the back side. In the patch-based method[2], there is no path behind the image, because there is no understanding of the scene, as shown in Fig. 1 (c) and (f), but if the model understands the context of the scene, the path in the direction of the back side is predicted, as in Fig. 1 (b). An area covering 180 degrees horizontally and 90 degrees vertically that has been cut out of the 360-degree image is regarded as the front-side area, as shown in Fig. 1 (d). Convolutional Neural Network (CNN)-based Generative Adversarial Networks[1] (GANs) will predict the surrounding areas, especially corresponding to the overhead, feet, and back. This is the first step to generate a consistent result as an image representing a 360-degree space. Also, due to the influence of the equirectangular projection, the 360-degree image has a large amount of distortion, and the

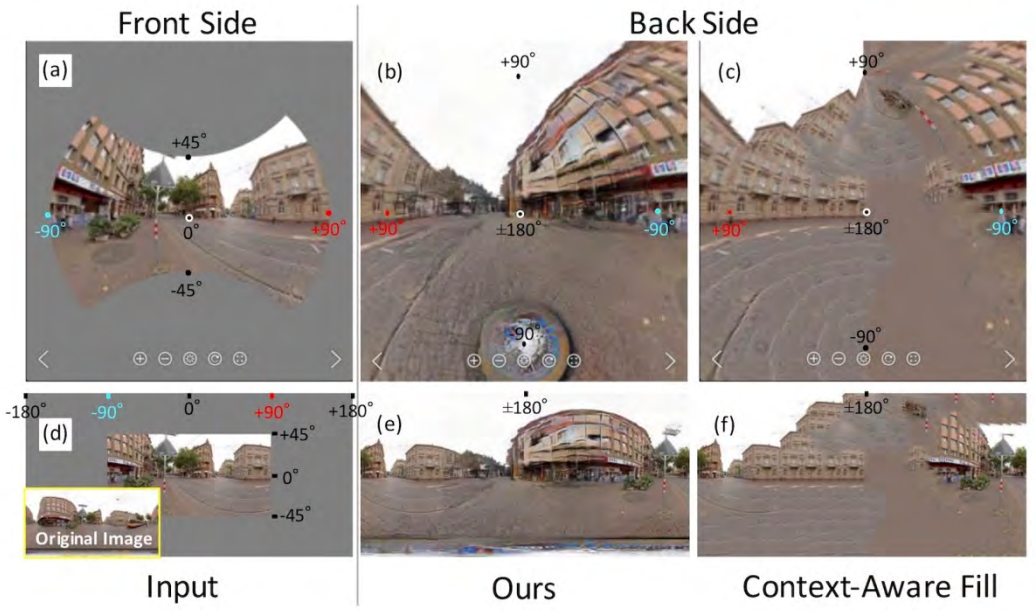

Fig. 1 360-degree images and spherical visualization

upper and lower parts of the image are continuous, with similar pixels. Therefore, the amount of information per region is sparse. However, in the central area, the information is dense, since distortion effects are lower and detailed textures are maintained. Since there is a bias in the amount of information contained by one image like above, it is necessary to make appropriate treatments.

Recently, cGAN-based methods are considered to be a promising solution to the problem of image completion (especially inpainting). Dilated convolutions[3] for expanding the CNN's receptive field are used to complete pixels based on an understanding of the context. Furthermore, they are also effective when large holes are completed. However, our problem setting differs from the conventional problem setting in that it needs to not only complete the area surrounded by the actual pixel, as in the inpainting setting, but also to complete the non-enclosed area. However, by only using dilated convolutions multiple times to expand the receptive field, it is possible to effectively deal with the sparse information but impossible to simultaneously deal with the detailed information.

Multi-scale dilated convolution, which is the architecture that concatenates outputs from series of dilated convolutions in parallel, is effective for solving the above problem. Therefore, as a generator network, we propose an encoder-decoder network with residual multi-scale dilated convolution (RMDC). Furthermore, we are introducing a self-attention block (SAB) into the last of the residual blocks to generate the detailed texture, as shown in **Fig. 2**. Experiments show that the proposed method is effective for completing 360-degree images and can generate visible plausible results. We are showing that a 360-degree space can be generated as a 2D image by displaying the result as a sphere like in Fig. 1 (a), (b), and (c).

This paper will show following outcomes: (1) Novel tackling of the 360-degree image generation and completion by GANs; (2) Performing a completion that captures the properties of 360-degree images by proposed generator, which consists of RMDC and SAB, (3) The approach to easily produce a realistic 360-degree space, which is difficult by hand design.

2. Related Work

The recent development of GANs is remarkable. There is now an unsupervised setting that comprises the generation from noises[1),4)-6)] or a conditional setting such as class condition setting[7)-9)].

Out of all conditional settings, image-to-image translation problem is considered the most promising in its practical use. There are cases where a translation model has been trained with pair data[10),11)] or unpaired data[12),13)]. One of the paired image-to-image translation problems is the problem of image completion by cGAN.

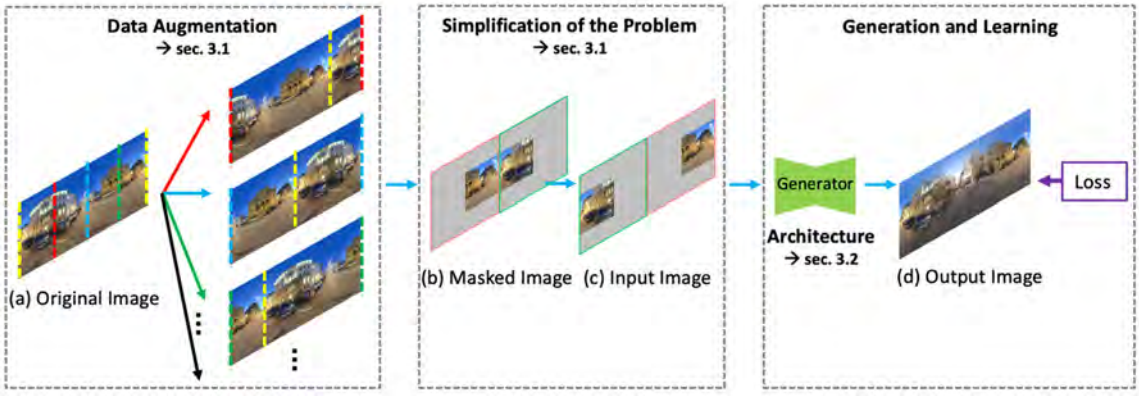

Fig. 2 Training procedure of the proposed method

In image completion or inpainting, patch-based methods[2),14),15)] are conventionally used, and recently, generation-based methods[16)-8)] using cGAN have been promising, since the methods using cGAN can help with understanding the context of an image and then generating an object that is unseen in the image. The main approach involves expanding a receptive field by using dilated convolutions in a generator. There is the method[17)], which uses a discriminator for evaluating global and local consistency in the result images, and the method[18)], which has an attention module to refer to pixels that are similar to input pixels as patch-based methods do.

The problem that we tackle is different from a conventional inpainting problem[16)-18)]. In an inpainting problem, which is an inside completion problem, the pixels being generated are enclosed by the input pixels as a condition. However, in our problem setting, the pixels being generated enclose the input pixels, so this is an outside completion problem. This problem is made more difficult due to the lack of knowledge and constraints regarding the area surrounding the pixels being generated. The existing work[19)] that tackles this problem uses a vanilla pix2pix[10)], so we believe there is still room for improvement of the network architecture according to this problem setting.

In the field of computer vision, there are many works about object recognition, segmentation, and depth estimation of a 360-degree image. Recent proposed methods[21),22)] employ distorted kernel convolution based on the 360-degree image's property of being made from a sphere. Another method[23)] of solving recognition problems involves generating a 360-degree image by selecting the patch image from the dataset with Nearest Neighbor, but there have been no studies that generated a 360-degree image with CNN-based GANs, to the best of our knowledge. Additionally, it has not been verified that distorted kernel convolutions, such as Spherical CNN[21)], are effective even in the generation process.

The problem that we are tackling is 360-degree image completion, which is the combination of 360-degree image generation and the completion of the surrounding area. Although we use dilated convolutions such as conventional cGAN-based image completion methods, we use multi-scale dilated convolutions in series and parallels to fit the properties of 360-degree images. Furthermore, we introduce a self-attention module like SAGAN[8)] to our generator in order to improve the quality of the generated texture. This attention module is different from the attention module of the above inpainting method[18)], but the expected effect is similar. In this way, by designing the generator to fit the properties of 360-degree images, our methods can generate high-quality 360-degree images that lack Spherical CNN but have a normal square convolution kernel.

3. Proposed Method

We take the cGAN approach, which has an encoder-decoder network, for 360-degree image completion. To make the problem easier, we carry out preprocessing (as shown in section 3.1) of inputs for data augmentation. Then we generate images with a newly designed generator for 360-degree image generation (as shown in section 3.2). Loss functions are the adversarial losses from a multi-scale discriminator and feature matching loss was calculated from intermediate outputs of the discriminator, and perceptual loss was calculated from a trained VGG network, which is the same as pix2pixHD[11)].

3.1 Preprocessing: image rearranging

We rearrange images as preprocessing for data augmentation in order to ease the burden of solving this problem. An original property of a 360-degree image is that

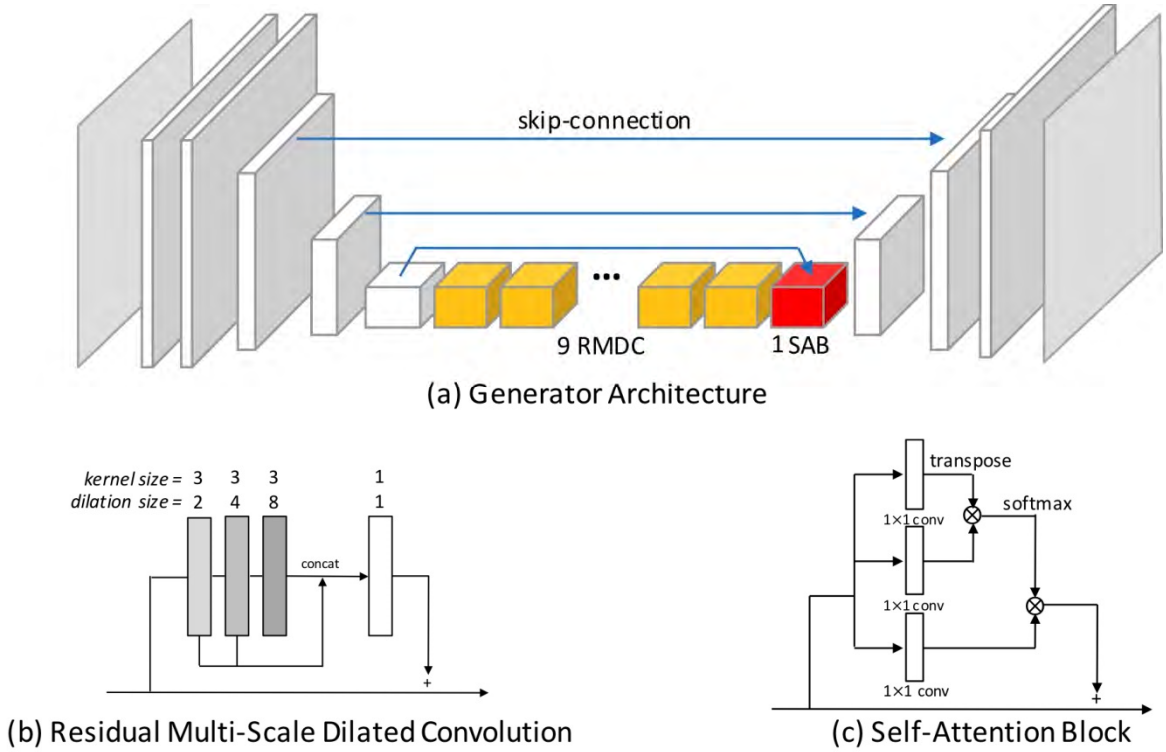

Fig. 3 Proposed generator architecture and components

both ends of the image are continuous. Therefore, a new 360-degree image whose center is changed can be generated by splitting it vertically and then swapping the pieces. By changing the position of a split line, multiple images are generated from one image. By rearranging the image, we transition from a direct problem where a generator completes the surrounding pixels of the input pixels in the center of the image, like in Fig. 2 (b), to an easier problem where input pixels are separated on both ends. When making this change, not only the center should be completed, but also the upper and lower areas, like in Fig. 2 (c), since it is easier to consider consistencies when conditional pixels enclose the generated pixels. While the generated area only considers the consistency between the center in the image before being rearranged, the generation of the center of the image can consider consistencies on both ends after being rearranged. Therefore, it become easy for the generator to predict the appropriate pixels according to their consistencies. Note that the problem after rearranging is different from conventional inpainting problems in that not only the center but also the upper and lower areas should be completed and a very large area should be generated.

3.2 Generator architecture

We propose a novel architecture of generator for capturing the features of a 360-degree image. The generator is an encoder-decoder network with skip-connection, like in **Fig. 3** (a). Its convolution architecture is the same as pix2pixHD except residual blocks on the bottleneck. The contents of the residual blocks are newly specialized for 360-degree image generation. To be more specific, the generator has Residual Multi-Scale Dilated Convolution (RMDC) and Self-Attention Block (SAB).

RMDC consists of a series and a parallel of dilated convolutions, which have gradually large-sized dilations, as shown in Fig. 3 (b). After concatenating the outputs from three dilated convolutions, the number of channels became 1/3 with a 1 × 1 convolution. The receptive fields that have been expanded by composing the dilated convolutions in a series are effective for image completion, as shown in previous works, and we think that the expanded receptive fields can capture the specific distortion of a whole 360-degree image. However, a large dilation leads to a loss of the dense texture information by automatically thinning out pixels. To address this issue, we are properly dealing with the information bias depending on the area, by using parallel dilated convolutions. The equirectangular projection, which causes the distortion of a 360-degree image, stretches the top and bottom areas in particular. Therefore, similar pixels tend to be continuous in the top and bottom areas.

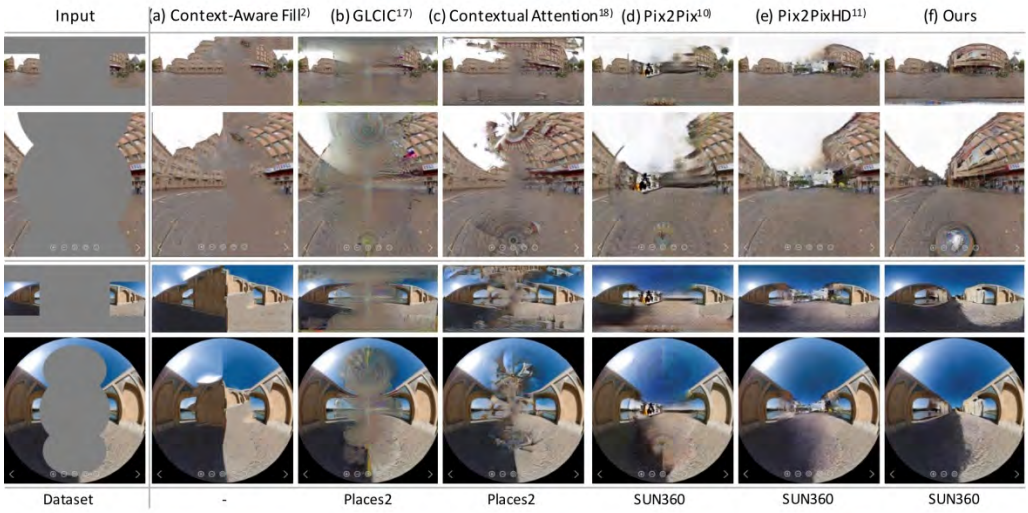

Fig. 4 Comparison results

However, fine objects tend to exist in the center, due to the decreased effects of the projection. Since a 360-degree image consists of areas of sparse and dense information, as in the above case, the adaptive scale of features should be captured with parallel convolutions. The experiments conducted to validate the effect of this RMDC are shown in section 4.3.

SAB is an attention module with architecture similar to Fig. 3 (c). This makes it possible to refer non-local features with attention map made by evaluating the correlation between pixels, which is also used in GANs[8]. To follow this step, we are also introducing SAB in order to generate fine textures. It is placed at the end of residual blocks, since the effects of referencing similar pixels from the entire feature map cannot be obtained unless the receptive field is sufficiently expanded in the previous RMDC and the input pixels at both ends are referred to in advance. See details in section 4.

4. Experiments

We used 52,800 images, including the outdoor categoryof the SUN360 dataset[23], as train data and 138 images as test data. We increased train data fourfold through data augmentation, as shown in sec. 3. The original resolution of the dataset was 9,104 × 4,552, and we resized it to 512 × 256. We used 9 RMDC and 1 SAB in the bottleneck of the generator. In training, the optimizer was Adam, whose *beta_1* was 0.5 and whose *beta_2* was 0.999. In the inference (test), only the generator is used, and the discriminator is not used. When we visualize the results as a sphere, we use the software of Ricoh Theta. We used PyTorch as deep-learning framework.

4.1 Comparison results

Figure 4 shows the comparison of the results. Fig.4 (a), (b), and (c) show the results of inpainting methods; Fig.4 (d) and (e) show the results of general image-to-image translation methods; and Fig.4(f) shows the result of proposed method. In concrete terms, Fig.4 (a) was made through context-aware fill on Adobe Photoshop; Fig.4 (b) and (c) were made through official implementation models[17),18)] trained by Places2[24)]; Fig.4 (d) and (e) were the results of the models trained by the SUN360 dataset ; Fig.4(f) was trained by the SUN360 dataset . The figures in the second and fourth rows are parts of spherical visualizations of the generated results of the first and third rows, respectively.

Inpainting models that do not use 360-degree image as their datasets cannot generate the specific distortion seen in 360-degree images. Their results are also inconsistent, likely due to their extremely large completion areas and input conditions without surrounding pixels. Additionally, pix2pix and pix2pixHD, which are thought to translate high-resolution images, generate artifacts in the center of the results. We think this is because there is a significant distance from a large generated area to the pixels that can be referenced as an input condition. Additional consideration is given in section 4.2. However, our proposed methods can generate the distortion seen in 360-degree images and fine texture, suppressing a large artifact.

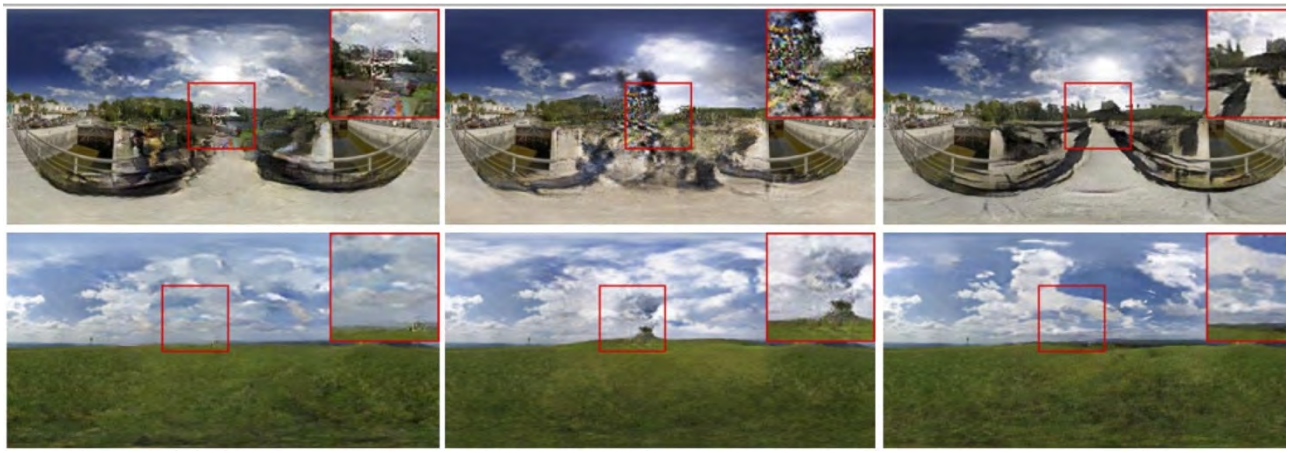

(a)RMDC (b) SAB (c)RMDC&SAB

Fig. 5 Ablation study

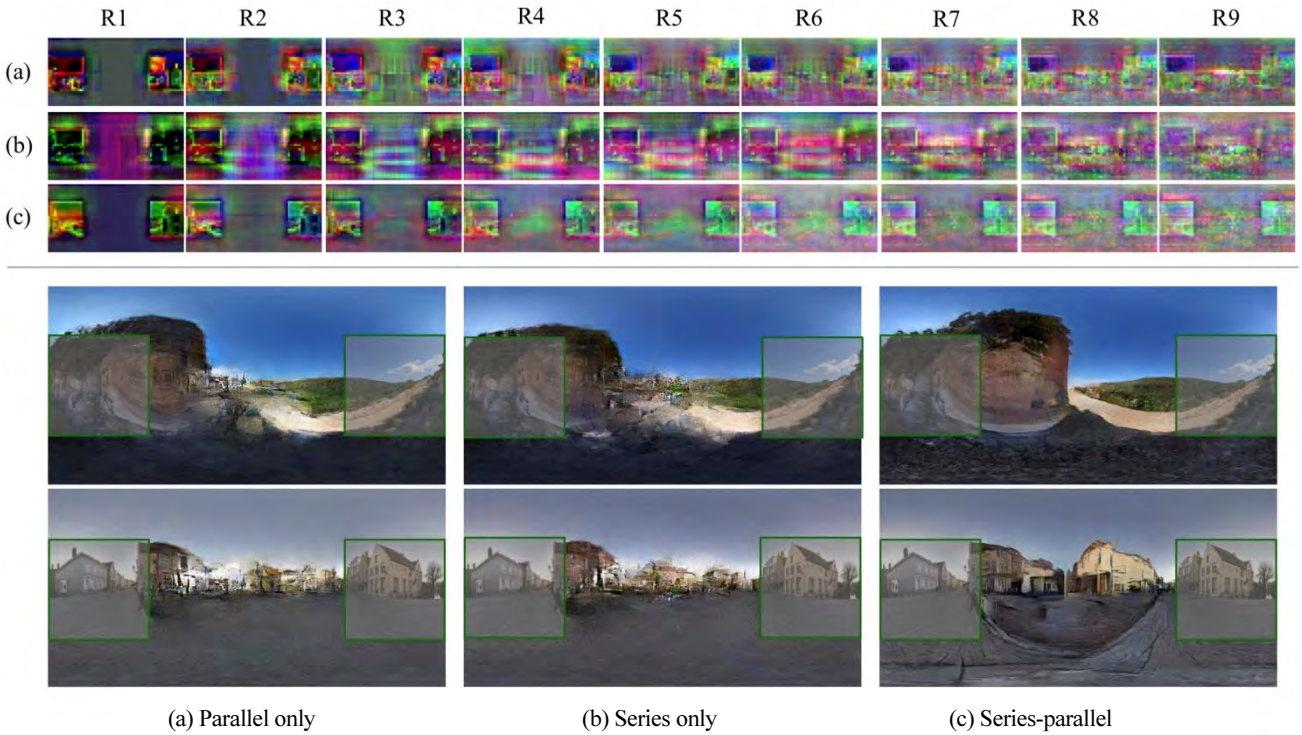

(a) Parallel only (b) Series only (c) Series-parallel

Fig. 6 Visualization of feature maps and comparison results

4.2 Ablation study

Figure 5 shows the results of ablation study for verifying the effectiveness of the components of the proposed method. In detail, Fig.5 (a) shows the results of the model when SAB is removed from the proposed method.

The results have the tendency of carrying the distortion of a 360-degree image, since it can globally understand what is seen with RMDC. However, expansion parts show that generated texture is not fine-grained but blurred.

Additionally, Fig.5 (b) uses the residual block that consists of two 3×3 convolutions, normalization, and activation such as pix2pixHD or ResNet[25], instead of RMDC. The number of the blocks is nine, as well as RMDC of the proposed method. These results show that self-attention has no effect unless the receptive field is expanded in advance, while it has the property of selecting features non-locally. Figure 5 (c) shows the results of the proposed method, which completes large holes, considering

Table 1 User study: The percentage of users judging our result to be more natural than that of the other method for the same input

Ours vs. Parallel only	Ours vs. Series only	Ours vs. Pix2PixHD
96%	98%	96%

input pixels by expanding the receptive field with RMDC and also show that the network is appropriately designed to generate fine-grained texture with SAB.

4.3 Effects of RMDC

(a) Motivation

Figure 6 shows the experimental results for revealing the effects of RMDC. Our RMDC consists of the block of convolutions of different dilation in series and parallels (see Fig. 3). However, there is also the method of using parallel-dilated convolutions, such as PSPnet[26], and series-dilated convolutions, such as the recent state-of-the-art inpainting methods[17),18)]. Therefore, we conducted the experiment so that the arrangement of dilated convolutions, as above, is changed only in the residual blocks of our method.

(b) Setting

Figure 6 shows the visualization of each of the three channels of the feature maps from each residual block and the results. Concerning the bottom part of Fig.6, (a) shows the results when dilated convolutions are in parallel. The feature maps that are output from the convolutions of each scale of dilation in parallel are concatenated, and then the number of their channel is compressed by 1×1 convolution. Note that a large dilation generates sparse features because it ignores the pixels between selected pixels. Figure 6 (b) shows the results when dilated convolutions are in series. The residual blocks have only three dilated convolutions. Figure 6 (c) shows the feature maps from each of the residual blocks of our method, and the results.

(c) Discussion

The results of R1 and R2 directly reflect the features of each structure. For the top part of Fig.6, (a)-R1 shows that the information for pixels corresponding to the inputs at both ends does not lead to the center pixels. Figure 6(a)-R2 shows that the central area is also colored, but it is uniform, so it seems that detailed information does not exist yet.

However, Figure 6 (b)-R1 shows that the information leads to the center through the effects of the receptive field expanded by series-dilated convolutions. Figure 6 (c)-R2 has more blur features than Fig. 6 (a)-R2 due to the combined effect of the dilations of various scales.

In stage R5, Fig. 6 (c)-R5 has what we intended; RMDC deals with an area-wise information bias, which is that the upper and lower areas are sparse and the center area is dense according to the projection. Meanwhile, Fig. 6 (a)-R5 does not have the shape of the whole image, while it has the detailed features. Additionally, Fig. 6 (b)-R5 has similar features throughout the whole image, although both the ends corresponding to input areas and the area corresponding to completed areas should be distinguished because of the residual learning by skip connections and residual connections.

Although all of the feature maps in R9 seem to have fine features in their centers, there are large artifacts in the actual result images. According to our observations, trying to create dense features from sparse features and trying to create global shapes from small kernels are the causes of unstable learning and artifacts.

4.4 User study

Table 1 shows the results of the user study that employs test data. Each user simultaneously saw the results of the proposed method and the comparison method and answered as to which result was more natural. We showed each 10 pairs to 5 users. We created an environment where the users could freely rotate the viewpoint using software to display the results as a sphere. The results showed that our method could generate more natural 360-degree images than other comparison methods. Moreover, users answered that they could judge by the presence and absence of an artifact. Therefore, Table 1 mainly shows whether the models can suppress artifacts relatively. **Figure 7** shows additional examples of our method's results, some of those are used for the user study. In Fig.7, regions in every result are the same position as top left, except bottom images. Bottom images are visualized by the spherical viewe input r.

4.5 Limitation

Our proposed method has some limitations. Our method can generate the texture of natural objects, such as sky or grassland, well but is not good at generating an artifact, such as buildings. Although the curves of buildings' edge are suitable for equirectangular projection, the windows are

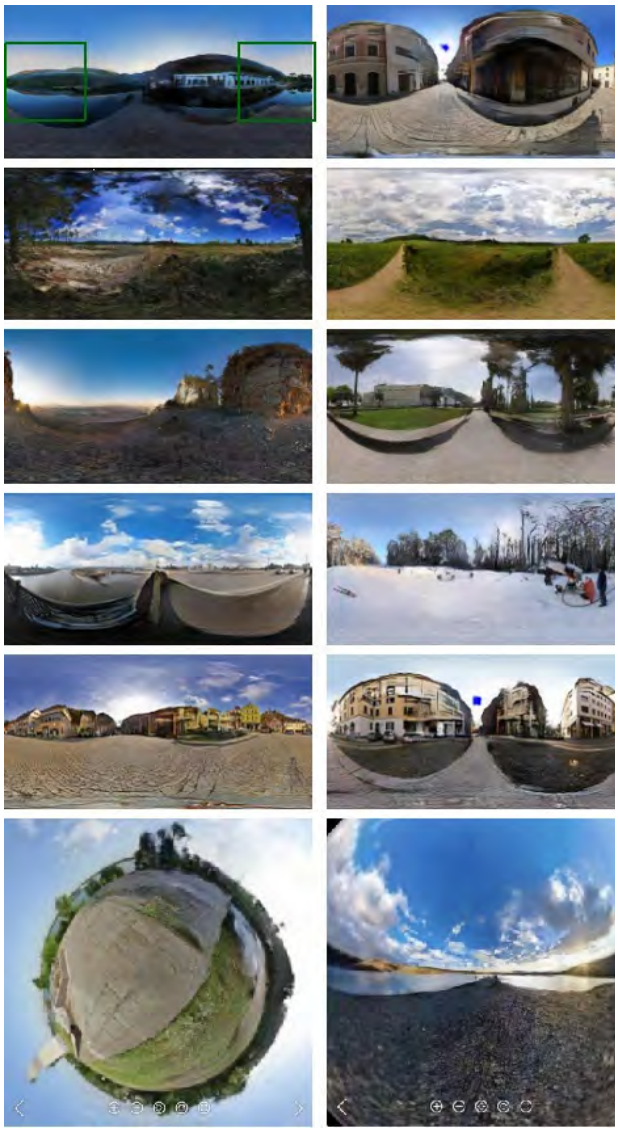

Fig. 7 Other results of our method under the same setup as Fig. 4.

distorted unnaturally. Moreover, our method cannot restore a semantic object, such as a car or a human from one part.

To summarize above, it is easier for our method to generate objects with free shapes but more difficult to generate specific shapes.

5. Conclusion

In this paper, we tackled the 360-degree image generation and completion by GANs. We proposed the novel generator with residual multi-scale dilated convolutions for dealing with the specific properties of a 360-degree image. In the user study, more than 96 percent of the results generated by the proposed method were judged to be more natural than the results of the other methods.

References

1) I. J. Goodfellow, J. P-Abadie, M. Mirza, B. Xu, D. W-Farley, S. Ozair, A. Courville, Y. Bengio: “Generative Adversarial Nets,” 27, Proc. of Advances in Neural Information Processing Systems (NIPS2014 (2014).
2) C. Barnes, E. Shechtman, A. Finkelstein, D. B. Goldman: “Patchmatch: A Randomized Correspondence Algorithm for Structural Image Editing” ACM Trans. on Graphics (TOG) (Proceedings of SIGGRAPH 2009) Vol.28, No.3 (2009).
3) F. Yu, V. Koltun: “Multi-Scale Context Aggregation by Dilated Convolutions,” arXiv:1511.07122, Proc. of International Conference on Learning Representations(ICLR2016) (2016).
4) A. Radford, L. Metz, S. Chintala: “Unsupervised Representation Learning with Deep Convolutional Generative Adversarial Networks,” arXiv:1511.06434, Proc. of International Conference on Learning Representations (ICLR2016) (2016).
5) T. Karras, T. Aila, S. Laine, J. Lehtinen: “Progressive Growing of GANs for Improved Quality, Stability, and Variation,” arXiv:1710.10196, Proc. of International Conference on Learning Representations (ICLR2018) (2018).
6) T. Karras, S. Laine, T. Aila: “A Style-Based Generator Architecture for Generative Adversarial Networks,” arXiv:1812.04948, Proc. of Computer Vision and Pattern Recognition (CVPR2019)(2019).
7) T. Miyato, T. Kataoka, M. Koyama, Y. Yoshida: “Spectral Normalization for Generative Adversarial Networks,” arXiv:1802.05957, Proc. on International Conference on Learning Representations(ICLR2018) (2018).
8) H. Zhang, I. Goodfellow, D. Metaxas, A. Odena: “Self-Attention Generative Adversarial Networks,” arXiv:1805.08318, (2018).
9) A. Brock, J. Donahue, K. Simonyan: “Large Scale GAN Training for High Fidelity Natural Image Synthesis,” arXiv:1809.11096, (2018).
10) P. Isola, J.-Y Zhu, T. Zhou, A. A. Efros: “Image-to-Image Translation with Conditional Adversarial Networks,” arXiv:1611.07004, Proc. of Computer Vision and Pattern Recognition (CVPR2017) (2017).
11) T-C. Wang, M-Y. Liu, J-Y. Zhu, A. Tao, J. Kautz, B. Catanzaro: “High-Resolution Image Synthesis and Semantic Manipulation with Conditional GANs,” arXiv:1711.11585, Computer Vision and Pattern Recognition (2018).
12) J-Y. Zhu, T. Park, P. Isola, Alexei A. Efros: “Unpaired Image-to-Image Translation using Cycle-Consistent Adversarial Networks,” arXiv:1703.10593, Proc. of International Conference on Computer Vision (ICCV2017) (2017).
13) M-Y. Liu, T. Breuel, J. Kautz: “Unsupervised Image-to-Image Translation Networks,” arXiv:1703.00848, Proc. of Advances in Neural Information Processing Systems(NIPS2017) (2017).
14) A. A. Efros, W. T. Freeman: “Image quilting for texture synthesis and transfer,” Proc. of the 28th Annual Conference on Computer Graphics

and Interactive Techniques,(SIGGRAPH'01) pp.341 – 346, (2001).

15) A. A. Efros, T. K. Leung: "Texture synthesis by non-parametric sampling," Proc. of the Seventh IEEE International Conference on Computer Vision, 1999, Vol. 2, pp. 1033 – 1038. (1999).
16) D. Pathak, P. Krahenbuhl, J.f Donahue, T. Darrell, A. A. Efros: "Context Encoders: Feature Learning by Inpainting," Computer Vision and Pattern Recognition (2016).
17) S. Iizuka, E. S-Serra, H. Ishikawa: "Globally and Locally Consistent Image Completion," ACM Trans. on Graphics Vol.36, No.4, (Proc. of SIGGRAPH) (2017).
18) J. Yu, Z. Lin, J. Yang, X. Shen, Xin Lu, T. S. Huang: "Generative Image Inpainting with Contextual Attention," Proc. of Computer Vision and Pattern Recognition 2018, pp. 5505-5514 (CVPR2018) (2018).
19) N. Kimura, J. Rekimoto: "ExtVision: Augmentation of Visual Experiences with Generation of Context Images for a Peripheral Vision Using Deep Neural Net-work," Proc. of the 2018 CHI Conference on Human Factors in Computing Systems (CHI '18) No. 427, pp. 1–10 (2018).
20) Y-C. Su, K. Grauman: "Learning Spherical Convolution for Fast Features from 360° Imagery," arXiv:1708.00919, Proc. of Advances in Neural Information Processing Systems (NIPS2017) (2017).
21) T. S. Cohen, M. Geiger, J. Koehler, M. Welling. "Spherical CNNs," arXiv:1801.10130, Proc. of International Conference on Learning Representations (2018).
22) K.Tateno, N. Navab, F. Tombari: "Distortion-Aware Convolutional Filters for Dense Prediction in Panoramic Images," Proc. of European Conference on Computer Vision (ECCV 2018) pp 732–750 (2018).
23) J. Xiao, K. A. Ehinger, A. Oliva, A. Torralba: "Recognizing scene viewpoint using panoramic place representation," Proc. of Computer Vision and Pattern Recognition (CVPR2012) (2012).
24) B. Zhou, A. Lapedriza, A. Khosla, A. Oliva, A. Torralba: "Places: A 10 million image database for scene recognition, " IEEE Trans. on Pattern Analysis and Machine Intelligence Vol.40, No.6, pp.1452–1464 (2017).
25) K. He, X. Zhang, S. Ren, J. Sun: "Deep Residual Learning for Image Recognition," arxiv:1512.03385, Computer Vision and Pattern Recognition(CVPR2016) (2016).
26) H. Zhao, J. Shi, X. Qi, X. Wang, J. Jia: "Pyramid Scene Parsing Network," Proc. of Computer Vision and Pattern Recognition (CVPR2017) (2017).

(Received April 26, 2019)
(Revised August 26, 2019)

Naofumi AKIMOTO

He received M.S from Keio University, Japan.

Yoshimitsu AOKI (*Member*)

He received the B.E, the M.E. and the Dr.E in Applied Physics all from Waseda University in 1996, 1998, 2001 respectively. He is currently a Professor at the Department of Electrical Engineering of Keio University. His research interests have been in image processing, computer vision, pattern recognition and artificial intelligent system.

IIEEJ **Paper**

Multi-Class Dictionary Design Algorithm Based on Iterative Class Update K-SVD for Image Compression

Ji WANG†, Yukihiro BANDOH††, Atsushi SHIMIZU†††, Yoshiyuki YASHIMA†(*Member*)

† Graduate School of Information and Computer Science, Chiba Institute of Technology,
†† NTT Media Intelligence Laboratories, NTT Corporation, ††† NTT TechnoCross Corporation

<**Summary**> K-SVD (K-Singular Value Decomposition) is a popular technique for learning a dictionary that offers sparse representation of the input data, and has been applied to several image coding applications. It is known that K-SVD performance is largely dependent on the features of the training images. Therefore, a multi-class dictionary approach is appropriate for natural images given the variety of their features. However, most published investigations of multi-class dictionaries are based on predetermined classification and do not consider the relation between classification stage and dictionary training stage. Therefore, there is still room for improving coding efficiency by linking dictionary training with classification optimization. In this paper, we propose a multi-class dictionary design method that repeats the following two stages: class update stage for all training vectors and dictionary update stage for each class by K-SVD. Experiments indicate that the proposed method outperforms the conventional alternatives as it achieves, for the fixed classification task, BD-bitrate scores of 6% to 48% and the BD-PSNR value of 0.4 dB to 1.6 dB.

Keywords: image coding, sparse coding, K-SVD, OMP, multi-class

1. Introduction

Image coding technology is one of the key technologies for communication services, broadcasting and many storage devices. JPEG and H.264/AVC are widely used for many currently provided image and video services. H.265/HEVC, the latest international standard, is also spreading as a coding scheme for ultra-high resolution video. Most of the conventional image coding standards adopt transforms based on discrete cosine transform (DCT). This is because DCT gives a good approximation of the Karhunen-Loeve transform (KLT) under the condition that there is high correlation among neighboring pixels, which is a known statistical property of many natural images and videos. However, DCT is not efficient enough to well represent local features of each image.

Recent research effort has been devoted to learning dictionaries that allow image coding to utilize adaptive transforms. One of the efficient methods to design such dictionaries is K-SVD (K-Singular Value Decomposition)[1]. Given an image signal, K-SVD can derive a dictionary that well approximates each block with a sparse combination of atoms from the set of blocks composing the image. An example of this approach is the facial image codec based on the K-SVD dictionary introduced by Reference 2).

It is known that dictionaries generated by K-SVD are largely dependent on the features of the training images. Therefore, the extension of K-SVD to support multiple dictionaries is a promising approach to more efficient representations of natural images with various features. Here, let us call the extended K-SVD "multi-class K-SVD". Multi-class K-SVD adaptively selects the most suitable dictionary based on the local feature(s) of the image to be encoded.

In order to design multiple dictionaries, it is necessary to classify the learning data available in terms of characteristics. Various approaches such as edge directionality and pixel value variance have been studied as local features suitable for classification. As examples for image coding application, some classification methods based on intra prediction mode and intra/inter prediction residual power of the coding unit in H.264/AVC or H.265/HEVC have been already studied[3),4)].

It has been clarified that multi-class K-SVD gives better coding performance than single class K-SVD (i.e. with one dictionary). However, conventional studies on multi-class K-SVD use predetermined classification schemes for dictionary design, and do not consider the relationship

between the classification stage and the dictionary training stage. Therefore, there still remains the potential for improvements in coding efficiency by combining dictionary training and classification optimization. In this paper, we propose a multi-class K-SVD method that takes into account the interplay between classification and dictionary design. The proposed method iterates the classification of training samples and dictionary design for each class.

The rest of this paper is organized as follows. A survey of K-SVD and conventional studies on multi-class K-SVD approaches is given in section 2. The new multi-class K-SVD algorithm with its class update cycle is proposed in section 3, and its application to image encoding and decoding is also described. Analyses of the designed dictionaries and experimental results for image coding are given in section 4 to demonstrate the effectiveness of the proposed algorithm. Finally, concluding remarks and future works are given in section 5.

2. Previous Work

2.1 Review of K-SVD

In this section, we review the dictionary learning procedure based on K-SVD[1]. The set of sample vectors for dictionary learning is indicated as the matrix $\mathbf{Y}$, and each column of $\mathbf{Y}$ corresponds to N sample vectors $\mathbf{y}_i (i = 1, 2, \cdots, N)$. For image representation, $\mathbf{y}_i$ is often set as a vector whose elements are the pixel values in the i-th small block obtained after dividing the image. Let $\mathbf{d}_k (k = 1, 2, \cdots, K)$ be the k-th atom vector, and let dictionary $\mathbf{D}$ be a matrix in which these atoms are arranged as columns. The dimension of these atoms equals that of $\mathbf{y}_i$. We represent signal $\mathbf{y}_i$ as a linear combination of these atoms as expressed by Eq. (1).

$$\mathbf{y}_i = \sum_{k=1}^{K} x_{ik}\mathbf{d}_k \tag{1}$$

x_{ik}, which denotes the k-th element of vector $\mathbf{x}_i$, is the representation coefficient of the sample $\mathbf{y}_i$. Using coefficient matrix $\mathbf{X} = (\mathbf{x}_1, \mathbf{x}_2, \cdots, \mathbf{x}_N)$, Eq. (1) can be written as

$$\mathbf{Y} \approx \mathbf{DX} \quad . \tag{2}$$

We consider an optimization problem with sparsity constraints that expresses input vector $\mathbf{y}_i$ with as few atoms as possible. Approximations with greater sparsity and smaller error can generally be obtained by using a dictionary learned from samples having characteristics similar to the samples to be represented. Therefore, it is desirable to co-optimize both dictionary $\mathbf{D}$ and coefficient $\mathbf{X}$. This problem can be formulated as

$$\min_{\mathbf{D},\mathbf{X}} ||\mathbf{Y} - \mathbf{DX}||_F^2 \quad \text{subject to} \quad \forall i, ||\mathbf{x}_i||_0 \leq T_0 \ . \tag{3}$$

Here, notation $\|\cdot\|_F$ stands for the Frobenius norm , $\|\mathbf{x}_i\|_0$ means the number of non-zero elements in the vector $\mathbf{x}_i$, and T_0 is the sparsity constraint threshold.

K-SVD solves Eq.(3) by iterating two stages, sparse coding stage and dictionary update stage. The former applies orthogonal matching pursuit (OMP)[5] to determine $\mathbf{x}_i$ for each $\mathbf{y}_i$ while fixing $\mathbf{D}$; and the latter updates $\mathbf{D}$ together with the nonzero coefficients of $\mathbf{x}_i$. The algorithmic description of K-SVD is detailed in Reference 1).

2.2 Feature specific multiple dictionaries

When an image is expressed under the condition that the number of non-zero coefficient is T_0 or less, the dictionary designed by K-SVD under the constraint that the number of non-zero coefficients is less than T_0 using that image can minimize reconstruction errors. However, the characteristics of K-SVD derived dictionaries are highly dependent on the feature of the images used in training. A dictionary trained for a specific image is optimum for that image, but not necessarily for other images. **Figure 1** shows the dictionaries $\mathrm{D}_{\mathrm{barbara}}$, $\mathrm{D}_{\mathrm{lena}}$ and $\mathrm{D}_{\mathrm{pepper}}$ designed by K-SVD under the constraint condition of $T_0 = 3$ for each of the three images "Barbara", "Lena" and "Pepper". The atoms included in each dictionary reflect the characteristics of the image used for training. For example, in the Barbara image, stripe patterns having various directions present in the original image strongly appear as several atoms in the dictionary. To measure the sparse representation performance of these dictionaries, the Peak Signal to Noise Ratio (PSNR) values of the images reconstructed by applying the three dictionaries $\mathrm{D}_{\mathrm{barbara}}$, $\mathrm{D}_{\mathrm{lena}}$, and $\mathrm{D}_{\mathrm{pepper}}$ to each image, "Barbara", "Lena", and "Pepper" are shown in **Table 1**. Table 1 shows the results under the same sparsity condition of $T_0 = 3$. The quantization and entropy coding for coefficients are not applied because they affect the evaluation of sparse representation performance itself. Therefore, note that the PSNR in Table 1 indi-

Table 1 PSNR values of the images reconstructed by the different dictionaries

	$\mathrm{D}_{\mathrm{Barbara}}$	$\mathrm{D}_{\mathrm{Lena}}$	$\mathrm{D}_{\mathrm{Peppers}}$	$\mathrm{D}_{\mathrm{HEVC\text{-}DCT}}$
Barbara	**29.59**	25.53	25.08	26.20
Lena	31.70	**32.95**	32.27	29.51
Peppers	31.70	32.31	**32.94**	29.67

cates the sparse representation performance, not coding performance. That is, first, three non-zero coefficients are obtained by repeating the projection (OMP) of the target block vector in the image onto the basis in each dictionary three times. After that, the target image is reconstructed using only those three coefficients, and how much it can approximate the original image was measured. For comparison, the result when each image is reconstructed using the HEVC-DCT[6]dictionary under the same sparsity condition of $T_0 = 3$ is also shown. For all images, image reconstruction performance is highest with the dictionary trained against itself. Unfortunately, using a dictionary trained against different images seriously degrades image reconstruction performance. For example, for the Barbara image, the other two K-SVD dictionaries yield worse performance than HEVC-DCT. When applying K-SVD to image coding, the decoder has to use the same dictionary as the encoder, so the designed dictionary itself must be encoded and transmitted to the decoder. However, the coding and transmission of atoms for each image every time incurs large overheads for information transmission, and is not practical from the viewpoint of rate distortion performance.

To solve this problem, some researchers take approaches that share the multiple dictionaries among an encoder and a decoder in advance. That is, first, the image is divided into small blocks to calculate local features, then a set of blocks having similar features is created as a class, and finally, K-SVD is executed for each class so as to create multiple dictionaries. It is considered that the local features in images can be classified into similar geometric patterns such as the direction of edges and texture features. A set of dictionaries designed for each class is shared in advance by the encoder and decoder, and these are adaptively switched when encoding. This eliminates the need to encode new sets of dictionary information, and makes it possible to represent more images efficiently. For example, in Reference 3), based on the H.265/HEVC framework, an approach is proposed in which training samples are classified by transform unit (TU) size and a dictionary is designed by K-SVD for each class. Moreover, it is described that an application-specific dictionary can be developed for particular applications such as gaming or medical video by changing samples in training. Further, in Reference 4), block classification based on intraframe/interframe prediction residual power is performed using the H.264/AVC framework, and different dictionaries are designed class by class. For

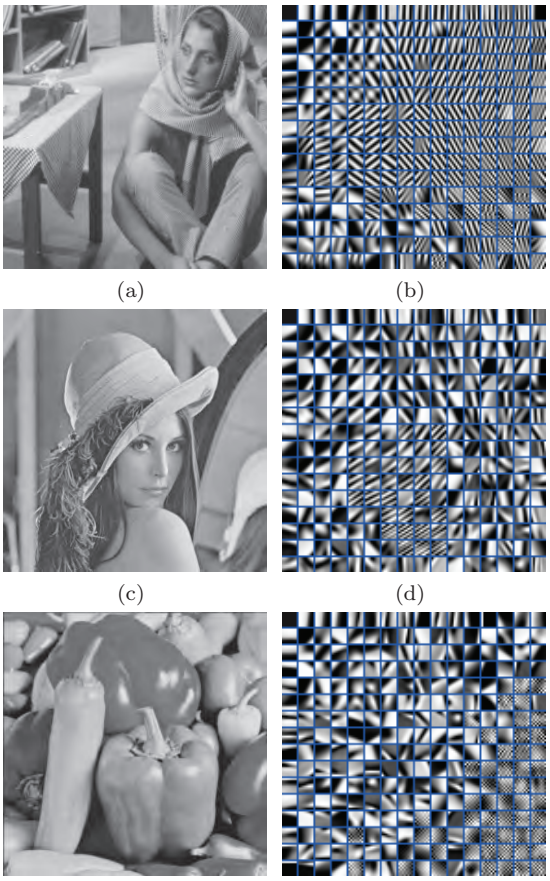

Fig. 1 Dictionaries designed by K-SVD; the original images ((a), (c), (e)) and their corresponding dictionaries ((b), (d), (f))

application other than image coding, multiple dictionaries designs based on K-SVD also have been studied. In reference 7), multiple dictionaries are designed in order to sharpen the character image. Small patches in images are classified into 13 classes based on their pixel distribution state, and a K-SVD dictionary is designed for each class. In Reference 8), the effectiveness of class specific sparse codes is investigated in the context of discriminative action classification. The local motion features for each action are trained by K-SVD to design the action specific dictionary. In References 3),4),7) and 8), local regions of an image are classified into multiple classes according to their characteristics, and a dictionary setting based on K-SVD is performed class by class. However, conventional methods do not consider the effects of classification on the subsequent processes, a dictionary learning based on K-SVD, because these methods use pre-determined features in performing classification. This is, the classifications and dictionary learning are designed independently. This raises the disadvantage that image representation performance depends on what kinds of features are used for classification.

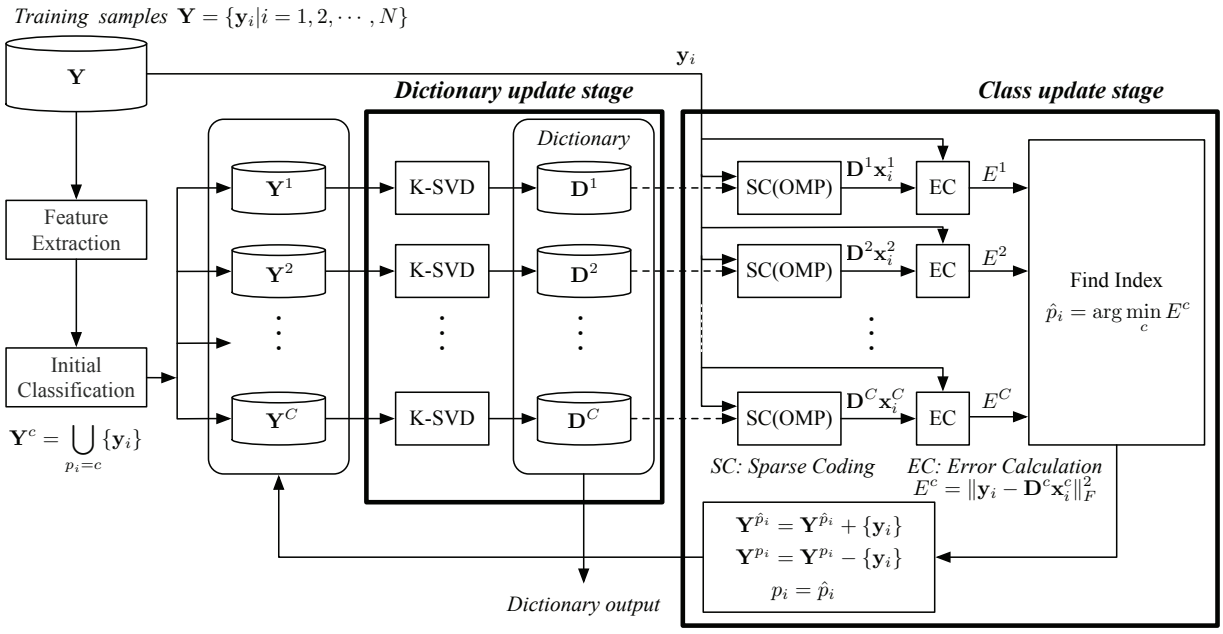

Fig. 2 Block diagram of dictionary training by Multi-class K-SVD

For example that considers the effect of classification on dictionary learning based on K-SVD, there are some studies on image clustering. In References 9) and 10), a dictionary for face recognition and object recognition are designed by K-SVD. They improved the performance of class identification by adding not only the approximation error for the training data but also the identification error based on the linear classifier to the cost function of the K-SVD algorithm. The dictionary designed by the methods in References 9) and 10) is a "single" dictionary for better class classification and does not correspond to the multi-class dictionary design handled in this paper. In Reference 11), the design method of class specific dictionary for clustering is proposed. The dictionaries, coefficients, and the parameters of support vector machine (SVM) are designed based on an alternating optimal approach for the training data. The purpose in Reference 11) is not a dictionary design for image compression, but a dictionary design for image classification. For this reason, the correct class label information is added to the training data used for dictionary design as supervised data. Therefore, the method proposed in Reference 11) cannot support unsupervised learning. Furthermore, since each atom is not occupied by a specific class dictionary but is shared among the dictionaries of multiple classes, the designed dictionaries are not completely independent for each class.

In contrast to the conventional research described above, the contribution of this paper is to propose a multi-class dictionary design method targeting image coding, and to clarify the effect of the proposed method. In order to focus on application to image coding, its classification takes an unsupervised approach based on the k-means method, unlike the conventional supervised technique for such as object recognition and image classification. In the proposed method, a multi-class dictionary is designed by repeating the two stages, unsupervised class update stage for all training vectors and dictionary update stage for each class by K-SVD. Compared to conventional approaches that do not perform classification optimization, better compression efficiency is expected.

3. Proposed Method

In this section, we propose a new multi-class dictionary design method consisting of two stages (dictionary design and classification), and its application for image coding. For designing multi-class dictionaries, we iterate the classification of training data and the dictionary design process for each class. By performing iterative convergence processing, we can create multi-class dictionaries that solve the conventional problem of what kind of local features should be used for clustering. In the proposed method in this paper, dictionary design including classification of training data is performed as unsupervised learning. Therefore, our method includes a different process from the conventional dictionary design method based on iterative updating using supervised data. In this section, we show the detail algorithm to design the multiple dictionaries based on K-SVD under unsupervised training and how to apply multi-class dictionaries ob-

Algorithm 1 The multi-class K-SVD algorithm

Initialization:
Set the number of classes C. Set the maximum number of iterations for class update L_{max}. Set over-complete DCT to initial $\mathbf{D}^c$ for each class. Classify all training vectors $\mathbf{y}_i (i = 1, 2, \ldots, N)$ into classes based on DSIFT, $\mathbf{Y}^c = \bigcup_{p_i=c} \{\mathbf{y}_i\}$ and set class index for $\mathbf{y}_i$ to p_i. Set $count = 0$.

Dictionary update stage:
for $c = 1, 2, \cdots, C$ **do**
Calculate dictionary $\mathbf{D}^c$ with K-SVD.
end for

Class update stage:
for $i = 1, 2, \cdots, N$ **do**
for $c = 1, 2, \cdots, C$ **do**
find $\mathbf{x}_i^c$ that approximates $\mathbf{y}_i$ by sparse coding with $\mathbf{D}^c$
end for
new class index $\hat{p}_i = \arg\min_c \|\mathbf{y}_i - \mathbf{D}^c \mathbf{x}_i^c\|_F^2$
if $\hat{p}_i \neq p_i$ **then**
$\mathbf{Y}^{\hat{p}_i} = \mathbf{Y}^{\hat{p}_i} + \{\mathbf{y}_i\}$
$\mathbf{Y}^{p_i} = \mathbf{Y}^{p_i} - \{\mathbf{y}_i\}$
$p_i = \hat{p}_i$
end if
end for
Set $count = count + 1$

Convergence check:
if $count > L_{max}$ or no class index is changed **then**
return Dictionary $\mathbf{D}^c (c = 1, 2, \ldots, C)$.
else
Back to "Dictionary update stage".
end if

tained by the proposed method to image compression.

3.1 Dictionary training process

Figure 2 depicts the process flow of the proposed multi-class K-SVD dictionary design method. Since dictionary design and classification cannot be optimized at the same time, the proposal alternately performs, for each class, the classification of training data and dictionary design. **Algorithm 1** details the steps of the multi-class dictionary design; the specific procedures in each stage are described as follows.

First, training images are divided into small blocks, and training vectors are calculated to yield a set of m-dimensional vectors $\mathbf{y}_i (i = 1, 2, \ldots, N)$ where elements of $\mathbf{y}_i$ are pixel values in the i-th block. N is the number of training vectors. We consider that each training vector, $\mathbf{y}_i$, can be approximated as a weighted linear combination of the atoms in dictionary $\mathbf{D}^c$, where the weight coefficients of the atoms are denoted as coefficient vector $\mathbf{x}_i$. Training vectors are initially classified into C classes, $\mathbf{Y}^1, \mathbf{Y}^2, \cdots, \mathbf{Y}^C$, based on their local features and class index for $\mathbf{y}_i$ is determined as p_i, where $p_i \in \{1, 2, 3 \ldots C\}$. As the local feature, dense scale invariant feature transform (DSIFT)[12]is utilized because the distribution of edge gradient direction in a block can be expected to significantly influence the shape of basis patches to be designed. The initial dictionary for each class is set to over-complete DCT with size K.

Next, in the dictionary update stage, a dictionary that enables sparse representation for training vectors for each class is designed. In preparation, we concatenate all training vectors $\mathbf{y}_i$ that belong to class c as columns of matrix $\mathbf{Y}^c \in \mathbf{R}^{m \times n(c)}$ and similarly concatenate coefficient vectors $\mathbf{x}_i$ for $\mathbf{y}_i$ to build matrix $\mathbf{X}^c \in \mathbf{R}^{K \times n(c)}$. Here, $n(c)$ is the number of training vectors belonging to the c-th class. Dictionary $\mathbf{D}^c$ and coefficient $\mathbf{X}^c$ are obtained by solving Eq. (4).

$$\min_{\mathbf{X}^c, \mathbf{D}^c} \|\mathbf{Y}^c - \mathbf{D}^c \mathbf{X}^c\|_F^2, \text{ s.t. } \forall_i, \ \|\mathbf{x}_i^c\|_0 \leq T_0 \tag{4}$$

As the solver of the problem in Eq. (4), we use K-SVD. Specifically, as shown in Eq. (4), dictionary $\mathbf{D}^c \in \mathbf{R}^{m \times K}$ and coefficients $\mathbf{X}^c$ that minimize the square error between original signal $\mathbf{Y}^c$ and its reconstructed signal $\mathbf{D}^c \mathbf{X}^c$ are found under the sparsity constraint that the number of nonzero coefficients in each column of matrix $\mathbf{X}^c$ is equal to or less than T_0. This designs C dictionaries.

After dictionary design, the class update stage is executed. Among the C kinds of dictionaries $\mathbf{D}^c$, a new class index $\hat{p}_i$ for each training vector $\mathbf{y}_i$ is re-assigned so as to satisfy the following:

$$\begin{aligned} \hat{p}_i = \quad & \arg\min_c \|\mathbf{y}_i - \mathbf{D}^c \mathbf{x}_i^c\|_F^2 \\ & \text{s.t. } \|\mathbf{x}_i^c\|_0 \leq T_0, \ i = 1, 2, \cdots, N. \end{aligned} \tag{5}$$

The above equation yields the class index that minimizes the square error between a training vector and its reconstructed vector from the designed dictionary subject to the constraint on the number of nonzero coefficients. If $\hat{p}_i$ is different from p_i, the training sample $\mathbf{y}_i$ is moved to class $\mathbf{Y}^{\hat{p}_i}$ and the class index p_i of $\mathbf{y}_i$ is replaced by $\hat{p}_i$.

These two steps, the dictionary update stage for each class by K-SVD and the class update stage, are iterated until the convergence conditions are satisfied. The convergence conditions are that the number of iterations exceeds predetermined threshold L_{max} or that none of the class indices of the training vectors change. Finally, the algorithm outputs $\mathbf{D}^c (c = 1, 2, \cdots, C)$ as the multi-class dictionaries.

In order to effectively represent the actual image, each dictionary to be designed should contain one DC basis, as has been confirmed [1)13)]. Therefore, one DC basis is included in the initial dictionary for each class, and the DC basis is not changed during iterative processing. Also,

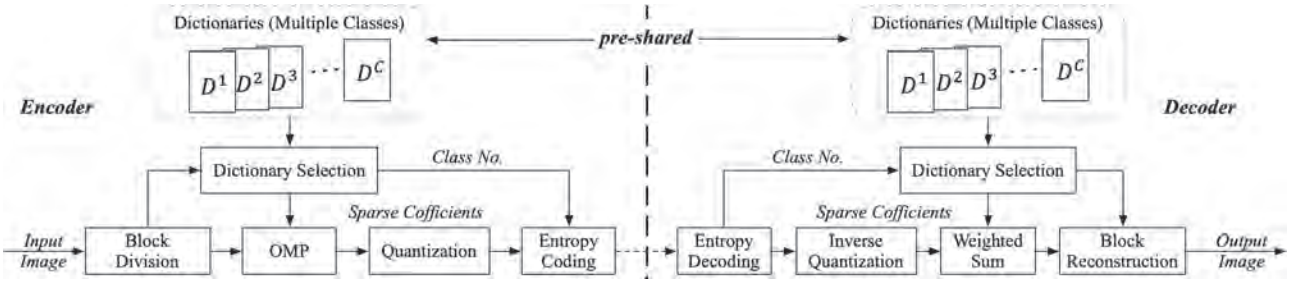

Fig. 3 Block diagram of encoder and decoder with multi-class dictionaries

atoms other than DC maintain zero mean during iterative processing.

3.2 Encoding/decoding process

This section describes the encoding and decoding process using dictionaries designed by the proposed multi-class K-SVD algorithm. A block diagram of the encoder and decoder is shown in **Fig. 3**. All dictionaries $\mathbf{D}^c(c = 1, 2, \cdots, C)$ are designed offline, and prestored in both encoder and decoder. Here, all atoms other than DC in the dictionary are normalized so that the mean value is zero and the standard deviation is one.

In the encoding process, an image to be coded is divided into small blocks of the same size as the used in the training process. Then, OMP is performed for each target block $\mathbf{t}_i$ under sparsity condition T_0; the squared errors $\mathbf{e}^c(c = 1, 2, \cdots, C)$ are calculated as follows,

$$e^c = \|\mathbf{t}_i - \mathbf{D}^c\mathbf{x}_i\|_F^2 \quad , \tag{6}$$

then the class index c and sparse coefficients $\mathbf{x}_i$ that minimize squared error e^c are determined. Quantized coefficients $Q(\mathbf{x}_i)$ and class index c are encoded and transmitted.

When sparse coding is applied to image compression, how to assign codes to sparse coefficients is an important point. Due to the nature of sparse coding, most of the coefficients for representing image data are zero; at most T_0 coefficients are non-zero. In order to reconstruct an image from sparse coefficients, it is necessary to efficiently encode the index of each nonzero coefficient, which indicates the basis corresponding to the nonzero coefficient, based on its statistical properties. Previous studies have shown that the index at which nonzero coefficients occur is uniformly random, and the distribution of the quantization level of nonzero coefficients can be approximated by a Laplacian function[3]. In Reference 3), based on this characteristic, indices of the nonzero coefficients are represented by a fixed length code and the quantized level of the nonzero coefficients is represented by a Golomb-Rice code. To express the indices of nonzero coefficients more efficiently, a method of assigning a variable length code to a zero run length (i.e. the number of consecutive zero coefficients between nonzero coefficients) has been proposed [14]. The entropy coding in this paper follows the method of Reference 14). That is, for each block, the number of quantized nonzero coefficients (NUM), the zero run length between nonzero coefficients (ZR), and the level number of the quantized nonzero coefficients (LEVEL) are separately encoded and transmitted. Since the DC coefficient of a block is highly correlated with that of its prior block, we adopt differential pulse code modulation (DPCM) when coding DC coefficients.

Furthermore, in the proposed method, it is necessary to encode the class index in order to identify the dictionary used for sparse coding. According to our experiments, there was no clear correlation between the class index of a target block and the class index of its neighboring blocks. Moreover, we failed any indication of the occurrence probability distribution of the class index concentrating on a specific class. Therefore, class indices are represented using $\lceil \log_2 C \rceil$ bit fixed length codes. The details are shown in section 4.5.

In the decoding process, the dictionary is adaptively selected block by block based on the decoded class index, and pixel values in the block are reconstructed as the sum of atoms weighted by the decoded sparse coefficients. Since the weighted sum is only calculated for the inverse transformation, the computation cost in the decoder is as low as a normal DCT.

4. Experimental Results

4.1 Simulation conditions

We evaluate the effectiveness of the proposed method using the ITE test image data set[15),16)]and HEVC test sequence[6]. The experimental conditions are summarized in **Table 2**. Thirty-one images with a resolution of 1080p are used as training data for dictionary design, and six

Table 2 Experimental conditions

Dictionary training	Block size	8×8
	Initial dictionary	Over-complete DCT with 16×16 atoms
	Number of classes C	32, 64, 128
	Sparsity parameter T_0 Initial classifier	3, 5, 7, 9 k-means using DSIFT[12)]
	Maximum iteration limit for class update, L_{max}	20
Encoding	Coefficients quantization	Uniform quantization for step QP (for DC, QP=1)
	Coefficients coding (DC)	DPCM using the previous block's DC coefficient
	Coefficients coding (AC)	Separately encoding of NUM, ZR, and LEVEL
	Class index	Fixed length coding

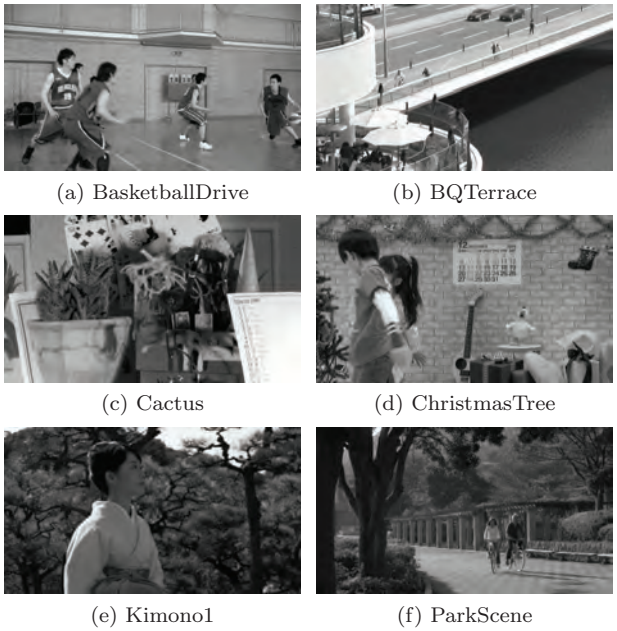

(a) BasketballDrive (b) BQTerrace

(c) Cactus (d) ChristmasTree

(e) Kimono1 (f) ParkScene

Fig. 4 Test images

images in **Fig. 4**, not included in the training images, are used as encoding targets.

In this experiment, in order to analyze the behavior of the proposed method in detail, multi-class dictionaries are designed using various parameters. Specifically, we prepared dictionaries by setting the class index C to $32, 64, 128$ and the sparsity parameter T_0 to $3, 5, 7, 9$. Each basis included in the dictionary is set to 8×8 size, following JPEG. Dictionary training based on multi-class K-SVD is started for each class by setting overcomplete DCT with $16 \times 16 = 256$ atoms as an initial dictionary. For the initial classification, the DSIFT feature obtained for each block is used, and the maximum number of iterations of class update is set to 20.

Next, experimental conditions of encoding are as follows. The coding experiment examined intraframe coding, and performance is evaluated from the viewpoint of the PSNR of the decoded image and the amount of information transferred. After the image to be coded is divided into 8×8 blocks, sparse coding using a multi-class dictionary is performed for each block according to the method described in section 3.2, and a class index for specifying the dictionary to be used and the coefficients corresponding to each basis are obtained. As described in section 3.2, DC coefficients of two neighboring blocks are strongly correlated, so the difference from the decoded DC coefficient of the previous block is quantized and encoded. Since the DC coefficient greatly influences visual image quality, the quantization step for the DC coefficient difference is set to just one. The amount of information for DC coefficients is calculated as the entropy of the quantization level number corresponding to the quantized prediction error. AC coefficients (coefficients for atoms other than DC) are linearly quantized with quantization width QP. The quantization level number "LEVEL" for coefficient x is calculated as

$$\mathrm{LEVEL} = sign(x) \times \lfloor (|x| + QP/2)/QP \rfloor \quad . \qquad (7)$$

The amount of information for AC coefficients is calculated as the entropy obtained from the occurrence probability NUM, ZR and LEVEL. Fixed length code of $\lceil \log_2 C \rceil$ is allocated to each class index. The total amount of information required for each block is calculated as the sum of the amount of information occupied by DC coefficient, AC coefficients, and class index.

4.2 Dictionary training performance

Figure 5 shows the percentage of training samples whose class indices changed among the training samples with each class update iteration. Clearly, the change in the number of training samples belonging to each class gradually converges to zero with class update iteration regardless of the number of classes, C, or the sparsity parameter, T_0.

In addition, **Fig. 6** shows the mean square error (MSE) between the original block and the block reconstructed by the dictionary designed after each iteration number. In this determination, coefficient quantization was not performed. From Fig. 6, we find that MSE strongly decreases in the first few iterations, continues to gradually decrease subsequent class update iterations, and converges to a ba-

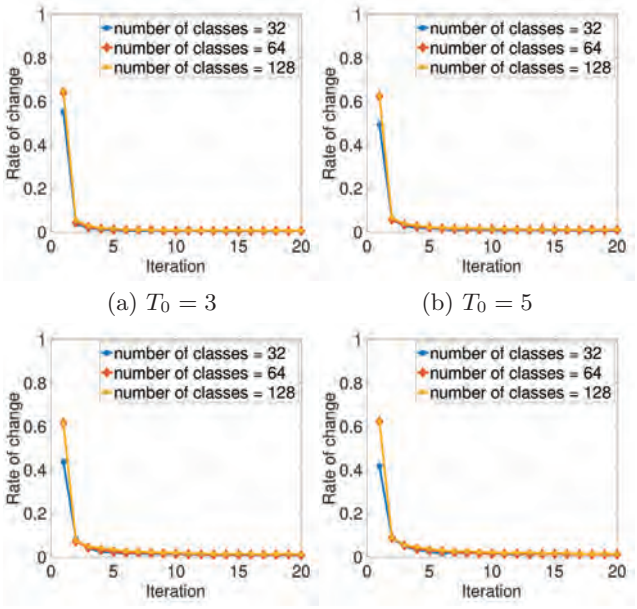

(a) $T_0 = 3$ (b) $T_0 = 5$

(c) $T_0 = 7$ (d) $T_0 = 9$

Fig. 5 The rate of change in the number of training samples belonging to each class

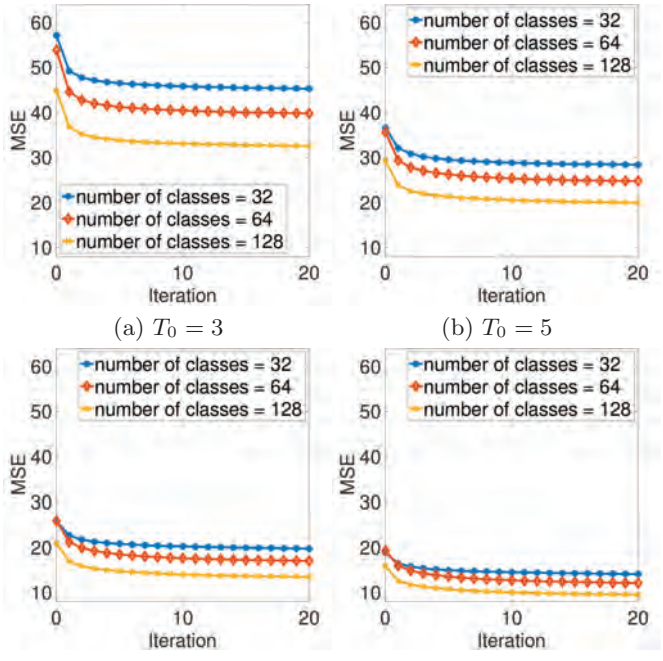

(a) $T_0 = 3$ (b) $T_0 = 5$

(c) $T_0 = 7$ (d) $T_0 = 9$

Fig. 6 MSE convergence characteristics for the training data

sically constant value in 15 to 20 iterations regardless of C or T_0. Furthermore, the converged value of MSE apparently decreases as class number C increases and as sparsity parameter T_0 increases. This is because the atoms that offer better approximation of the local pixel value distribution are easier to find in the designed dictionaries as C and/or T_0 increase. Based on the above results, the following experiments were carried out by setting the maximum iteration number for class update, L_{max}, to 20.

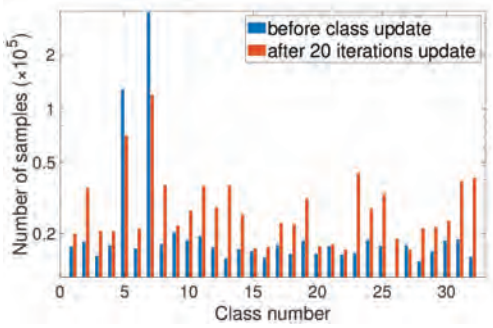

(a) Number of the training samples

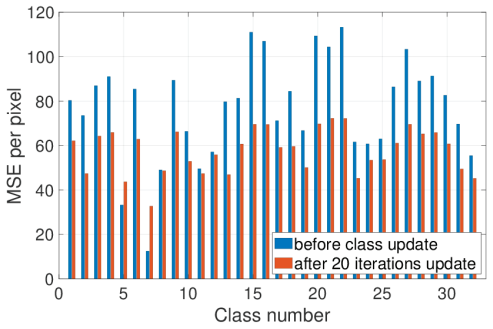

(b) MSE(per pixel)

Fig. 7 The number of training samples belonging to each class and their sparse representation MSE

Figure 7 shows the number of training samples belonging to each class and the MSE obtained by sparsely approximating those training samples using $T_0 = 3$ and $C = 32$. The blue bar in Fig. 7 shows MSE of initial classification and the red bar shows MSE after 20 iterations. In the initial classification based on DSIFT, the training sample distribution concentrates on some classes, but training samples are distributed among many classes with each class update iteration. For classes whose initial classification have large MSEs, it is found that after 20 class updates the MSE decreases dramatically. It is also found that sparse approximation yields an inverse correlation between the number of samples belonging to each class and MSE. This is because among the training image data, as the ratio of the low frequency vector rises above that of the high frequency vector, and the vector frequency falls, the reconstruction error becomes smaller. This tendency was also found in experiments using other numbers of classes or other sparsity parameters.

4.3 Initial classifier

DSIFT is based on an edge gradient histogram over orientation bins, and the atoms in the designed dictionary of each class can reflect the edge shape feature of the original block. In this subsection, we investigate how the convergence value and the convergence speed differ depending on the initial classification in the proposed algorithm.

Two classification methods, block-variance-based method (VAR) and random-assignment-based method (RAND), other than DSIFT were tested. Block variance is a measure of the spread of pixel values in a block, reflecting the sharpness and complexity of the edge. It is calculated by the following equation:

$$\mathrm{VAR} = \sum_i \sum_j (f(i,j) - M)^2 \quad , \tag{8}$$

where M is the average of pixel values in the block. For the initial classification, the blocks are classified into C classes by k-means method based on VAR. RAND is a method to assign C random variables of 1 to C as class numbers for each block, and it does not require any specific feature calculations. The experiment by RAND is intended to verify how the proposed method behaves when starting from random initial classification.

We designed three types of multiclass dictionaries under three initial classifications, DSIFT, VAR, and RAND. **Figure 8** shows the convergence characteristics of MSE when $C = 32$ and $T_0 = 5$. From Fig. 8, it can be seen that the dictionaries designed by initial classification with RAND without class update (i.e. the first K-SVD output dictionaries) have poor image representation performance. Moreover, MSE by the dictionaries designed by the initial classification by DSIFT becomes smaller than that by VAR. Moreover, regardless of which initial classification is used, MSE decreases and converges as the number of iterations increases. The three MSEs converge to almost the same value, but the convergence speed is the fastest for DSIFT. The similar tendency has shown by the measurement of convergence characteristics based on three kinds of initial classification methods under various C and T_0. From these results, it can be concluded that the proposed algorithm can design the high performance multiclass dictionaries regardless of initial classification method if the number of class update iterations is sufficiently large.

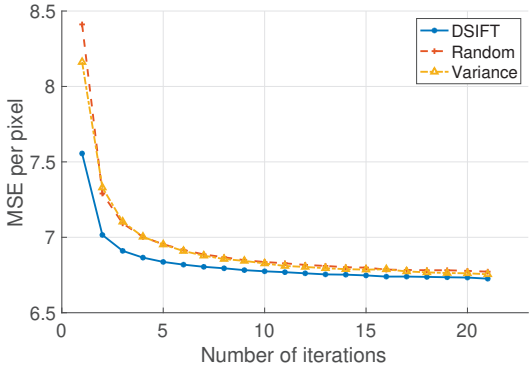

Fig. 8 Convergence characteristics based on three kinds of initial classification methods

4.4 Coding performance

This section examines the rate distortion characteristics to evaluate the performance of our approach.

Table 3 details the performance (Bjontegaard metric) of the proposed method[17] at different C and T_0 values. In generating the data, the proposed method used dictionaries designed with 20 iterations, while the reference method to be compared used dictionaries designed under initial classification. As described later, there is an appropriate T_0 in the range of the target bit rate (compression ratio). In other words, a small T_0 is effective for an application used in a low bit rate environment, and a large T_0 is effective for an application used in a high bit rate environment. Also, there is an appropriate C depending on the implementation environment of the encoder/decoder. In other words, if the memory available to the encoder and decoder is large, we can use dictionaries designed with a large C, but if the memory is small,

Table 3 BD-PSNR[dB] and BD-rate[%] of the proposed method against the conventional method without class update under the same C and T_0 as an anchor

T_0	C	BasketballDrive		BQTerrace		Cactus		ChristmasTree		Kimono1		ParkScene	
		PSNR	RATE	PSNR	RATE	PSNR	RATE	PSNR	RATE	PSNR	RATE	PSNR	RATE
3	32	0.85	-26.27	0.75	-26.32	0.78	-22.64	0.83	-40.58	0.67	-8.46	0.75	-17.27
	64	1.07	-32.27	0.95	-32.81	1.01	-29.59	0.95	-45.09	1.01	-13.15	0.9	-20.33
	128	1.03	-30.56	0.92	-30.75	0.99	-28.49	1.01	-48.26	0.98	-11.96	0.95	-21.23
5	32	0.79	-17.49	0.69	-17.17	0.75	-15.96	0.91	-26.59	0.43	-5.81	0.77	-12.97
	64	1.2	-25.88	1.02	-24.57	1.13	-23.61	1.16	-32.75	0.97	-14.06	1.05	-17.43
	128	1.12	-23.83	0.99	-23.6	1.09	-22.26	1.23	-34.7	0.92	-12.72	1.05	-17.32
7	32	0.84	-16.78	0.68	-15.03	0.77	-14.47	0.99	-22.2	0.46	-7.17	0.79	-12.12
	64	1.23	-23.56	1.04	-21.8	1.21	-21.97	1.35	-28.93	0.81	-12.07	1.18	-17.36
	128	1.16	-22.07	0.99	-20.35	1.13	-20.29	1.34	-28.3	0.89	-13.08	1.1	-16.2
9	32	0.85	-16.27	0.7	-14.62	0.78	-14.24	1.02	-19.56	0.56	-8.83	0.82	-12.2
	64	1.13	-20.59	0.99	-19.65	1.1	-19.09	1.4	-25.73	0.46	-6.7	1.18	-16.79
	128	1.13	-20.16	1.02	-19.69	1.13	-19.04	1.48	-26.32	0.77	-11.47	1.18	-16.45

we can use only dictionaries designed with a small C. Thus, we can say there are many cases where dictionaries designed with fixed T_0 and C are used, to satisfy the requirements of the encoder/decoder implementation and application environment. Therefore, in Table 3, C and T_0 of the conventional method used as anchors are the same as C and T_0 of the proposed method, respectively. As shown in Table 3, regardless of the number of classes and sparsity parameters, our approach attained significantly better BD-PSNR and BD-rate performance than the conventional approach. From Table 3, it can be seen that BD-PSNR improved from 0.4 dB to 1.5 dB for various images. In addition, the performance improvement in BD-rate was 6% to 48%, and reducing sparsity parameter T_0 increased the bitrate reduction.

In addition, the performance of the proposed method is compared with that of the conventional method in which the encoding is performed with the number of classes that gives the best performance. First, the dictionaries in the conventional method are designed by setting the number of classes to 1, 4, 16, 32, 64, 128, and 256. After that, the rate-distortion characteristics when encoding with each dictionary are obtained. Next, using the encoding performance when $C = 1$ (i.e. single class) as an anchor, the number of classes, C_{best}, with the best BD-rate is determined for each T_0. The result is shown in **Fig. 9**. Figure 9 shows the average BD-rate for the six test sequences, and almost the same results were also obtained for individual images. From Fig. 9, we can see that C_{best} is 32. Next, we summarize the BD-PSNR and BD-rate of the proposed method in **Table 4**, in which the anchor is the RD characteristic of the conventional method with C_{best}. Note that since $C_{best} = 32$, the row of $C = 32$ in Table 4 has the same value as Table 3. From the above considerations, it was confirmed that the coding performance of the proposed method also exceeded that of the conventional method using the number of classes which gives the best performance.

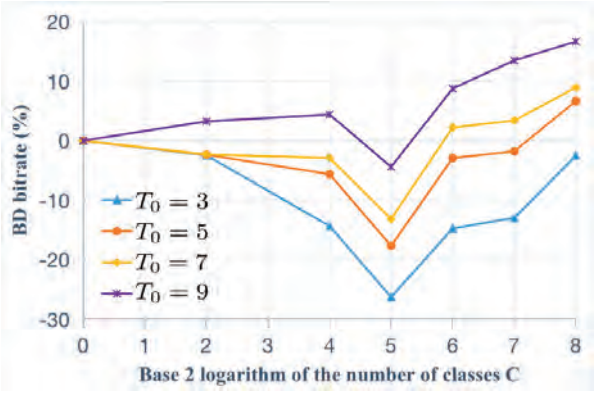

Fig. 9 BD bitrate against $C = 1$ as an anchor (without class update)

Figure 10 and **Fig. 11** show the PSNR and bit rate of the test image 'Cactus' and 'ParkScene' measured under the condition of $C = 32$, 64, and 128. In Fig. 10 and Fig. 11, all results include overhead information for class indices. Figures 10 (a), (c) and (e) show the rate distortion characteristics of the proposed method, and Figs. 10 (b), (d) and (f) show those of the conventional method. We can confirm the effectiveness of the proposed method relative to the conventional method under same C and T_0 by comparing Figs. 10(a), (c) and (e), with Figs. 10 (b), (d) and (f), respectively. Also, note that Figure 10 (b) is the result of encoding with the number of classes that gives the maximum performance in the conventional method. We can see that the performances of the proposed method shown in Figs. 10 (a), (c) and (e), are superior to the best performance of the conventional method shown in Fig. 10 (b). A similar discussion is pos-

Table 4 BD-PSNR[dB] and BD-rate[%] of the proposed method against the conventional method without class update under the best $C(= 32)$. Note that the values in the row for $C = 32$ are the same as in Table 3

T_0	C	BasketballDrive		BQTerrace		Cactus		ChristmasTree		Kimono1		ParkScene	
		PSNR	RATE	PSNR	RATE	PSNR	RATE	PSNR	RATE	PSNR	RATE	PSNR	RATE
3	32	0.85	-26.27	0.75	-26.32	0.78	-22.64	0.83	-40.58	0.67	-8.46	0.75	-17.27
	64	0.92	-27.50	0.80	-27.22	0.82	-23.22	0.88	-41.86	0.74	-9.42	0.80	-17.88
	128	0.99	-29.41	0.84	-27.68	0.90	-25.24	0.96	-45.50	0.84	-10.31	0.87	-19.29
5	32	0.79	−17.49	0.69	−17.17	0.75	−15.96	0.91	−26.59	0.43	−5.81	0.77	−12.97
	64	0.78	−16.88	0.66	−15.56	0.71	−14.08	0.88	−25.06	0.42	−5.44	0.74	−12.08
	128	0.81	−17.08	0.68	−15.44	0.75	−14.54	0.94	−26.64	0.48	−6.27	0.76	−12.45
7	32	0.84	−16.78	0.68	−15.03	0.77	−14.47	0.99	−22.20	0.46	−7.17	0.79	−12.12
	64	0.73	−13.78	0.64	−12.69	0.68	−11.65	0.95	−20.24	0.35	−4.90	0.71	−10.36
	128	0.78	−14.41	0.65	−12.34	0.70	−11.67	0.98	−20.29	0.41	−5.67	0.72	−10.40
9	32	0.85	−16.27	0.70	−14.62	0.78	−14.24	1.02	−19.56	0.56	−8.83	0.82	−12.20
	64	0.66	−11.72	0.60	−11.20	0.63	−10.17	0.92	−16.27	0.40	−5.86	0.68	−9.52
	128	0.68	−11.78	0.62	−11.05	0.63	−9.81	0.94	−16.40	0.41	−5.80	0.67	−9.21

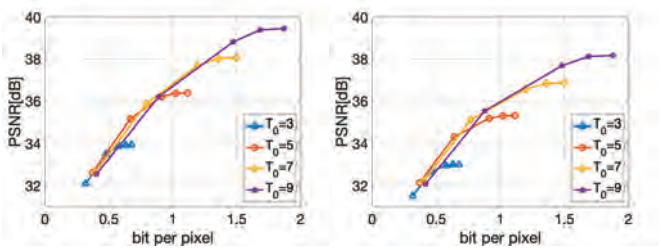

(a) proposed($C = 32$) (b) conventional($C = 32$:best)

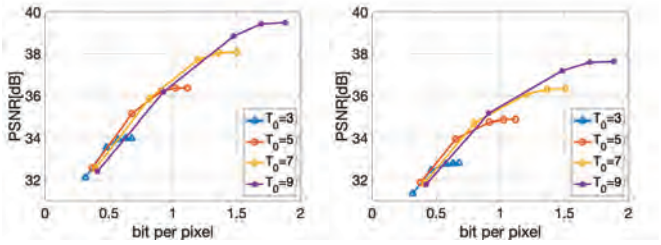

(c) proposed($C = 64$) (d) conventional($C = 64$)

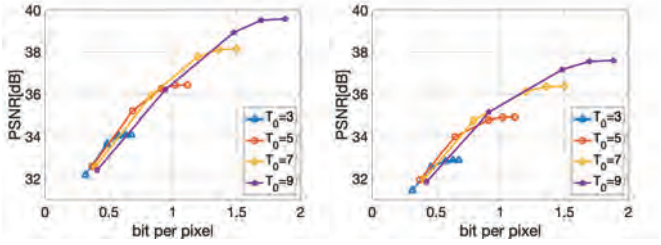

(e) proposed($C = 128$) (f) conventional($C = 128$)

Fig. 10 RD curves for Cactus

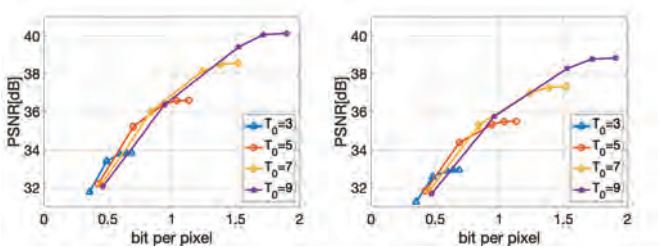

(a) proposed($C = 32$) (b) conventional($C = 32$:best)

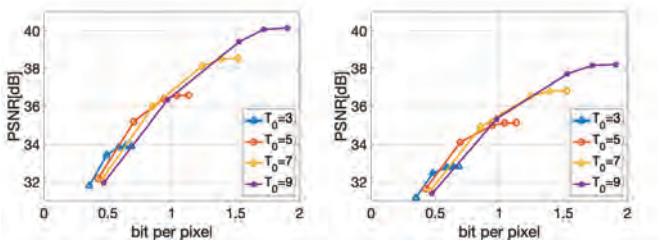

(c) proposed($C = 64$) (d) conventional($C = 64$)

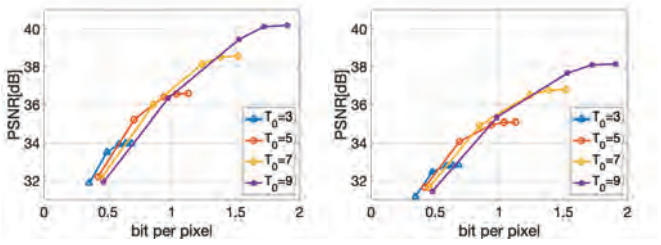

(e) proposed($C = 128$) (f) conventional($C = 128$)

Fig. 11 RD curves for ParkScene

sible from the results in Fig. 11. Figure 10 and Fig. 11 show that as sparsity parameter T_0 fell, the PSNR saturated at a lower bit rate, even if a finer quantization level was used. Therefore, in order to obtain a high PSNR, encoding must use a larger number of non-zero coefficients and the dictionaries designed with large T_0 values. On the other hand, in the low bit rate environment, where the number of non-zero coefficients to be encoded increases, the quantization step width must be coarse, which leads to a decrease in PSNR. These results suggest that it is better to use the dictionaries designed with large T_0 values when high bit rates are possible and to use the dictionaries designed with small T_0 values if only low bit rates are available. We have confirmed that the same trend is observed for different test images and different C values. In order to realize this idea, a method of switching multiple dictionaries designed with various C and T_0 for each target compression ratio or each image/block will be suitable. Although the multiple dictionaries designed for various C and T_0 must be shared by the encoder and decoder, the method is considered to be useful as an advanced coding control method for both the conventional method and the proposed method. These advanced RD optimization method by adapting C/T_0 is an important subject in the future study.

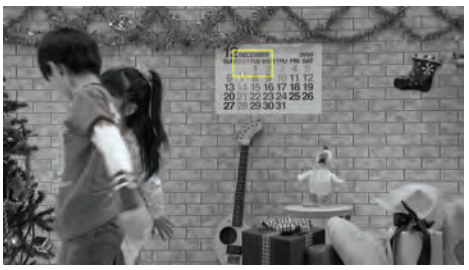

(a) ChristmasTree

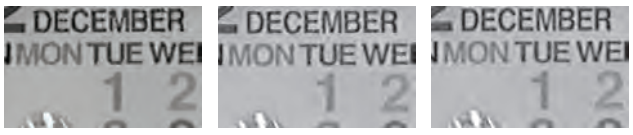

(b) Original (c) w/o class update (d) With class update

Fig. 12 Perceptual quality comparison for ChristmasTree (0.53 bit/pel, $C = 128$, $T_0 = 9$)

Subjective image quality is also improved by the proposed method. **Figure 12** compares the reconstructed images encoded at the same bit rate using dictionaries designed with $T_0 = 9$. It can be seen that the dictionary designed using class update can reconstruct detailed image structure with less visual degradation.

4.5 Consideration of selected class indices

Figure 13 shows a histogram of class index selection for each image when an image is coded using a dictionary

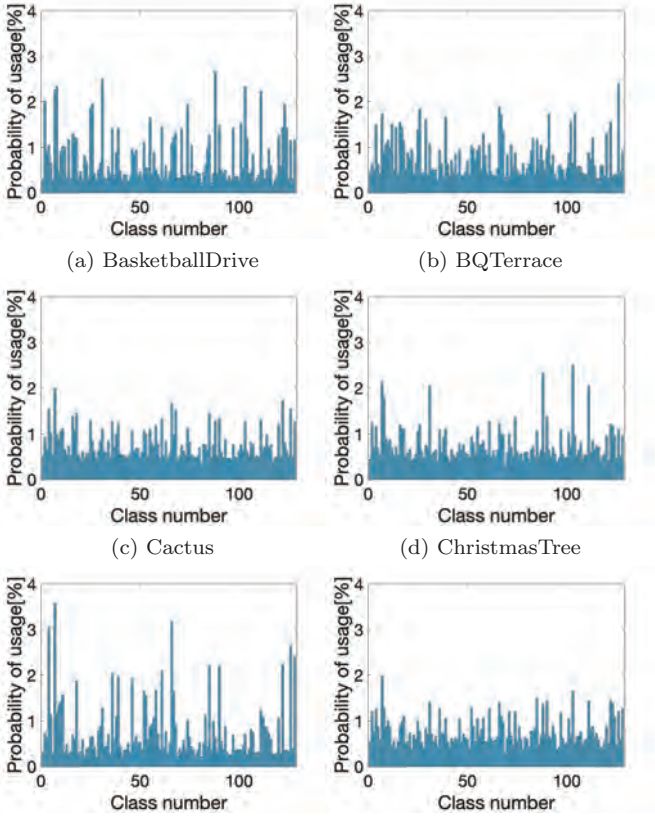

(a) BasketballDrive (b) BQTerrace

(c) Cactus (d) ChristmasTree

(e) Kimono1 (f) ParkScene

Fig. 13 Class selection probability ($T_0 = 3$, $C = 128$)

designed under the condition of $C = 128$ and $T_0 = 3$. From Fig. 13, it can be seen that the selection ratio of classes differs with the image, and that image reconstruction does trigger switching to the appropriate dictionary according to the distribution of the local features of the image to be encoded. **Figure 14** shows the relationship between the feature of the bases included in some dictionaries and the feature of the blocks that selected each of those dictionaries. Figure 14 (a) is a part of image " Park Scene ". Figure 14 (b), Fig. 14 (d) and Fig. 14 (f) show the blocks using the dictionaries shown in Fig. 14 (c), Fig. 14 (e) and Fig. 14 (g), respectively. We can see that the blocks in Fig. 14 (b), Fig. 14 (d) and Fig. 14 (f) contain vertical, diagonal and horizontal edge, respectively, and the selected dictionary contains many bases that reflect the block feature. These confirm the effectiveness of the multi-class dictionary approach. Also, since there is no class index that is rarely used, it can be said that the number of classes is not excessive.

Next, we consider the local correlation of class indices. If the class indices of neighboring blocks are highly correlated, applying the following rules in code assignment may reduce the total code length. Let C_P be the class index of the target block, C_A be the class index of its left neighboring block, and C_B be the class index of its upper

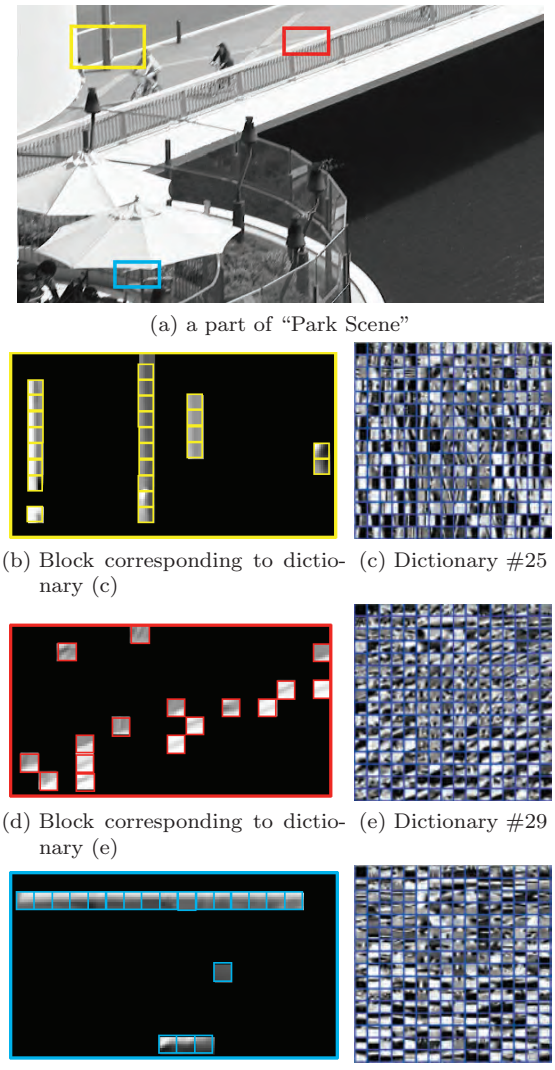

(a) a part of "Park Scene"

(b) Block corresponding to dictionary (c) (c) Dictionary #25

(d) Block corresponding to dictionary (e) (e) Dictionary #29

(f) Block corresponding to dictionary (g) (g) Dictionary #88

Fig. 14 Example of relationship between the feature of blocks and the selected dictionary

neighboring block. The code assignment rule is,

- "00" if $C_P = C_A$
- "01" if $C_P = C_B$
- "1"+"fixed length code with $\lceil \log_2 C \rceil$ bit" otherwise.

The number of bits yielded by the above rule is smaller than that yielded by fixed length coding only when the probabilities of $C_P = C_A$ or $C_P = C_B$ are larger than 0.25 ($C = 32$), 0.2 ($C = 64$), 0.167 ($C = 128$), respectively. We measured the probability that the class index of a block to be coded is the same as the class index of its left or upper neighboring blocks for the six test images in Fig.4 under $T_0 = 3$. They were 0.118, 0.076, 0.054 for the case of $C = 32$, $C = 64$ and $C = 128$, respectively. This result suggests that the class index has only slight local correlation, and that using a variable length code to the class has little benefit. Therefore, as described in section 3.2, it is appropriate to assign a fixed length code to each

class index.

5. Conclusions

This study proposed a multi-class K-SVD method that considers interdependency of classification performance and dictionary design. In the proposed method, after multiple dictionaries are designed by K-SVD, sparse coding for each training vector is performed using all of the dictionaries. As a result, the training vector is reclassified into the class that best approximates it. By iteratively performing the dictionary design stage and the class update stage, it is possible to design dictionaries that enable more efficient sparse representation. Experiments on still images revealed that the proposed algorithm gives a significant coding gain compared to the conventional method based on fixed classification with predetermined features.

We believe that the proposed method can be further expanded in more directions and also has high potential as regards research. First, the proposed method can be extended to multi-class dictionary design for residual signals of intraframe prediction as used in H.265/HEVC. Considering its application to videos, it can also be applied to dictionary design for motion compensation prediction error. In addition, the class selection strategy under rate-distortion optimization and the adaptive switching method of multiple dictionaries which are designed with different sparse constraint parameters, are considered to be interesting viewpoints of future research. Moreover, introducing a dynamic class merge process in the middle of iterated dictionary design offers attractive research directions for producing more compact sets of dictionaries that can improve coding efficiency.

References

1) M. Aharon, M. Elad, A. Bruckstein: "K-SVD: An Algorithm for Designing Overcomplete Dictionaries for Sparse Representation", IEEE Trans. on Signal Processing, Vol.54, No.11, pp.4311–4322 (2006).
2) O. Bryt, M. Elad: "Compression of Facial Images Using the K-SVD Algorithm", Journal of Visual Communication and Image Representation, Vol.19, No.4, pp.270–282 (2008).
3) Je-Won Kang, M. Gabbouj, C.C.J. Kuo: "Sparse/DCT (S/DCT) Two-Layered Representation of Prediction Residuals for Video Coding", IEEE Trans. on Image Processing, Vol.22, No.7, pp.2711–2722 (2013).
4) J.W. Kang, C.C.J. Kuo, R. Cohen, A. Vetro: "Efficient Dictionary Based Video Coding with Reduced Side Information", Proc. of 2011 IEEE International Symposium of Circuits and Systems (ISCAS), pp.109–112 (2011).
5) Y.C.C. Pati, R. Rezaiifar, P.S.S. Krishnaprasad: "Orthogonal Matching Pursuit: Recursive Function Approximation with Applications to Wavelet Decomposition", Proceedings of 27th Asilomar Conference on Signals, Systems and Computers, pp.1–5 (1993).
6) J.R. Ohm, G.J. Sullivan, H. Schwarz, T.K. Tan, T. Wiegand: "Comparison of the Coding Efficiency of Video Coding Standards–Including High Efficiency Video Coding (HEVC)", IEEE Trans. on Circuits and Systems for Video Technology, Vol.22, No.12, pp.1669–1684 (2012).
7) R. Walha, F. Drira, F. Lebourgeois, C. Garcia, A.M. Alimi: "Multiple Learned Dictionaries Based Clustered Sparse Coding for the Super-Resolution of Single Text Image", Proc. of IEEE 12th International Conference on Document Analysis and Recognition, pp.484–488 (2013).
8) T. Guha, R.K. Ward: "Learning Sparse Representations for Human Action Recognition", IEEE Trans. on Pattern Analysis and Machine Intelligence, Vol.34, No.8, pp.1576–1588 (2012).
9) Q. Zhang, B. Li:"Discriminative K-SVD for Dictionary Learning in Face Recognition", Proc. of 2010 IEEE Computer Society Conference on Computer Vision and Pattern Recognition (2010).
10) Z. Jiang, Z. Lin, L. S. Davis:"Learning a Discriminative Dictionary for Sparse Coding via Label Consistent K-SVD", Proc. of IEEE Computer Vision and Pattern Recognition 2011 (CVPR 2011) (2011).
11) D. Zhang, P. Liu, K. Zhang, H. Zhang, Q. Wang, X. Jing:"Class Relatedness Oriented-Discriminative Dictionary Learning for Multiclass Image Classification", Elsevier, Pattern Recognition, Vol.59, pp.168–175 (2016).
12) A. Vedaldi, B. Fulkerson: "Vlfeat: an Open and Portable Library of Computer Vision Algorithms", Proc. of the international conference on Multimedia - MM'10, p.1469, ACM Press (2010).
13) B. Olshausen, D. Field: "Natural Image Statistics and Efficient Coding", Network: Computation in Neural Systems, Vol.7, No.2, pp.333–339 (1996).
14) R. Vinith, A. S. Aswani, K. Govindan: "Medical Image Compression Using Sparse Approximation", International Journal of Advanced Computer and Mathematical Sciences, Vol.6, No.2, pp.30–39 (2015).
15) HDTV Test Materials for Assessment of Picture Quality, The Institute of Image Information and Television Engineering (2009).
16) Ultra-High Definition/Wide-Color-Gamut Standard Test Images, The Institute of Image Information and Television Engineering (2014).
17) G. Bjontegaard: "Calculation of Average PSNR Differences between RD-Curves", Technical Report VCEG M-33, ITU-T SG16/Q.6 (2001).

(Received December 14, 2019)
(Revised March 21, 2020)

Ji WANG
He received the B.E. and M.E. degrees from Chiba Institute of Technology, Chiba, Japan, in 2012 and 2014, respectively. Currently he is studying in Graduate School of Information and Computer Science, Chiba Institute of Technology. His research interests include next generation video coding and machine learning.

Yukihiro BANDOH
He received the B.E., M.E., and Ph.D. degrees from Kyushu University, Japan, in 1996, 1998 and 2002, respectively. He granted JSPS Research Fellowship for Young Scientists from 2000 to 2002. In 2002, he joined Nippon Telegraph and Telephone (NTT) Corporation, where he has been engaged in research on efficient video coding for high realistic communication. He is currently a distinguished engineer at NTT Media intelligence Laboratories.

Atsushi SHIMIZU
He received the B.E. and M.E. degrees in electronic engineering from Nihon University in 1990 and 1992 respectively. He joined Nippon Telegraph and Telephone (NTT) Corporation in 1992 and was engaged in video compression algorithm and software development. He is currently in NTT TechnoCross Corporation.

Yoshiyuki YASHIMA (*Member*)
He received the B.E., M.E., and Ph.D degrees from Nagoya University, Nagoya, Japan, in 1981, 1983 and 1998, respectively. In 1983 he joined the Electrical Communications Laboratories, Nippon Telegraph and Telephone Corporation (NTT), Kanagawa, Japan, where he has been engaged in the research and development of high quality HDTV signal compression, MPEG video coding algorithm and standardization. He was also a visiting professor of Tokyo Institute of Technology during 2004-2007. In 2009, he moved to Chiba Institute of Technology. Currently, he is a professor at the Faculty of Information and Computer Science, Chiba Institute of Technology. His research interests include next generation video coding, pre- and post-processing for video coding, processing of compressed video, compressed video quality metrics and image analysis for video communication system. He was awarded the Takayanagi Memorial Technology Prize in 2005, and received the FIT Funai Best Paper Award in IEICE in 2008. Professor Yashima is a Fellow member of the IEICE, a senior member of the IEEE, and a member of ACM, IPSJ and ITE.

IIEEJ Paper

A Configurable Fixed-Complexity IME-FME Cost Ratio Based Inter Mode Filtering Method in HEVC Encoding

Muchen LI[†], Jinjia ZHOU[†,‡] *(Member)*, Satoshi GOTO[††]

[†] School of Science and Engineering, Hosei University, [‡] JST, PRESTO, Tokyo, Japan,
[††] Egypt-Japan University of Science and Technology

<Summary> This paper presents a fixed-complexity inter mode filtering algorithm for High Efficiency Video Coding (HEVC). Motion estimation (ME) particularly the fractional motion estimation (FME) is the most computational challenge part because of the optimized Rate-Distortion (RD) evaluation for coding blocks with different sizes and prediction modes. Especially when HEVC introduces new tools like the coding tree unit and asymmetric motion partition (AMP), complexity of ME has increased furthermore. There are many approaches to reducing the ME complexity by removing the unlikely prediction modes. However, most mode filtering methods cannot guarantee the worst-case performance and limit overall speed in a pipelined video encoder. Thus, a fixed number of modes is required to ensure the worst-case performance and realize the pipeline design. By investigating the cost correlation of integer motion estimation (IME) and FME, we utilize the confidence interval (CI) of the cost ratio to remove fixed number of modes. Moreover, the dedicated configurable mode filtering makes the complexity of FME adaptive to different requirements of RD performance. According to experiment in HEVC reference software HM 16.0 with full FME, the proposed scheme achieves at almost 82.75% complexity reduction of the FME with an average of 1.63% BD rate loss.

Keywords: IME, FME, cost ratio, inter mode, HEVC

1. Introduction

With the enormous development of electronic devices, high definition videos such as High Definition (HD), Quad Full High Definition (QFHD), even Super Hi-Vision (SHV) videos have appeared in our daily lives which brings challenges to the existing video compression formats. As a successor to H.264/AVC (advanced video coding)[1], HEVC[2] is developed by the Joint Collaborative Team on Video Coding (JCT-VC) group to meet the increasing demand of compression efficiency. By adopting many new tools such as hierarchical quad-tree coding structure, asymmetric motion partition (AMP), advanced motion vector prediction (AMVP), and merge[2)-4)], HEVC greatly improves the coding efficiency. It is shown that HEVC reference video codec HM[5] currently achieves about 50% bitrate reduction with same subjective quality compared to H.264/AVC. However, these innovations also increase the encoding complexity that is not friendly for real-time applications. Motion estimation (ME) is one of the most complex part in HEVC, which is the major issue involved in this work.

ME is a coding method of exploiting redundancy between frames. It creates prediction blocks from previously coded frames and finds the optimal match for the current block, which leads to high complexity in the encoding from the following three aspects. Firstly, it invokes a series of computationally expensive operations, such as interpolation for fractional motion vector and Rate-Distortion (RD) evaluation. Secondly, with the quad-tree coding structure, a coding tree unit (CTU) can be split into four coding units (CU) recursively in multiple depths. Thirdly, additional AMP modes are introduced. Traversal on CU in different depths and prediction modes results in high computation complexity. It is reported that ME brings 50%~70% complexity of the whole encoding in HEVC.

There are many previous works for reducing computation complexity of ME that can be classified into two categories[6)-13)]. The first category is to simplify the process of motion search, for example, fast motion search algorithm of reducing the searched points or iterations[6)-8)]. The second one is reducing the ME operations by removing some traversal nodes of CU types and prediction modes. Our proposal belongs to the second one that is usually called mode filtering method. There are also plenty of literatures about the mode filtering [9)-13)]. J. Kim et.al give a method that detects skip mode early and removes most of inter mode evaluations in the CU level[9)]. Q. Yu et. al employ a CU splitting early termination scheme to skip CUs in some depths when the coding block coefficient meets certain

conditions[10]. L Shen et. al propose a depth selection method based on the information of neighboring blocks[11]. However, the main problem of these works is that the number of kept modes is highly content-dependent and uncertain. It cannot guarantee the worst-case of performance for the architecture, which limits their overall speed in a pipelined video encoder. G.Y. Zhong et. al[12] give a solution that chooses a fixed number of modes for each depth. However, it does not consider the content difference of CTUs and there are still quite a few kept modes. The time reduction and video quality can be improved furthermore.

Our previous publication[13] gave a fixed-complexity mode filtering method based on cost ratio of integer motion estimation-fractional motion estimation (IME-FME), and the related confidence intervals. This work achieves great RD performance enhancement through selecting the different cost function and applying different confidences intervals with various quantization parameters (QPs) and depths. The rest of this paper is organized as follows. Section 2 introduces the related ME techniques and analyzes the complexity of them. Section 3 investigates the different cost ratio of IME-FME and presents a configurable fixed-complexity schemes. Section 4 discusses the simulation results based on HM 16.0 [5]. Final conclusions are drawn in section 5.

2. Motion Estimation in HEVC

2.1 Quad-tree coding structure and inter mode

HEVC incorporates the flexible quad-tree structure for content adaptive coding. A picture is divided into a sequence of CTUs. A CTU can be represented by a single CU, or it can be further divided into CUs in a quad-tree structure recursively until the smallest CU (SCU) size is reached. CTU size can be as large as 64×64 and SCU can be as small as 8×8. **Figure 1** gives an example that 64×64 CTU is partitioned into CUs with four quad-tree depth[2)-4)]. The CU in bold is further split into four CUs in the next depth.

In inter prediction, each CU can be partitioned into one or more prediction units (PUs). As shown in **Fig.2**, for a CU of 2N×2N, besides symmetric partition modes that already known from H.264/AVC, another four asymmetric motion partition (AMP) modes are defined in HEVC. In this figure, N equals half of the width/height at the CU; n equals to N/2. The indices U, D, L and R denote the partition orientation Up, Down, Left and Right. PART_N×N is only used for SCU to avoid redundant representation. According to default HM, for the CU of 8×8, only three modes

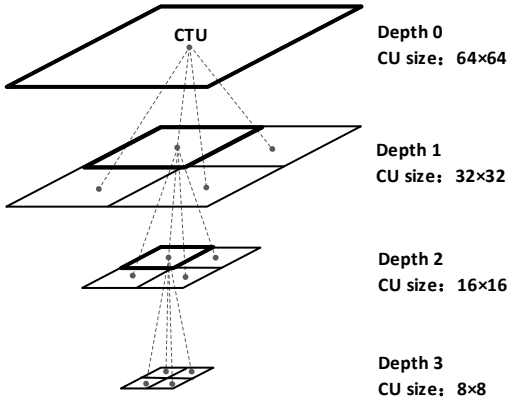

Fig.1 Quad-tree partitioning of a CTU

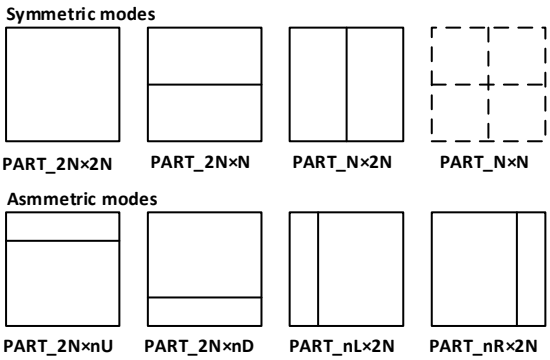

Fig. 2 Inter partition modes for a CU of size 2N×2N

(PART_2N×2N, PART_2N×N, PART_N×2N) are in use to limit the complexity of coding scheme [2)-4)].

2.2 Motion estimation and Rate-Distortion measure

As illustrated in **Fig.3**, ME is a process that uses block matching algorithm to find the best matching block in previously coded pictures (reference pictures) for a current block. The search is performed in a search range around the collocated block. The displacement of the collocated block and best match is known as motion vector. The determination of the best matching is subject to the Rate-Distortion (RD) cost function $J=D+\lambda \times B$, wherein D measures the difference of the Matching block, B represents the bit cost on the motion vector [3)].

According to HM, ME is usually divided into integer motion estimation (IME) and fractional motion estimation (FME). IME performs a coarse search over the search range and generates an integer-pixel motion vector. Cost functions of Eq. (1) is used in IME, where sum of absolute difference (SAD) is the distortion measure and B_{pred} specifies the bit cost on motion information. λ_{pred} is a QP based Lagrangian

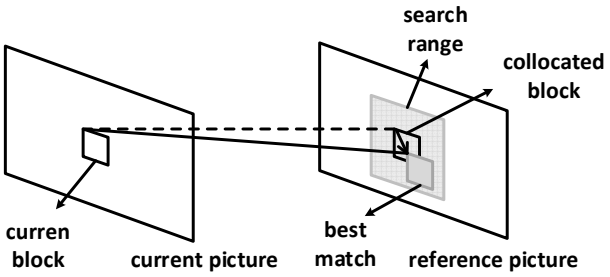

Fig. 3 Motion estimation

multiplier for motion vector decision.

$$J_{pred,SAD} = SAD + \lambda_{pred} \times B_{pred} \quad (1)$$

FME performs a fine search in sub-pixel accuracy around the integer motion vector derived in IME. In this process, computation intensive interpolation filtering is involved to generate the half-pixel and quarter-pixel samples. Since the distortion costs among neighboring sub-pixel samples are similar, higher accuracy is required for the distortion computation for motion estimation. Cost function of Eq. (2) is employed in FME. Hadamard transformed difference (HAD) is the distortion measure, which is more complex than SAD since it involves the transform of a block. With the processes of transform and interpolation mentioned above, FME has much higher computation complexity than IME, especially when IME is greatly accelerated by the fast search tools such as TZ search that implemented in HM [4].

$$J_{pred,HAD} = HAD + \lambda_{pred} \times B_{pred} \quad (2)$$

After the decision of fractional motion vector, partition modes of each CU are evaluated, and the best mode is selected. Then, the cost of the CU will be compared to the cost sum of the four sub-CUs in the next depth for deciding whether the further split is needed or not. More precise decision is required to maximize the coding gain in the mode decision and CU depth selection. Thus, sum of square error (SSE) based cost function of Eq. (3) is used in these processes. λ_{mode} is the Lagrangian multiplier for mode decision. B_{mode} represents bit cost of encoding the whole block that includes the information of motion, mode and residual. The calculation of J_{mode} needs intensive computation since it involves (inverse) transform, (inverse) quantization, reconstruction and entropy coding. These procedures are highly dependent with each other and results in high cost in real-time implementations. The J_{mode} cost-based decision is also called full rate distortion optimization (full RDO) [4), 5)].

$$J_{\text{mode}} = SSE + \lambda_{\text{mode}} \times B_{\text{mode}} \quad (3)$$

Above all, different RD cost functions are employed in different steps of ME. RD cost checks traversing on the quad-tree structure and multiple prediction modes make ME the most computational challenging part in HEVC encoding. Motion search for IME part requires large external memory access, which is a power consuming part in hardware design. Literatures [14), 15)] have proposed several efficient solutions for the IME part and greatly reduced the external memory bandwidth. Moreover, interpolation of FME also brings high cost in hardware area which is discussed in the next section.

3. Proposed Fixed-Complexity FME Mode Filtering

FME is the major part in ME in terms of computation expense on the processes of interpolation and RD cost evaluation. Our simulation shows that even with only one reference frame, the FME occupies more than 50% of the encoding time. Therefore, low complexity FME algorithm is critical for realizing fast encoding. Moreover, the interpolation and the full RDO result in high hardware cost. Reducing the operation times of interpolation and full RDO can save a lot of cost on logical gates [14) 16)]. Our work proposes a mode filtering algorithm to reduce the number of modes to a fixed level for the FME part. This section firstly introduces a two-loop ME structure and the incorporated module of mode filtering. A new complexity measurement is defined and how the proposed mode filtering module effects on the FME complexity is explained. Then the investigation on the cost ratio of IME-FME and a cost ratio-based mode filtering algorithm is presented. Finally, the configurable scheme is discussed.

3.1 Overview of the proposed mode filtering

In original HM, IME and FME for each CU are performed sequentially in one loop, as illustrated in **Fig. 4(a)**, the RD cost of all the partition modes are checked by IME and FME in sequence. After that, inter mode with the selected partition mode is compared with the modes of PCM, intra and skip for the CU compress. When a CTU is compressed with the one loop ME structure, the processing of next CU will not be started until both IME and FME of the current CU are all finished. In order to increase the parallelism, the inter-dependency of IME and FME in one CU are usually removed in real-time applications.

In this work, IME and FME in a CTU are departed into two loops and the proposed mode filtering algorithm is applied based on a two-loop ME structure, as illustrated in Fig.4(b). The left part is the IME loop, in which all the prediction modes for all the CUs across different depths are checked by IME. The generated integer motion vectors and IME costs for all CUs will be transmitted to the module of mode filtering that selects a certain amount of modes for the following FME loop. The integer motion vectors of the selected modes are fed into the FME loop wherein the fractional motion search and estimation are performed to decide the best inter mode. With the two-loop ME structure, FME for a CU will not be started before the IME for all the CU in the same CTU are completed.

Since motion vectors are predicted from neighboring blocks, separation of IME and FME inevitably leads to inaccurate prediction of MVs. Our simulation shows that the two-loop structure without mode filtering module increases the BD rate by 0.09% and the encoding time by 3% compared with one loop structure. The coding efficiency loss is negligible. With the two-loop ME structure, the most computationally intensive FME and the following mode decision process is departed from IME. By applying efficient mode filtering algorithm before FME, only a limited number of modes with good IME costs will be selected for the FME and full RDO. If the complexity of FME can be reduced to a fixed level, it will benefit the pipeline design for IME and FME.

In this paper, we introduce a new complexity measurement for FME. Usually, execution time is used as complexity measurement that is related to the content of the processed picture, and other coding parameter like QP values. However, for a CU with the same size, the number of pixels that needs to be processed in the FME is the same. In other words, the operation times related to hardware cost are the same. Therefore, we introduce a more direct and simple definition 'layer' to measure the complexity of FME. The layer is proportional to the size of CU no matter what partition mode they use. According to the HM with default configuration, CTU is configured as 64×64 and four depths are allowed. Seven modes can be selected for the CU in depth 0, 1, 2 and three modes can be selected for the CU in depth 3. We define the FME complexity of processing a 64×64 CU for one mode as 1 layer. If seven modes are evaluated, the complexity of depth 0 is 7 layers. In depth 1, the CU size is 32×32 and FME complexity is 1/4 layer for one mode. Since there are 4 CPUs and seven modes in depth 1, the FME complexity of depth 1 is still 7 layers. It is easy

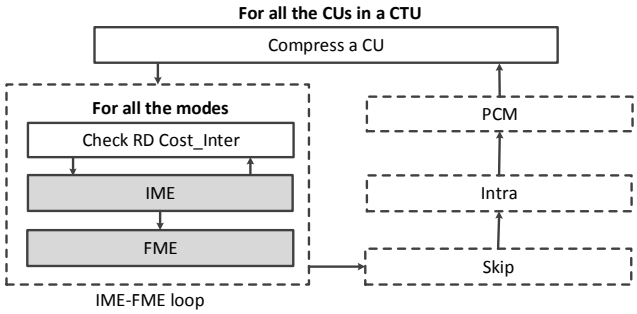

(a) One loop ME structure

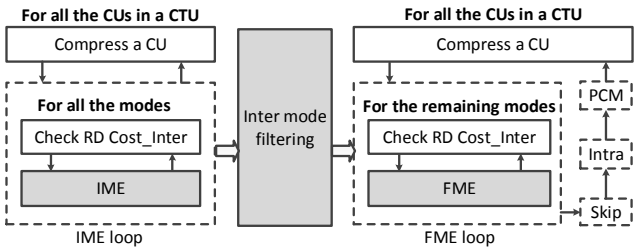

(b) Two-loop ME structure with an inter mode filtering module

Fig. 4 One loop and two-loop ME structures

to find that the complexity of each depth is the same with the allowed number of modes for this depth. Therefore, the FME complexity for the whole CTU is 24(=7+7+7+3) layers.

3.2 Proposed cost ratio-based mode filtering algorithm

The mode selection includes two aspects. One is mode selection in the same depth. The other is mode selection across different depths, which is called depth selection here. In the latter case, a CU can be further split into 4 sub-CUs, the RD cost of this CU in the upper depth is compared with the cost sum of the four sub-CUs in the next depth in order to decide whether the further split is necessary. If the depth is selected, the corresponding mode of the CU in this depth is necessary. Otherwise, the corresponding modes can be omitted. In depth selection, since the number of partitions increases a lot after being split into lower depth, the side information of encoding motion vectors increases significantly, especially for the case of low motion (since the distortion is also small). Thus, it will lead to great error if the IME cost is directly used for the depth selection. In order to make better use of IME costs for the depth selection, the relationship of IME cost and FME cost is investigated in the next section. The FME cost here does not only refer to the cost of $J_{pred,HAD}$ that used in the fractional motion vector decision but also the cost calculated based on the derived fractional motion vector, such as J_{mode}. Similarly, IME cost

refers to the cost calculated based on the integer motion vector.

3.2.1 Distribution of cost ratio and the related confidence interval

Figure5 depicts a scatter plot of IME cost and FME cost for the sequence of BQSquare with QP equals to 22. The horizontal axis C_i refers to the cost of IME while the vertical axis C_f refers to the cost of FME. The cost ratio of IME-FME is defined as Eq. (4) .

$$R_{f/i} = C_f / C_i \tag{4}$$

In Fig.5, IME cost is $J_{pred,SAD}$ and FME cost is J_{mode}. As shown in the figure, most of the points distribute in the area that clamped by line a and line b. The value of $R_{f/i}$ can be thought of being distributed within a range of $[a, b]$. That is

$$a \leq R_{f/i} \leq b \ . \tag{5}$$

It implies that large IME cost does not necessarily results in large FME cost. That is why the IME costs are not used directly for the mode decision for all the cases.

Supposing the cost ratio of $R_{f/i}$ confirms to normal distribution, $[a, b]$ can be regarded as a confidence interval (CI) that constructed with a given confidence level. By fitting a probability distribution to the sample data of $R_{f/i}$ with MATLAB, normal distribution of $R_{f/i}$ with two parameters μ (mean value) and σ (standard deviation) can be created. If we choose a confidence level $\alpha \in (0,1)$, the upper limit and lower limit of the confidence interval can be calculated as $\mu \pm Z_{\alpha/2}\left(\frac{\sigma}{\sqrt{n}}\right)$, where the critical value $Z_{\alpha/2}$ can be derived by checking the Z-table[17]. Giving different confidence levels, different confidence intervals can be derived.

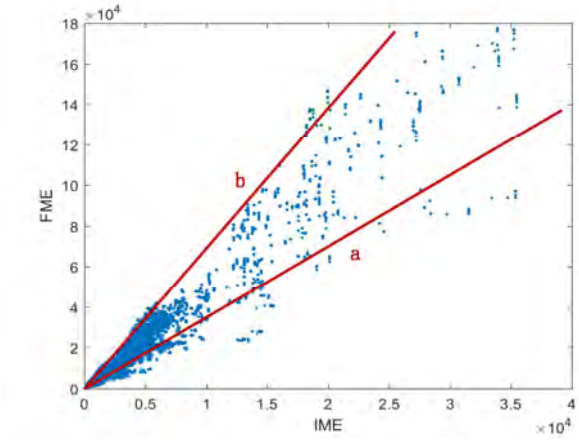

Fig. 5 IME cost and FME cost for the sequence of BQSquare

Figure 6 gives the probability density function (PDF) of the $R_{f/i}$ related to $J_{pred,SAD}$ and J_{mode}. It is obvious that there are some bias and the function is not completely fit with the normal distribution. From our investigation, we find that the cost ratio can generally follow the normal distribution if the cost functions of the IME and FME are carefully selected. As shown in **Fig.7,** if the SAD is used as IME cost and HAD is used as FME cost, the PDF of $R_{f/i}$ fits well with normal distribution. According to the distribution of cost ratio, it is possible to estimate the confidence interval of FME cost with the IME cost.

3.2.2 Confidence interval-based mode filtering (CI-MF)

Our simulation shows that the confidence interval varies with QP and depth for a given confidence level.

If the cost ratio and related confidence interval of depth *n* is represented as Eq. (6),

$$a_n \leq R_{(f/i)_n} = \frac{C_{f_n}}{C_{i_n}} \leq b_n \,, \tag{6}$$

for different depth k and j, we get

$$a_k \leq R_{(f/i)_k} = \frac{C_{f_k}}{C_{i_k}} \leq b_k \ , \tag{7}$$

$$a_j \leq R_{(f/i)_j} = \frac{C_{f_j}}{C_{i_j}} \leq b_j \ . \tag{8}$$

If the following condition of Eq. (9) is satisfied,

$$b_j C_{i_j} < a_k C_{i_k} \quad (\text{that is } \frac{C_{i_k}}{C_{i_j}} > \frac{b_j}{a_k}) \tag{9}$$

we can get

$$C_{f_k} > C_{f_j} \ . \tag{10}$$

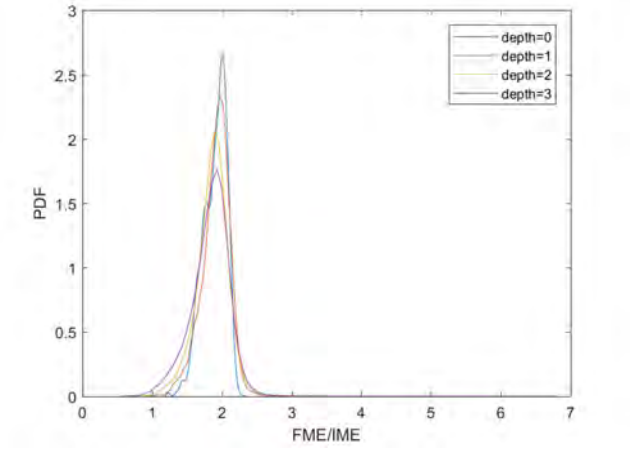

Fig. 6 PDF of cost ratio of $J_{pred,SAD}$-J_{mode} for the sequence of BQSquare

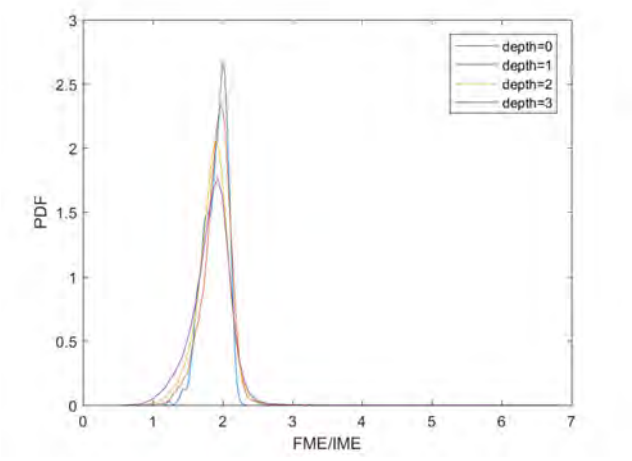

Fig.7 PDF of cost ratio of SAD-HAD for the sequence of BQSquare

If depth *k* is the upper depth, this conclusion means that FME cost of the CU in depth *k* is lar ger than the cost sum of the corresponding sub-CUs in depth *j*. In other words, depth *k* should have lower priority and is more likely to be removed for this CU. From the above derivation, we find that the depth selection is realized by comparing the IME cost ratio to a parameter that is related to the confidence intervals. The parameter is called mode filtering parameter (MFP) and this depth selection method is called confidence interval-based mode filtering (CI-MF). The related confidence intervals can be derived from training based on the distribution of cost ratio from the statistics.

Since there are up to seven modes in one depth, it is complex to compare each mode in the current depth to the other mode combinations in the lower depth. In order to simplify the comparison, some unlikely modes are firstly removed for each depth. Then the depth selection is performed among the kept modes. For the same depth, since each mode includes one or two partitions, bit cost of all the modes are in the same level. Thus, the SAD-based IME cost is directly used for the mode selection in the same depth. To avoid large performance loss, two modes with the smallest IME costs are kept.

For the depth selection, the previous work[13] uses the cost ratio of $J_{pred,SAD}$-J_{mode} which is in accord with the original HM. This work employs the cost ratio of SAD-HAD for the following three reasons. Firstly, the confidence interval is derived from the statistic of cost ratio $R_{f/i}$. Based on the assumption that the cost ratio conforms to the normal distribution, cost ratio of SAD-HAD is much better in terms of the conformity with normal distribution. Secondly, since depths are checked from upper to lower, modes in the upper depth that meet certain conditions will be selected firstly, which gives higher priority to the upper depth. It can be taken as a complement of removing the part of bit cost from the cost function. Thirdly, it is very common that HAD or HAD based cost are directly used as the measurement of mode decision, since the calculation of J_{mode} is complex and relatively hard to be implemented in real application[18)-20)].

The other problem is how to reduce the complexity to a fixed level. The complexity of a CU in terms of layers is proportional to size and allowed number of modes of this CU. For each CTU, there are up to 85 CUs with 339 modes needs to be checked in some order. It is difficult to control the whole complexity of a CTU in a fixed level if the number of kept modes for each CU is different and random. This work keeps the same number of modes for the CUs in the same depth. CUs in the depth with higher priority will be assigned more modes. The complexity of each depth in terms layers is equals to the allowed number of modes, and the whole complexity of a CTU equals to the sum of the allowed numbers for all the depths. By adjusting the allowed number of modes for each depth, the whole complexity of the CTU can be controlled easily.

Figure 8 depicts the process of CI-MF for one depth. Cost of the current depth is compared with that of other lower depths to evaluate their priorities. For depth 0, the lower depths are depth 1, 2 and 3. Cost of a depth is defined as the cost sum of all the CUs in this depth. As mentioned previously, before depth selection, the best two modes with smaller IME cost are kept for each CU. Therefore, the cost of a depth has a range with a minimum and a maximum value. For depth 0, there is only one CU, thus the minimum and maximum cost of this depth are the cost of the best mode and the second-best mode of the CU, respectively. In the flow chat of Fig.8, depth *n* is the current depth needs to be processed. For depth *n*, the minimum cost and maximum cost are marked as C_{n0} and C_{n1}. C_{n0} equals the cost sum of the best modes for all the CUs in this depth and C_{n1} equals the cost sum of all the second-best modes. Two cost values of the current depth are compared to the average cost of other lower depths respectively to decide how many modes are kept for this depth. C_{nLower} is used to represent the average cost of the lower depths, which is calculated as Eq. (11). B_{nLower} is the average upper limit of CIs of other lower depths which is calculated as Eq. (12). MFP_n is the mode filtering parameter that related to CI. It is defined in Eq. (13), where a_n is the lower limit of CI for depth *n*. All the parameters mentioned above are not used for depth 3 (*n*

should not be 3), since the allowed number of modes of the last depth can be calculated directly when the upper depths are all processed.

$$C_{nLower} = \frac{1}{(3-n)} \sum_{l=n+1}^{3} \frac{C_{l0} + C_{l1}}{2}, \quad (0 \le n \le 2) \tag{11}$$

$$B_{nLower} = \frac{1}{\sum_{l=n+1}^{3} 4^l} \sum_{l=n+1}^{3} 4^l b_l, \quad (0 \le n \le 2) \tag{12}$$

$$MFP_n = \frac{B_{nLower}}{a_n}, \quad (0 \le n \le 2) \tag{13}$$

M_n in the flow chart is used to record the number of kept modes and it is initialized to 0. For the complexity control of the whole CTU, M_n should be limited in a range of $[L_n, U_n]$, where L_n is the lower limit and U_n is the upper limit for depth n. The limits are decided by the number of modes that have been kept for the upper depths and the expected complexity of the whole CTU. They are updated instantly with the progress of mode filtering. If $L_n = U_n$, as shown in Fig.8, the number of modes need to be kept is fixed and the following evaluation is unnecessary. For example, there is no mode for depth 0 and 1 that is kept in the previous process, but the expected complexity is 4. In this case, for depth 2 and depth 3, both L_n and U_n are equal to 2. M_n is also equal to 2.

For the normal case that U_n is larger than L_n, M_n is derived by comparing the two cost ratios of C_{n0}/C_{nLower} and C_{n1}/C_{nLower} to the mode filtering parameter MFP_n.

Then, M_n is adjusted based on the limits of $L_n$and U_n. C_{n0} is smaller than C_{n1} and the comparison starts with C_{n0}/C_{nLower}. The progress mainly includes the following three cases.

(1) If C_{n0}/C_{nLower} is larger than MFP_n, depth *n* with the best mode has no priority compared to other lower depths. The best mode in depth *n* is removed in the mode filtering. In this case, the second-best mode should also be removed and M_n equals to 0. If $L_n > 0$, it means that the kept modes are not enough for keeping the whole complexity in a fixed level. Although both modes are not good enough, one or two modes should be remained. In this case, M_n is set to L_n, $(M_n = L_n)$.

(2) If the ratio of C_{n0}/C_{nLower} is equal or smaller than MFP_n, It implies that the best mode in depth *n* is better than modes in other lower depths. The best mode should be kept for depth *n*. Thus, M_n is updated to 1. Then, C_{n1}/C_{nLower} will be checked and the process goes to the case (3).

(3) If C_{n1}/C_{nLower} is larger than MFP_n, the second-best mode should be removed, M_n is still equal to 1 and finally determined. If C_{n1}/C_{nLower} is smaller or equal than $MFP_n$the second-best mode should be kept and M_n is updated to 2.In this case, the maximum number of allowed modes for this depth should be checked. If $M_n > U_n$, the final value of M_n should be adjusted to U_n $(M_n = U_n)$.

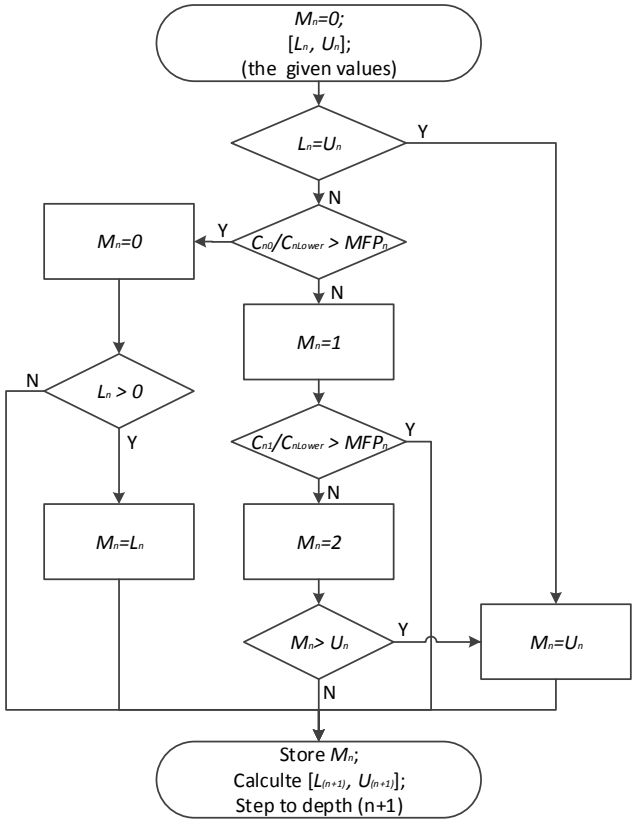

Fig. 8 CI-MF for one depth

By applying the same process for each depth, the kept modes across all the depths are decided. The FME will be performed to the kept modes.

3. 3 Proposed configurable CI- MF with *k* layers (CI-MF-*k*)

For a CTU, layers of FME equals to the sum of numbers of kept modes for all the depths. As described in previous section, CI-MF generates the number of kept modes M_n for each depth. It is related to the number of modes that have been decided as far and the expected complexity on FME.

Figure 9 describes the configurable scheme, wherein *k*

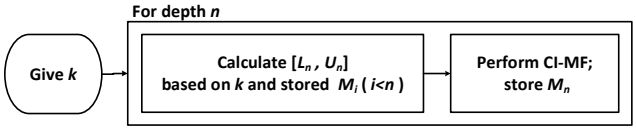

Fig.9 Configurable CI-MF-*k* scheme

Table 1 Experiment Condition

Sequences for simulation	21 Sequences from Class A～E; Class A (2560×1600): Traffic, PeopleOnStreet, Nebuta, SteamLocomotive; Class B (1920×1080): Kimono, ParkScene, Cactus, BasketballDrive, BQTerrace; Class C (832×480): BasketballDrill, BQMall, PartyScene, RaceHorsesC Class D (416×240): BasketballPass, BQSquare, BlowingBubbles, RaceHorses Class E (1280×720): Johnny, Vidyo1, Vidyo3, Vidyo4
Training sequences (Resolution)	15 sequences; 3 sequences from each class. Class A: Traffic, Nebuta, SteamLocomotive; Class B: Cactus, BasketballDrive, BQTerrace; Class C: BasketballDrill, BQMall, PartyScene; Class D: BasketballPass, BlowingBubbles, RaceHorses; Class E: Vidyo1, Vidyo3, Vidyo4.
Max CU/depth	64/4
GOP structure	LDP configuration (IPPP, reference frame number:1)
QP	22, 27, 32, 37
Comparison cases	Anchor: Original HM; Case1: HM with CI-MF-4; Case2: HM with CI-MF-5; Case3: HM with CI-MF-6.

represents layers of FME for each CTU that should be fixed by applying CI-MF. The range of M_n changes with different value of *k*. Accordingly, M_n may be different. By using this method, the complexity of the FME can be adjustable for different encoding requirement.

4. Simulation Results and Analysis

Simulation is implemented in HM 16.0 with the test configuration of Low-Delay-P (LDP) main [21]. Since one reference frame scheme is quite common in real-time application, only one reference frame is employed in this simulation. Other coding parameters are exactly accord with the default configuration recommended by JCT-VC. Simulation includes confidence intervals training and performance evaluation of CI-MF. The confidence intervals for different QPs and depths are obtained by training. As listed in **Table 1**, 21 Sequences from Class A to Class E that are recommended by JCT-VC are tested in the simulation. In the training, 3 sequences are randomly selected from each class, and 15 sequences are employed.

Table 2 Confidence intervals from training

$a_n/b_n/QP$	22	27	32	37
a_0	1.7158	1.6987	1.6654	1.6092
b_0	1.7822	1.7592	1.7206	1.6611
a_1	1.7405	1.7227	1.6871	1.6272
b_1	1.8136	1.7896	1.7493	1.6880
a_2	1.7637	1.7432	1.7052	1.6437
b_2	1.8374	1.8112	1.7701	1.7090
a_3	1.7565	1.7402	1.7062	1.6524
b_3	1.8331	1.8146	1.7809	1.7298

Firstly, the samples of cost ratio are taken from the training sequences. Based on the statistic computation with MATLAB, the mean value and standard deviations for different QPs and depths are derived. Then, for the training sequences, the confidence level is set from 50% to 95% with a step of 5%. The confidence intervals with the smallest average BD rate for the training sequences are selected and implemented in the CI-MF algorithm. Four training sessions with different training sequences are used to verify the reliability of the training method. In our experiments, it is found that the trained confidence intervals and the corresponding BD rate results of the four sessions are close with each other.

Therefore, it is possible to get reliable confidence intervals with the proposed training method. The confidence intervals derived from one of the training sessions are used for the final simulation. The sequences of this training session are listed in the second row of Table 1. **Table 2** shows confidence intervals from the training.

Cases 1, 2, 3 in Table 1 are executed with the proposed configurable CI-MF-*k* with *k* equals to 4, 5 and 6 respectively. They are all compared to the anchor of original HM to evaluate the efficiency of the proposed CI-MF algorithm. Moreover, the three cases are compared with each other to show how the RD performance and encoding time change with the different FME complexity setting.

Since this work is focused on reducing the complexity of FME part, the FME complexity is firstly measured by a parameter of layers for each CTU. This measurement is related to the complexity in terms of hardware cost since it is related to the number of pixels needs to be processed in the FME. By keeping the same number of modes for CUs with the same size and limiting the total number of modes across four depths, CI-MF-*k* fixes the complexity of FME in *k* layers for each CTU. The result is fixed regardless of video content and some encoding parameters like QP. HM has

incorporated many fast mode decision tools such as ESD (early skip detection), CFM (coding block flag based fast mode) and ECU (early CU termination) [22]. By enabling these tools, some CU or PU modes will be skipped, but the layers for each CTU will not be fixed. All the fast tools are disabled in default in HM. Our simulation employs the default setting that all the CU and PU modes should be traversed and the FME complexity is 24 layers for each CTU. FME complexity results in terms of layers for each CTU is shown in **Fig. 10**.

The performance of the proposed work is compared to the original HM and the result is listed in **Table 3**. ΔT_{FME} and ΔT_{Enc} are FME time reduction and encoding time reduction of the proposed work compared to Original HM, which are calculated as Eq. (14) and Eq. (15). $T_{FME}(original)$ and $T_{FME}(proposed)$ represent FME time for the original HM and the proposed work, respectively. $T_{Enc}(original)$ and $T_{Enc}(proposed)$ represent the encoding time for the original HM and the proposed work, respectively. RD performance of the proposed algorithm is measured by the Bjøntegaard-Delta rate (BD rate), which is calculated based on the results of PSNR and bitrate with four QPs. It corresponds to the average bitrate difference in percent for the same PSNR [23].

$$\Delta T_{FME} = \frac{T_{FME}(original) - T_{FME}(proposed)}{T_{FME}(original)} \quad (14)$$

$$\Delta T_{Enc} = \frac{T_{Enc}(original) - T_{Enc}(proposed)}{T_{Enc}(original)} \quad (15)$$

For the same sequence, ΔT_{FME} with different QP values is close since the reduced number of layers is the same. While the ΔT_{Enc} increases as QP value increases. In the following paper, we only discuss the average result

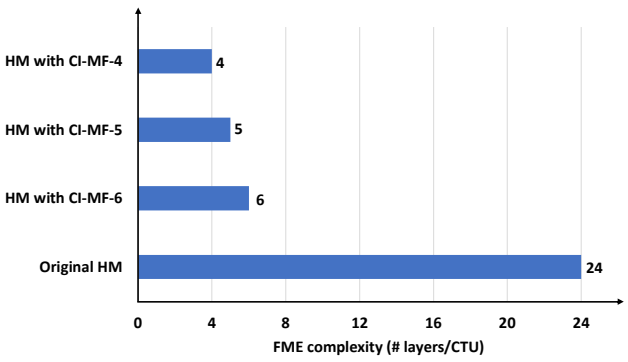

Fig.10 Complexity of FME

across different QP values. Taking the proposed HM with CI-MF-6 for an example, we discuss how the proposal effects the complexity and BD rate. By keeping only 6 modes across 4 depths, the FME complexity is reduced from 24 layers to 6 layers. FME is accelerated by 72.70% as expected. The whole encoding is accelerated by 44.22% as well. The proposed algorithm works better for the sequences with larger size. For example, the BD rate loss is even less than 0.1% for some sequences like SteamLocomotive from Class A.

However, for sequences from Class D with small size, the BD rate loss is significant. It is because that CTUs in the pictures with small size contains much more details compared to those in large size. Therefore, keeping the same number of modes for all the CUs in the same depth and reducing the number of modes to a low value bring much more loss for these videos. Comparing the results of the three cases, it is obvious that for each reduced one layer (*k* reduced by 1), ΔT_{FME} increases by 5% while the ΔT_{Enc} increases by 3%. When only 4 layers are kept, the FME time and encoding time reduction are up to 82.75% and 49.42% respectively. The BD rate loss is 1.63% on average. When the FME complexity is set from 4 to 6, the BD rate shows large improvement. We can set the complexity of the FME to different level for different encoding requirement.

The performance comparison between original HM and HM with CI-MF-4 for six sequences from different class is also shown in **Fig. 11** by RD curves. The RD curve in black represents the performance of original HM while the curve in red represents the performance of HM with CI-MF-4. The high conformity of two RD curves means that the performance of the two cases is quite close, such as the curves of the sequence of SteamLocomotive, as shown in Fig.11(b). For the sequence of *BQSquare*, the curve of CI-MF-4 is obviously below the curve of original HM, which means that the performance of CI-MF-4 is decreased compared the original HM, as shown in Fig.11(e). Our result shows that the BD rate of BQSquare is increased by 3.25% (PSNR loss 0.085dB and the bitrate increases 1.21% on average.)

The subjective visual quality comparison between original HM and HM with CI-MF-4 for the sequence of Kimono that has obvious texture and high motions are displayed. The reconstructed pictures with two QP values (22, 32) for the sixth frame are shown in **Fig. 12**. A 960×540 window is zoomed out from the frame of 1920×1080 size to show the details. Fig. 12(a) and Fig. 12(b) are the pictures encoded with QP of 22; Fig. 12(c) and Fig. 12(d) are the

Table3 Performance comparison of HM with CI-MF-4, CI-MF-5, CI-MF-6, with original HM

Class	Sequence	HM with CI-MF-4			HM with CI-MF-5			HM with CI-MF-6		
		BD rate [%]	ΔT_{FME}	ΔT_{Enc}	BD rate [%]	ΔT_{FME}	ΔT_{Enc}	BD rate [%]	ΔT_{FME}	ΔT_{Enc}
A	Traffic	1.53%	83.46%	52.40%	0.91%	78.06%	49.44%	0.82%	72.65%	46.30%
	PeopleOnStreet	1.27%	77.70%	42.52%	1.00%	73.38%	40.84%	0.98%	68.92%	38.60%
	Nebuta	1.28%	79.10%	39.70%	0.88%	74.39%	37.82%	0.38%	69.69%	35.65%
	SteamLocomotive	0.06%	85.83%	51.19%	0.01%	80.16%	48.30%	0.00%	74.27%	45.09%
Average		**1.03%**	**81.52%**	**46.45%**	**0.70%**	**76.50%**	**44.10%**	**0.55%**	**71.38%**	**41.41%**
B	Kimono	3.12%	78.00%	44.66%	1.56%	73.46%	42.64%	1.24%	69.06%	39.82%
	ParkScene	1.40%	84.08%	52.33%	0.80%	78.39%	49.44%	0.74%	73.32%	46.61%
	Cactus	1.62%	83.62%	50.79%	1.08%	78.67%	48.21%	1.16%	73.35%	45.40%
	BasketballDrive	2.17%	82.85%	49.32%	1.36%	77.79%	46.97%	1.19%	72.74%	44.33%
	BQTerrace	1.34%	84.52%	51.30%	0.85%	79.07%	48.58%	0.73%	73.48%	45.57%
Average		**1.93%**	**82.62%**	**49.68%**	**1.13%**	**77.48%**	**47.17%**	**1.01%**	**72.39%**	**44.35%**
C	BasketballDrill	1.77%	82.38%	48.81%	1.21%	78.80%	46.59%	1.01%	73.11%	43.90%
	BQMall	1.39%	83.67%	50.95%	0.80%	78.77%	48.22%	0.82%	73.30%	45.64%
	PartyScene	1.09%	82.58%	45.10%	0.73%	78.03%	43.03%	0.66%	72.56%	40.42%
	RaceHorsesC	1.95%	78.48%	40.06%	1.37%	74.17%	38.70%	1.00%	68.85%	36.56%
Average		**1.55%**	**81.78%**	**46.23%**	**1.03%**	**77.45%**	**44.14%**	**0.87%**	**71.96%**	**41.63%**
D	BasketballPass	1.45%	82.88%	50.92%	1.30%	77.46%	48.83%	0.66%	74.14%	46.63%
	BQSquare	3.25%	85.85%	48.66%	1.95%	81.45%	46.47%	1.88%	75.07%	42.71%
	BlowingBubbles	2.41%	80.53%	46.04%	1.57%	76.77%	43.12%	1.40%	73.23%	42.26%
	RaceHorses	1.82%	77.91%	39.47%	1.68%	74.36%	37.55%	1.44%	71.57%	36.64%
Average		**2.23%**	**81.79%**	**46.27%**	**1.63%**	**77.51%**	**43.99%**	**1.35%**	**73.50%**	**42.06%**
E	Johnny	1.43%	86.14%	59.31%	1.59%	80.21%	55.99%	0.74%	74.72%	52.44%
	Vidyo1	0.93%	86.22%	58.91%	0.61%	80.35%	55.62%	0.53%	74.37%	52.16%
	Vidyo3	1.90%	85.62%	56.73%	1.29%	79.62%	53.72%	0.90%	73.74%	50.18%
	Vidyo4	1.09%	86.30%	58.73%	0.57%	80.28%	55.30%	0.44%	74.53%	51.73%
Average		**1.34%**	**86.07%**	**58.42%**	**1.02%**	**80.12%**	**55.16%**	**0.65%**	**74.34%**	**51.63%**
Average for all		**1.63%**	**82.75%**	**49.42%**	**1.10%**	**77.79%**	**46.92%**	**0.89%**	**72.70%**	**44.22%**

pictures encoded with QP of 32. With the proposed CI-MF-4, PSNR is decreased by 0.03dB and 0.14dB for the QP of 22 and 32 respectively compared to original HM. But the quality difference cannot be captured by human eyes. In other words, the proposal has almost the same subjective quality with the original HM.

Table 4 shows the comparison results between CI-MF-4 and the previous work[13]. The results of CI-MF-4 in this table are corresponding to the result that listed in Table 3. In the performance comparison, we firstly implemented the previous method with HM16.0 that we used for this work. Secondly, we performed the simulation with the same environment and conditions. Both previous work and our proposal reduce FME from 24 layers to 4 layers. They achieved 84.56% and 82.75% FME time reduction, respectively. But improving the cost function and applying the adaptive CI according to different QP and depth, the performance of this work is much better. The BD rate loss is reduced from 2.18% to 1.63% on average.

5. Conclusion

In this paper, we present a low-complexity FME mode filtering algorithm CI-MF. It utilizes the ratio of IME-FME and the related confidence intervals to select the modes for different depths and keep the complexity of FME to a fixed level. The proposed CI-MF can be configurable for different encoding time and RD performance requirements.

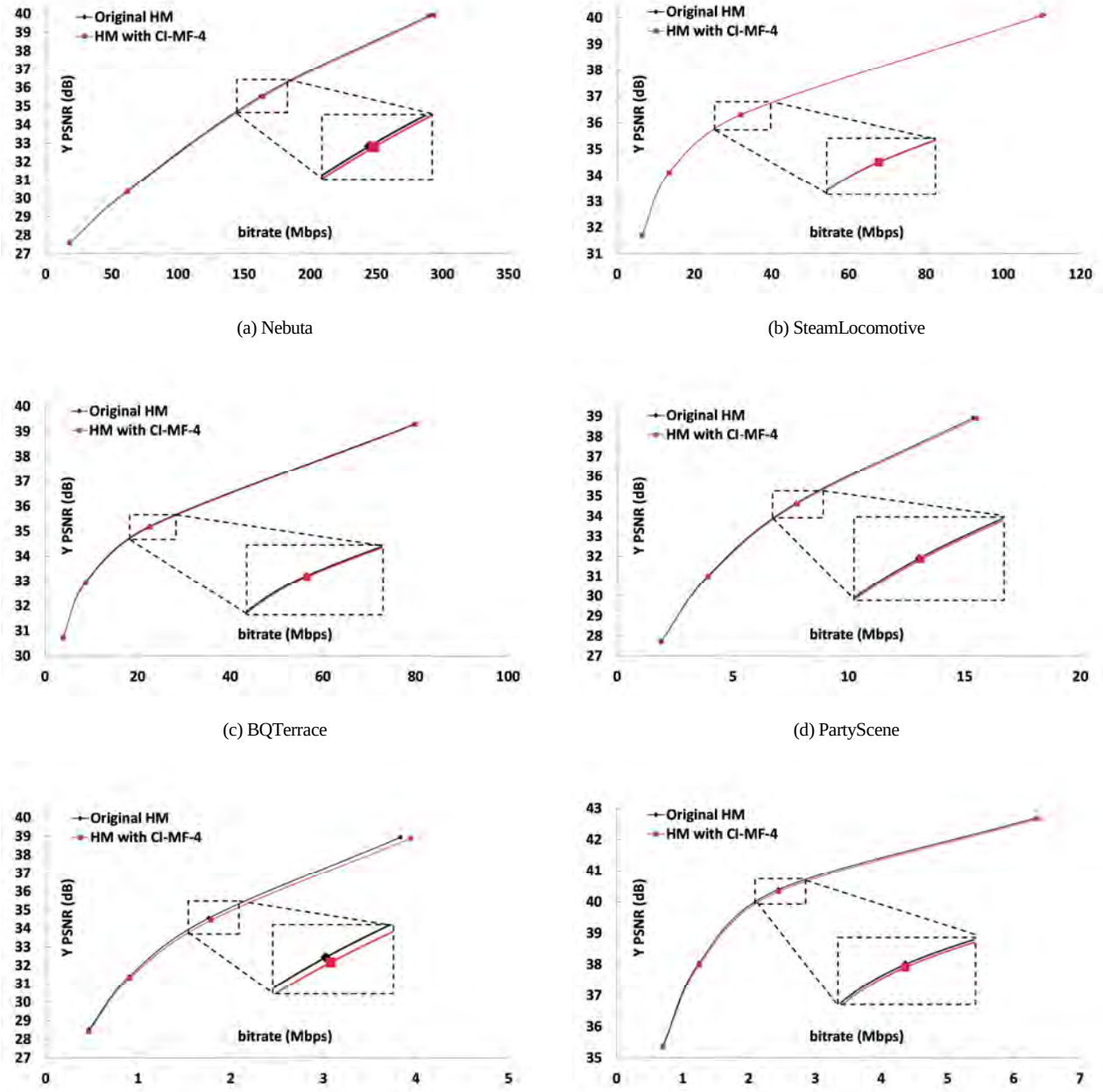

(a) Nebuta

(b) SteamLocomotive

(c) BQTerrace

(d) PartyScene

(e)BQSquare

(f) Vidyo3

Fig. 11 RD curves for different sequences

Simulation results demonstrate that the proposed CI-MF-4 scheme achieves 82.75% FME time reduction with 1.63% BD rate increasement compared to the original HM with full FME. The proposed algorithm is friendly to the hardware design. It will be applied to the ME part to solve the complexity problem in the real-time application in the future.

Acknowledgement

This work is supported by JST, PRESTO Grant Number JPMJPR1757 Japan.

(a) Kimono coded by original HM (QP: 22; PSNR: 41.6213dB)

(b) Kimono coded by HM with CI-MF-4 (QP: 22; PSNR: 41.5920dB)

(c) Kimono coded by original HM (QP: 32; PSNR: 36.7252dB)

(d) Kimono coded by HM with CI-MF-4 (QP: 32; PSNR: 36.5869dB)

Table 4 Performance comparison with previous work

Seq. Class	Previous work[13]			CI-MF-4		
	BD rate [%]	ΔT_{FME}	ΔT_{Enc}	BD rate [%]	ΔT_{FME}	ΔT_{Enc}
A	1.08%	83.95%	47.48%	1.03%	81.52%	46.45%
B	2.22%	84.87%	50.68%	1.93%	82.62%	49.68%
C	2.00%	83.25%	46.95%	1.55%	81.78%	46.23%
D	3.92%	83.42%	46.92%	2.23%	81.79%	46.27%
E	1.67%	87.24%	59.09%	1.34%	86.07%	58.42%
Ave.	2.18%	84.56%	50.25%	1.63%	82.75%	49.42%

References

1) Recommendation ITU-T H.264 | International Standard ISO/IEC 14496-10: “Advanced video coding for generic audiovisual services” (2019).
2) Recommendation ITU-T H.265 | International Standard ISO/IEC 23008-2: “High efficiency video coding” (2019).
3) M. Wien, High Efficiency Video Coding : Coding tools and Specification, Springer, pp.179-202 (2014).
4) K. McCann, C. Rosewarne, B. Bross, M. Naccari, K. Sharman, G. Sullivan: “High Efficiency Video Coding (HEVC) Test Model 16 (HM 16) Improved Encoder Description”, 19th meeting of Joint Collaborative Team on Video Coding (JCTVC), document JCTVC-W14970, Strasbourg (2014).
5) Joint Collaborative Team on Video Coding, HEVC Reference Software, HM16.0, https://hevc.hhi.fraunhofer.de/svn/svn_HEVCSoftware/tags/.
6) Y.-J. Wang, C.-C. Cheng, T.-S. Chang: “A Fast Algorithm and Its VLSI Architecture for Fractional Motion Estimation for H.264/MPEG-4 AVC Video Coding”, IEEE Trans. on Circuits and Systems for Video Technology Vol.17, No.5, pp.578-583 (2007).
7) T.-Y. Kuo, Y.-K. Lin, T.-S. Chang: “SIFME: A Single Iteration Fractional-Pel Motion Estimation Algorithm and Architecture for HDTV Sized H.264 Video Coding”, Proc. of International Conference on Acoustics, Speech and Signal (ICASSP), pp.1185 – 1188 (2007).
8) P.-K. Tsung, W.-Y. Chen, L.-F. Ding, C.-Y. Tsai, T.-D. Chuang, L.-G. Chen: “Single-Iteration Full-Search Fractional Motion Estimation for Quad Full HD H.264/AVC encoding”, Proc. of IEEE International Conference on Multimedia and Expo (ICME), pp. 9-12 (2009).
9) J. Kim, J. Yang, K. Won, B. Jeon: “Early Determination of Mode Decision for HEVC”, Proc. of Picture Coding Symposium (PCS), pp. 449-453 (2012).
10) Q. Yu, X. Zhang, S. Wang, S. Ma: “Early Termination of Coding Unit

Splitting for HEVC", Proc. of Asia Pacific Signal and Information Processing Association Annual Summit and Conference (APSIPA), pp. 1-4 (2012).

11) L. Shen, Z. Liu, X. Zhang, W. Zhao, Z. Zhang: "An Efficient CU Size Decision Method for HEVC Encoders", IEEE Trans. on Multimedia, Vol. 15, No. 2, pp. 465-470 (2013).
12) G.-Y. Zhong, X.-H. He, L.-B. Qing, Y. Li: "Fast Inter-Mode Decision Algorithm for High-Efficiency Video Coding Based on Similarity of Coding Unit Segmentation and Partition Mode between Two Temporally Adjacent Frames", Journal of Electronic Imaging, Vol. 22, No. 2, pp. 381-388 (2013).
13) J. Zhou, Y. Zhou, D. Zhou, S. Goto: "A fixed-complexity HEVC Inter Mode Filtering Algorithm Based on Distribution of IME-FME Cost Ratio", IEEE International Symposium on Circuits and Systems (ISCAS), pp. 617-620 (2015).
14) M. E. Sinangil, V. Sze, M. Zhou, A. P. Chandrakasan: "Cost and Coding Efficient Motion Estimation Design Considerations for High Efficiency Video Coding (HEVC) Standard", IEEE Journal of Selected Topics in Signal Processing, Vol. 7, No. 6, pp. 1017-1028 (2013).
15) D. Zhou, J. Zhou, G. He, S. Goto: "A 1.59Gpixel/s Motion Estimation Processor with -211-to-211 Search Range for UHDTV Video Encoder", IEEE Journal of Solid-State Circuits (JSSC), Vol. 49, No. 4, pp. 827-837 (2014).
16) V. Sze, M. Budagavi, G. J. Sullivan: "High Efficiency Video Coding (HEVC): Algorithms and Architectures", Springer, pp.303-341 (2014).
17) Wikipedia, "Standard normal table", https://en.wikipedia.org/wiki/Standard_normal_table/.
18) X. Zhao, J. Sun, S. Ma, W. Gao, "Novel Statistical Modeling, Analysis and Implementation of Rate-Distortion Estimation for H.264/AVC Coders", IEEE Trans. on Circuits and Systems for Video Technology, Vol. 20, No. 5, pp. 647-660 (2010).
19) Y-K. Tu, J-F. Yang, M-T. S, "Efficient Rate-Distortion Estimation for H.264/AVC", IEEE Trans. on Circuits and Systems for Video Technology, Vol. 16, No. 5, pp. 600-611 (2006).
20) Q. Wang, D. Zhao, W. Gao, S. Ma, "Low Complexity RDO Mode Decision Based on a Fast Coding-Bits Estimation Model for H.264/AVC", Proc. of IEEE International Symposium on Circuits and Systems (ISCAS), pp. 3467-3470 (2005).
21) F. Bossen: "Common Test Conditions and Software Reference Configurations", 11th meeting of Joint Collaborative Team on Video Coding (JCTVC), document JCTVC-K1100, Shanghai, China (2012).
22) K.-M. Lin, J.-R. Lin, M.-J. Chen, C.-H. Yeh, C.-A. Lee: "Fast Inter-prediction Algorithm Based on Motion Vector Information for High Efficiency Video Coding", Journal on Image and Video Processing, Vol. 99, pp. 1-17 (2018).
23) G. Bjøntegaard: "Calculation of Average PSNR Differences between RD-Curves", 13th meeting of Video Coding Experts Group, document VCEG-M33, Austin, Texas, USA (2001).

（Received March 20, 2019）
（Revised January. 27, 2020）

Muchen LI

She received the B.S degrees from the Physics Department of the East China Normal University, Shanghai, China in 2006, and the M. E degree from Waseda University, Kitakyushu, Japan, in 2011. She completes the doctor courses in Waseda University in 2017. She is currently a researcher in Hosei University, Tokyo, Japan. Her research interests include algorithms and VLSI architectures for multimedia processing and compressive sensing.

Jinjia ZHOU (*Member*)

She received the B.E. degree from Shanghai Jiao Tong University, Shanghai, China, in 2007, and the M.E. and Ph.D. degrees from Waseda University, Kitakyushu, Japan, in 2010 and 2013, respectively. She was a Researcher with Waseda University from 2013 to 2016. She is currently an Associate Professor with Hosei University, Tokyo, Japan. She is also a JST researcher, Tokyo, Japan, and She is also a senior visiting scholar in State Key Laboratory of ASIC & System, Fudan University, China. Her current research interests include algorithms and VLSI architectures for multimedia processing and artificial intelligence.. Dr. Zhou is a recipient of the Chinese Government Award for Outstanding Student dents Abroad of 2012. She received the Hibikino Best Thesis Award in 2011. She was a co-recipient of ISSCC 2016 Takuo Sugano Award for Outstanding Far-East Paper, the best student paper award of VLSI Circuits Symposium 2010 and the design contest award of ACM ISLPED 2010. She participated in the design of the world first 8K UHDTV video decoder chip, which was granted the 2012 Semiconductor of the Year Award of Japan. She works as a reviewer for journals including IEEE Trans. Circuits Syst. Video Tech., IEEE Trans. Circuits Syst. I, IEEE Trans. VLSI Syst., and IEEE Trans. Multimedia and so on.

Sotoshi GOTO

He received the B.E. and the M.E. Degrees in Electronics and Communication Engineering from Waseda University in 1968 and 1970 respectively. He also received the Dr. of Engineering from the same University in 1978. He joined NEC Laboratories in 1970 where he worked for LSI design, Multimedia system and Software as GM and Vice President. Since 2002, he has been Professor, at Graduate school of Information, Production and Systems of Waseda University at Kitakyushu. He served as GC of ICCAD, ASPDAC, VLSI-SOC, ASICON and ISOCC and was a board member of IEEE CAS society. He is IEEE Life Fellow and IEICE Fellow. He is Visiting Professor at Shanghai Jiao Tang University and Tsinghua University of China and Member of Science Council of Japan.

Call for Papers

Special Issue on
Image-Related Technologies for the Realization of Future Society

IIEEJ Editorial Committee

There is a great expectation for an advanced and comfortable society brought about by economic development and the solution of social issues through the introduction and spread of ICT technology. For this expectation, the government advocates and promotes Society 5.0 as a new future society, following hunting society (Society 1.0), agricultural society (Society 2.0), industrial society (Society 3.0), and information society (Society 4.0). It is clearly stated that this purpose is to build a system that coalesces cyber space (virtual space) and physical space (real space) at a high level, and integrates drones, AI devices, medical / nursing care, smart work, smart management and autonomous driving etc.

Not only image recognition and visualization, but also XR that integrates virtual reality (VR), augmented reality (AR), mixed reality (MR) is also necessary to make cyber space more familiar. In addition to visual effects, cross-modal sensory presentation that appeals to the human senses is emphasized. Therefore, technological innovation in computer graphics, computer vision, user interface, user experience, etc., which form these technological foundations, is important, and practical application of technology that appeals not only to vision but also to other senses through images and video.

In this special issue, we look forward to receiving your papers, system development papers, and data papers that will realize a future society through images and video.

1. Topics covered include but not limited to

   VR, AR, MR, Computer graphics, Image processing, Interaction, Realtime processing, Cross-modal sensory, Computer vision, Machine learning Image analysis, Object detection, Image recognition, User interface, User experience

2. Treatment of papers

   Submission paper style format and double-blind peer review process are the same as an ordinary contributed paper. If the number of accepted papers is less than the minimum number for the special issue, the acceptance paper will be published as an ordinary contributed paper. We ask for your understanding and cooperation.

3. Publication of Special Issue:

   IEEJ Transactions on Image Electronics and Visual Computing Vo.9, No.1 (June 2021)

4. Submission Deadline

   Friday, October 30, 2020

5. Contact details for Inquires:

   IIEEJ Office E-mail: hensyu@iieej.org

6. Online Submission URL: http://www.editorialmanager.com/iieej/

12TH ITU ACADEMIC CONFERENCE

ITU KALEIDOSCOPE 2020

Industry-driven digital transformation

7-11 December
ONLINE

CALL FOR PAPERS

Technically co-sponsored by

IEEE

IEEE ComSoc
IEEE Communications Society

Supported by

IEEE TEMS
Technology & Engineering Management Society

Organized by

ITU

ITU KALEIDOSCOPE 2020

Industry-driven digital transformation

CALL FOR PAPERS

Kaleidoscope 2020 – Industry-driven digital transformation *is the twelfth in a series of peer-reviewed academic conferences organized by ITU to bring together a wide range of views from universities, industry, and research institutions. The aim of the Kaleidoscope conferences is to identify emerging advancements in information and communication technologies (ICTs) and, in particular, areas in need of international standards to aid the healthy development of the Information Society.*

Theme

The Fourth Industrial Revolution has data analytics at its core, and relies on innovations in fields such as robotics, cyber-physical systems, digital twins, virtual simulation, augmented reality, edge computing, artificial intelligence and blockchain – innovations all contributing to digital transformation of industrial processes.

In particular, the manufacturing sector has been an early adopter of new technologies capitalizing on connectivity and intelligence, but these technologies introduce endless possibilities – the automotive, energy, retail and healthcare industries are all moving in this direction.

Objective

Kaleidoscope 2020 calls for original academic papers sharing insight into ongoing projects and research relevant to digital transformation. It targets specialists in the fields of ICT and socio-economic development, including researchers, academics, students, engineers, policymakers, regulators, innovators, and futurists.

Date and venue

Due to COVID-19, Kaleidoscope 2020 will be held exceptionally online from 7-11 December 2020.

Submission of papers

Prospective authors are invited to submit full, original papers. The submission should be within eight pages, including a summary and references, using the template available on the conference's website. All papers will go through a double-blind peer-review process. Submission must be made electronically; see *http://itu.int/go/K-2020* for more details on online submission (EDAS). Paper proposals will be evaluated based on content, originality, clarity, relevance to the conference's theme and, in particular, **significance to future standards**.

Deadlines extended

Submission of full paper proposals: **29 June 2020**

Notification of paper acceptance: **25 September 2020**

Submission of camera-ready accepted papers: **16 October 2020**

Publication and presentation

Accepted and presented papers will be published in the Conference Proceedings and will be submitted for inclusion in the IEEE *Xplore* Digital Library. The best papers will also be evaluated for potential publication in the IEEE Communications Standards Magazine. In addition, extended versions of selected papers will be considered for publication in the International Journal of Technology Marketing, the International Journal of Standardization Research, or the Journal of ICT Standardization.

Awards

A prize fund totalling CHF 6 000.- will be shared among the authors of the three best papers, as judged by the Steering and Technical Programme Committees. In addition, young authors of up to 30 years of age presenting accepted papers will receive Young Author Recognition certificates.

Keywords

Information and communication technologies (ICTs), standards, digital transformation, manufacturing and energy management, smart manufacturing, software defined networking, cyber-physical systems (CPS), cloud computing, fog computing, edge computing, mobile technologies, wireless networking (5G and beyond), machine-to-machine, 3D printing, advanced robotics, big data analytics, artificial intelligence (AI), machine learning, internet of things (IoT), industrial internet of things (IIoT), RFID technology, cognitive computing, trustworthiness, security, privacy.

Suggested (non-exclusive) list of topics

Track 1: Network and computing infrastructure, architecture

- Design principles, architecture and protocols for IIoT and digital twins
- Protocols and mechanisms for seamless IoT communications in wireless sensor networks
- Mobile and wireless communications
- Architecture and protocols for decentralized networking and services
- Cloud, fog and edge architectures

Track 2: Applications and services

- Smart manufacturing
- Infrastructure systems
- Verification and testing
- Virtual and augmented reality

Track 3: Enabling technologies

- AI and machine learning
- Intelligent real time data analytics
- Data management (analysis, quality, exchange, interoperability and integration prediction)

Track 4: Security, privacy and trust

- Security architectures, trust, identity management, protection mechanisms
- Threat models and attack strategies
- Security applications and management
- Lightweight cryptography

Track 5: Social, economic, standards, legal and policy aspects

- Regulation and standards for industrial Internet tools and services
- Multi-disciplinary standardisation
- New business models and multi-stakeholder aspects for digital transformation

Steering Committee

Andy Chen, Catronic Enterprise & REDDS Capital, Canada, and IEEE TEMS

Christoph Dosch, ITU-R Study Group 6 Vice-Chairman; IRT GmbH, Germany

Eva Ibarrola, University of the Basque Country, Spain

Kai Jakobs, RWTH Aachen University, Germany

Gyu Myoung Lee, Liverpool John Moores University, United Kingdom

Mitsuji Matsumoto, Waseda University Emeritus Professor, Japan

Roberto Minerva, Télécom SudParis, France

Mostafa Hashem Sherif, Consultant, United States

Technical Programme Committee

Chairman: Mostafa Hashem Sherif, Consultant, United States

The Technical Programme Committee is composed of over 60 subject-matter experts. Details are available at: *http://itu.int/en/ITU-T/academia/kaleidoscope/2020/Pages/progcom.aspx*

Additional information

For additional information, please visit the conference website: *http://itu.int/go/K-2020*. Inquiries should be addressed to Alessia Magliarditi at *kaleidoscope@itu.int*.

Partners

Organized by

Revised: January 6, 2017

Revised: July 6, 2018

Guidance for Paper Submission

1. Submission of Papers

(1) Preparation before submission

- The authors should download "Guidance for Paper Submission" and "Style Format" from the "Academic Journals", "English Journals" section of the Society website and prepare the paper for submission.
- Two versions of "Style Format" are available, TeX and MS Word. To reduce publishing costs and effort, use of TeX version is recommended.
- There are four categories of manuscripts as follows:
  - Ordinary paper: It should be a scholarly thesis on a unique study, development or investigation concerning image electronics engineering. This is an ordinary paper to propose new ideas and will be evaluated for novelty, utility, reliability and comprehensibility. As a general rule, the authors are requested to summarize a paper within eight pages.
  - Short paper: It is not yet a completed full paper, but instead a quick report of the partial result obtained at the preliminary stage as well as the knowledge obtained from the said result. As a general rule, the authors are requested to summarize a paper within four pages.
  - System development paper: It is a paper that is a combination of existing technology or it has its own novelty in addition to the novelty and utility of an ordinary paper, and the development results are superior to conventional methods or can be applied to other systems and demonstrates new knowledge. As a general rule, the authors are requested to summarize a paper within eight pages.
  - Data Paper: A summary of data obtained in the process of a survey, product development, test, application, and so on, which are the beneficial information for readers even though its novelty is not high. As a general rule, the authors are requested to summarize a paper within eight pages.
- To submit the manuscript for ordinsry paper, short paper, system development paper, or data paper, at least one of the authors must be a member or a student member of the society.
- We prohibit the duplicate submission of a paper. If a full paper, short paper, system development paper, or data paper with the same content has been published or submitted to other open publishing forums by the same author, or at least one of the co-authors, it shall not be accepted as a rule. Open publishing forum implies internal or external books, magazines, bulletins and newsletters from government offices, schools, company organizations, etc. This regulation does not apply to a preliminary draft to be used at an annual meeting, seminar, symposium, conference, and lecture meeting of our society or other societies (including overseas societies). A paper that was once approved as a short paper and being submitted again as the full paper after completion is not regarded as a duplicate submission.

(2) Submission stage of a paper

- Delete all author information at the time of submission. However, deletion of reference information is the author's discretion.
- At first, please register your name on the paper submission page of the following URL, and then log in again and fill in the necessary information. Use the "Style Format" to upload your manuscript. An applicant should use PDF format (converted from dvi of TeX or MS Word

format) for the manuscript. As a rule, charts (figures and tables) shall be inserted into the manuscript to use the "Style Format". (a different type of data file, such as audio and video, can be uploaded at the same time for reference.)

http://www.editorialmanager.com/iieej/

- If you have any questions regarding the submission, please consult the editor at our office.

Contact:
Person in charge of editing
The Institute of Image Electronics Engineers of Japan
3-35-4-101, Arakawa, Arakawa-Ku, Tokyo 116-0002, Japan
E-mail: hensyu@iieej.org
Tel: +81-3-5615-2893, Fax: +81-3-5615-2894

2. Review of Papers and Procedures

(1) Review of a paper

- A manuscript is reviewed by professional reviewers of the relevant field. The reviewer will deem the paper "acceptance", "conditionally acceptance" or "returned". The applicant is notified of the result of the review by E-mail.
- Evaluation method

  Ordinary papers are usually evaluated on the following criteria:
  - ✓ Novelty: The contents of the paper are novel.
  - ✓ Utility: The contents are useful for academic and industrial development.
  - ✓ Reliability: The contents are considered trustworthy by the reviewer.
  - ✓ Comprehensibility: The contents of the paper are clearly described and understood by the reviewer without misunderstanding.

  Apart from the novelty and utility of an ordinary paper, a short paper can be evaluated by having a quickness on the research content and evaluated to have new knowledge with results even if that is partial or for specific use.

  System development papers are evaluated based on the following criteria, apart from the novelty and utility of an ordinary paper.
  - ✓ Novelty of system development: Even when integrated with existing technologies, the novelty of the combination, novelty of the system, novelty of knowledge obtained from the developed system, etc. are recognized as the novelty of the system.
  - ✓ Utility of system development: It is comprehensively or partially superior compared to similar systems. Demonstrates a pioneering new application concept as a system. The combination has appropriate optimality for practical use. Demonstrates performance limitations and examples of performance of the system when put to practical use.

  Apart from the novelty and utility of an ordinary paper, a data paper is considered novel if new deliverables of test, application and manufacturing, the introduction of new technology and proposals in the worksite have any priority, even though they are not necessarily original. Also, if the new deliverables are superior compared to the existing technology and are useful for academic and industrial development, they should be evaluated.

(2) Procedure after a review

- In case of acceptance, the author prepares a final manuscript (as mentioned in 3.).
- In the case of acceptance with comments by the reviewer, the author may revise the paper in consideration of the reviewer's opinion and proceed to prepare the final manuscript (as

mentioned in 3.).

- In case of conditional acceptance, the author shall modify a paper based on the reviewer's requirements by a specified date (within 60 days), and submit the modified paper for approval. The corrected parts must be colored or underlined. A reply letter must be attached that carefully explains the corrections, assertions and future issues, etc., for all of the acceptance conditions.
- In case a paper is returned, the author cannot proceed to the next step. Please look at the reasons the reviewer lists for the return. We expect an applicant to try again after reviewing the content of the paper.

(3) Review request for a revised manuscript

- If you want to submit your paper after conditional acceptance, please submit the reply letter to the comments of the reviewers, and the revised manuscript with revision history to the submission site. Please note the designated date for submission. Revised manuscripts delayed more than the designated date be treated as new applications.
- In principle, a revised manuscript willl be reviewed by the same reviewer. It is judged either accceptance or returned.
- After the judgment, please follow the same procedure as (2).

3. Submission of final manuscript for publication

(1) Submission of a final manuscript

- An author, who has received the notice of "Acceptance", will receive an email regarding the creation of the final manuscript. The author shall prepare a complete set of the final manuscript (electronic data) following the instructions given and send it to the office by the designated date.
- The final manuscript shall contain a source file (TeX edition or MS Word version) and a PDF file, eps files for all drawings (including bmp, jpg, png), an eps file for author's photograph (eps or jpg file of more than 300 dpi with length and breadth ratio 3:2, upper part of the body) for authors' introduction. Please submit these in a compressed format, such as a zip file.
- In the final manuscript, write the name of the authors, name of an organizations, introduction of authors, and if necessary, an appreciation acknowledgment. (cancel macros in the Style file)
- An author whose paper is accepted shall pay a page charge before publishing. It is the author's decision to purchase offprints. (ref. page charge and offprint price information)

(2) Galley print proof

- The author is requested to check the galley (hard copy) a couple of weeks before the paper is published in the journal. Please check the galley by the designated date (within one week). After making any corrections, scan the data and prepare a PDF file, and send it to our office by email. At that time, fill in the Offprint Purchase Slip and Copyright Form and return the scanned data to our office in PDF file form.
- In principle, the copyrights of all articles published in our journal, including electronic form, belong to our society.
- You can download the Offprint Purchase Slip and the Copyright Form from the journal on our homepage. (ref. Attachment 2: Offprint Purchase Slip, Attachment 3: Copyright Form)

(3) Publication

- After final proofreading, a paper is published in the Academic journal or English transaction (both in electronic format) and will also be posted on our homepage.

IIEEJ Trans. on Image Electronics and Visual Computing

Vol. 8, No. 1 2020

Editor in Chief: Mei Kodama
The Institute of Image Electronics Engineers of Japan
3-35-4-101, Arakawa, Arakawa-ku, Tokyo 116-0002, Japan

Print: ISSN 2188-1898
Online: ISSN 2188-1901
CD-ROM: ISSN 2188-191x